UNIVERSITÉ D'ORLÉANS

ÉCOLE DOCTORALE SCIENCES ET TECHNOLOGIES

LABORATOIRES CEHMTI – CNRS / ITU – JRC

THÈSE présentée par : **Franck DE BRUYCKER**

soutenue le : **10 décembre 2010**

pour obtenir le grade de : **Docteur de l'université d'Orléans**

Discipline: **PHYSIQUE**

High Temperature Phase Transitions in Nuclear Fuels of the Fourth Generation

THÈSE dirigée par:

Mohammed MALKI	**Professeur, Université d'Orléans**

RAPPORTEURS:

Bo SUNDMAN	**Professeur, Royal Institute of Technology, Stockholm**
Gernot POTTLACHER	**Professeur, Institute of Experimental Physics, Graz**

JURY:

Y. GUERIN, Président	**[Directeur de recherche, CEA]**
G. POTTLACHER	**[Professeur, Technical University of Graz]**
B. SUNDMAN	**[Professeur, Royal Institute of Technology]**
R. KONINGS	**[Directeur de Recherche, European Commission]**
M. MALKI	**[Professeur, Université d'Orléans]**
D. MANARA	**[Chercheur, European Commission]**
F. MILLOT	**[Directeur de Recherche, C.N.R.S]**

Une étape se termine avec une pensée particulière pour Yves LAURENT, Titi,

pour avoir su partager son goût pour les sciences,

un GRAND Merci.

Remerciements

Les travaux présentés dans ce mémoire ont été effectués dans le cadre d'une thèse européenne afin d'obtenir le grade de Docteur de l'Université d'Orléans. Cette thèse a été menée sous la direction du laboratoire Conditions Extrêmes et Matériaux : Haute Température et Irradiation (CEHMTI-CNRS, Orléans) et ces trois années se sont déroulées entièrement à l'Institut Européen des Transuraniens de Karlsruhe (ITU). Je tiens, dans un premier temps, à remercier l'ensemble des personnes avec qui j'ai pu partager cette période, au travail comme en dehors, ce fut des années inoubliables.

Je remercie l'ensemble du personnel du CEHMTI pour son accueil et ses conseils. En particulier Mohammed Malki pour m'avoir suivi si « longtemps », tout d'abord comme professeur à Polytech'Orléans, puis comme maître de stage au CEMHTI et enfin comme directeur de thèse dans le même laboratoire. Merci d'avoir dirigé cette thèse malgré la distance. Je remercie également Francis Millot et Jean Claude Rifflet pour les mesures en pyrométrie UV et pour m'avoir fait visiter leur impressionnante salle des lasers.

La diversité culturelle du personnel de l'ITU et la qualité de ses laboratoires ont fait de ces trois années passées un réel plaisir. Merci au directeur de l'ITU, professeur Thomas Fanghaenel pour m'avoir permis de faire cette thèse dans son institut. Je remercie aussi Rudy Konings (en français !) pour m'avoir accueilli dans son unité Materials Research, son écoute et ses commentaires pertinents. Un grand merci à mon « chef » et aussi ami, Dario Manara, pour m'avoir donné cette opportunité de thèse et pour avoir tant apporté à cette aventure, elle n'aurait pas pu se passer si bien sans lui. Je tiens aussi à remercier Konstantinos Boboridis pour toute son aide et grâce à qui j'ai compris la définition du mot « exactitude », ευχαριστώ πολύ. Je remercie l'ensemble des personnes de Materials Reseach pour leurs aides et les bons moments passés à leur coté, pour ne citer qu'eux, notre secrétaire l'efficace Petra Strube, mon « officemate » Petronella Gotcu avec qui nous avons partagé les joies et les stress de la thèse. Des expériences n'auraient pas pu se réaliser sans leur aide, merci à Markus Ernstberger, Jean-yves Colle, Thierry Wiss, Philipe Raison, Bert Cremer et Artmut Thiele. Je ne peux pas, hélas, citer tout le monde ici. Il y a aussi les collègues des autres unités de l'ITU avec qui j'ai pu avoir des échanges enrichissants et grâce à qui j'ai pu obtenir et caractériser

de nombreux échantillons. Je pense en particulier à Joseph Somers, Rachel Eloirdi, Sylvain Morel (Grrr), Matteo Rini, Co Boshoven, Sarah Stohr et Daniel Bouexiere.

Certains travaux de cette thèse faisaient parti du programme F-Bridge ce qui m'a donné la chance de travailler avec les laboratoires du CEA de Saclay, Calculthermo et du CNRS de Rennes. Je remercie en particulier Christine Guéneau et Nathalie Dupin pour nos nombreux échanges (téléphonique bien souvent) et pour leurs multiples diagrammes de phases calculés, ainsi qu'Henri Noel et Olivier Tougait pour les projets que nous avons menés ensemble.

Si les collègues de travail ont été essentiels pour le bon déroulement de cette thèse, la famille a été tout aussi importante. Je remercie donc mes parents ainsi que mes sœurs et Christophe pour m'avoir suivi et encouragé durant toutes mes études, pour m'avoir transmis les valeurs qui m'ont guidé jusqu'ici. Un grand merci à Marion pour sa patience et son soutient, spécialement lors de la rédaction de ce rapport, fini les visiophones et les incessants voyages franco-allemands. Enfin, ce passage en Allemagne n'aurait pas pu se dérouler si bien sans les amis, l'équipe du Magic Building, El vecino Ernesto Gonzales (Punaise) et notre cuisinier privé Mattia Del Giacco. Je n'oublie pas Markus Beilmann pour TOUTE son aide, la bonne humeur de Mike Welland, la gentillesse de Julie Tondeur et de Cedric Cozzo, ni les séances d'espagnol passées avec Ana Isabel Martinez Abuela.

Merci à Tous.

Table des matières

Chapter 1: Introduction 1
1 Generation IV nuclear energy systems 1
2 The research and development project 4
3 Materials 5
3.1 Nuclear energy systems and nuclear fuels 5
3.2 Oxide and carbide fuels 5
4 Phase diagrams 10
4.1 The uranium plutonium dioxide phase diagram at high temperature 10
4.2 The Neptunium dioxide 12
4.3 The uranium - carbon phase diagram 13
4.4 The plutonium - carbon phase diagram 16
5 References – Chapter 1 19
Chapter 2: Experimental 21
1 Laser heating experiment 21
1.1 Sample holder 22
1.2 Heating agent 23
1.3 Pyrometry and temperature measurement 23
a) Theoretical Background 23
b) Fast two-channel pyrometer 26
c) Calibration 28
d) The size-of-source effect 32
2 Emissivity measurements 37
3 Ultra - Violet Pyrometry 43
4 Reflected Light Signal 48
5 Sample Characterization 49
5.1 X-Ray Diffraction 50
5.2 Scanning Electron Microscope and Electron Microprobe 50
5.3 Fusion extraction - infrared determination 51
6 References – Chapter 2 53
Chapter 3: Experimental Study of the Melting Behaviour of Oxide Nuclear Fuels 55
1 Introduction 55

2 Uranium Dioxide 56
3 Plutonium Dioxide 57
3.1 Sample preparation 59
3.2 Laser melting experiments on $PuO_{2.00}$ 61
3.3 PuO_{2-x} 68
3.4 Discussion 71
4 Uranium – plutonium mixed dioxides (MOX) 73
4.1 Sample preparation 73
4.2 Laser melting experiments on MOX samples 76
4.3 Post-melting sample characterization 79
a) X-Ray diffraction 79
b) SEM - EDS 81
4.4 Discussion 82
5 Neptunium Dioxide 84
5.1 Sample Preparation 84
5.2 Laser Heating 84
5.3 Discussion 86
6 References – Chapter 3 87
Chapter 4: Experimental Study of the Melting Behaviour of Carbide Nuclear Fuels 89
1 The uranium carbon phase diagram 89
1.1 Experimental methods 91
a) Sample preparation 91
b) Sample composition analysis 92
c) High temperature measurements via laser heating 97
1.2 High temperature behavior of uranium carbides 99
a) Multi-channel pyrometry measurements of uranium carbides 99
a.1) Uranium Monocarbide 99
a.2) Uranium Dicarbide 107
a.3) Experimental highlights 112
b) Investigation of the high temperature phase diagram U-C 113
c) Accuracy analysis 121
1.3 Summary of results on the uranium - carbon system 122
2 The plutonium carbon phase diagram 123
2.1 Experimental methods 124

a) Sample preparation 124
b) Sample analysis 125
2.2 High temperature measurements via laser heating 126
a) PuC 126
b) Pu_2C_3 132
2.3 Discussion 135
3 References – Chapter 4 137
Chapter 5: Conclusions 140
1 Progress in the experimental method 140
2 Material properties 142
3 Impact of the current result 144

Chapter 1: Introduction

The world's population expansion and its endeavor for a better life quality to everybody tend to a large increase of the energy needs. The worldwide demand is expected to increase of about 50% between 2000 and 2030, double in 2050. However, since the end of the 20th century, the humanity realized his environmental impacts and potential long-term consequences for global climate change. The fossil resources are broadly used because of their low cost and relatively easy accessibility. They are nevertheless not sustainable energies and high carbon dioxide issuers. The position of number national governments is to develop a wide range of energies clean and cost effective. The nuclear energy is one of the candidates to deal with this abrupt energy rise. Important research projects have nevertheless to be undertaken to improve the safety and nuclear waste recycling.

1 Generation IV nuclear energy systems

In 2000, ten countries (Argentina, Brazil, Canada, France, Japan, the Republic of Korea, the Republic of South Africa, Switzerland, the United Kingdom and the United State) agreed on a common nuclear energy development and formed the Generation IV International Forum[1] (GIF). The European Union joined the GIF in 2003. They all agreed on a common charter, a technological roadmap which must guide the research and development for innovative nuclear energy systems. Figure 1 shows an overview of the five generations of nuclear energy systems. It started in the 1950s with early prototype reactors, the generation II corresponds to commercial power plants constructed in the 1970s and the third one are improved models that are currently constructed. They offer principally advances in safety and economics. The generation IV energy systems involve new reactor types, more efficient, safe that may be used to produce secondary goods. In 2012, the first concrete results of the undertaken research projects are expected to allow the different GIF members to decide about building or not these new reactors.

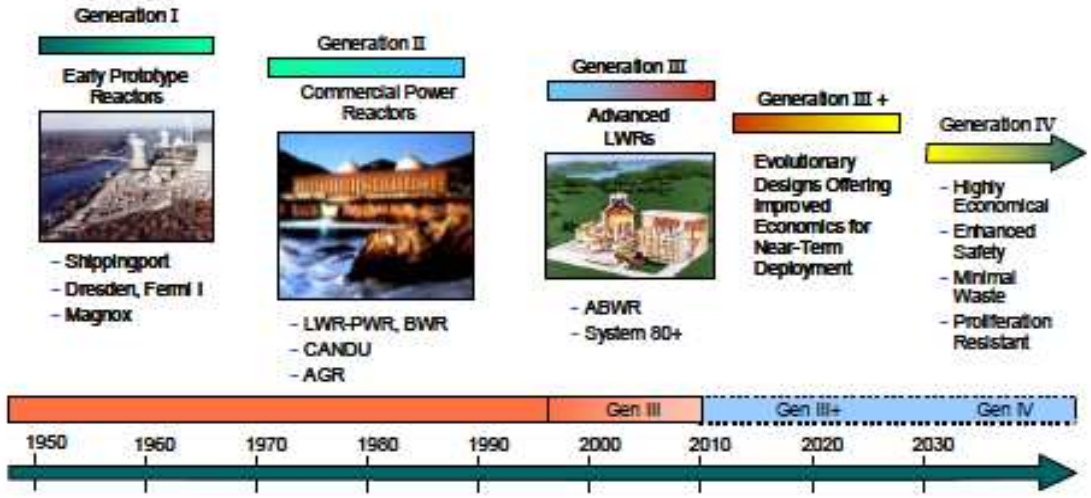


Figure 1: Overview of the five generations of nuclear energy systems

The GIF challenges will involve not only a demonstration of technical feasibility but also the development of robust industrial scale solutions. Four main criteria are taken into account for Generation IV [1].

- Sustainability: Generation IV nuclear energy systems must control the resources to assure energy for the present and future society needs. They will have to meet the objectives of minimizing environmental pollution and allowing an efficient fuel cycle. To decrease the volume of nuclear waste destined to long term storage, processes are being developed for burning the minor actinides in order to decrease their radioactivity and decay time. Important research is also carried out for waste confinement and storage[2].
- Economics: Generation IV nuclear energy systems must be economically competitive over other energy systems. The building cost has to be efficiently lower and the entirely fuel cycle, including recycling costs, should be quantitatively taken into account. For example, the fuel elements temperature will be increased for a better efficiency of converting heat to electricity and it will permit to produce secondary goods as hydrogen.
- Safety and reliability: Generation IV nuclear energy systems have to meet and excel in all safety recommendations more than the current nuclear plants do. This notion has high priority particularly in view of a broader public acceptance of nuclear energy. The incidence of human errors on malfunctioning of a reactor should be minimized as much as possible, and the consequences of any eventual accident should be confined to the inner part of a plant by as many passive safety systems as possible.

- Proliferation Resistance and Physical Protection: Generation IV nuclear energy systems must secure nuclear materials and facilities against terrorism and citizens' health. The fuel forms should be unattractive for the development of nuclear weapons, containing for example the fissile isotopes in chemical forms inadequate for bombs manufacturing.

Six different systems have been selected as those which best match the criteria presented above; they are listed in table 1. Each GIF member will choose one or more systems according to their own needs.

Generation IV		Very High Temperature Reactor	Gas-cooled Fast Reactor	Sodium-cooled Fast Reactor	Lead-cooled Fast Reactor	Super Critical Water-cooled Reactor	Molten Salt Reactor
FUEL	Oxide	P		P		P	
	Metal			P	S		
	Nitride		S		P		
	Carbide		P				
Recycle	Advanced aqueous	S	P	P	P	P	
	Pyroprocess	S	P	P	P		P
Generation-IV goals							
Efficient electricity generation		Very High	High	High	High	High	High
Possibility of high temperature process		Very High	High	Low	Low	Low	Medium
Sustainability : creation of fissile material		Medium/low	High	High	High	Low	Medium/ High
Sustainability : transmutation of waste		Medium	Very High	Very High	Very High	Low	High
Potential for passive "safety"		High	Very Low	Medium/low	Medium	Very Low	Medium
Current technical feasibility		High	Medium/low	High	Medium	Medium/low	Low

Table 1: The six fourth generation nuclear energy systems selected (P: Primary option; S: secondary option)

2 The research and development project

The main framework of this PhD project is the investigation of very high temperature (T > 1800 K) behaviour of materials employed in nuclear reactors of the Fourth Generation, and in particular the nuclear fuel. Among the fuels reported in Table 1, the main focus of the current work is on actinide carbides and oxides. These are refractory materials, i.e. they can be used at very high temperatures, melt above 2000 K (in most cases, above 2500 K) and maintain good mechanical and thermal properties up to melting. Although such high temperatures are normally not reached during operation of most nuclear plants (the centreline temperature of fuel elements in some fast reactors constitute exceptions), it is nonetheless important to investigate the behaviour of those materials in case of a thermal excursion of the reactor core up to temperatures close to or beyond melting. Moreover, the melting point and behaviour of those materials constitutes an important reference point for high temperature theoretical studies (e.g.: the fuel Equation of State) as well as for pure basic research.

The high temperature research field was initiated at the Institute for Transuranium Elements (ITU) of the European Commission's Joint Research Centre (EC – JRC) in the late 1980's and during the 1990's when the first high power lasers were purchased and employed as heating systems[3]. In parallel, fast multi-wavelength pyrometry techniques were developed for temperature measurements. In the last decade, these techniques gave the necessary experimental background for advanced studies of high temperature thermophysical and thermodynamic properties of conventional nuclear fuel, essentially stoichiometric and non-stoichiometric uranium dioxide, and (U, Pu) mixed dioxides (MOX) with low-Pu content (up to 15 at.% Pu)[4,5]. Within the current PhD thesis, this field of investigation is extended to other fuel forms, mostly envisaged for the nuclear plants of the Fourth Generation.

Among the oxide systems investigated here, particular focus is given to high-Pu MOX (up to 100 at.% Pu), and to minor actinide oxides (namely, NpO_2).In addition, very high temperature phase transitions of uranium and plutonium carbides are extensively studied with the current experimental approach.

The many original results obtained in the current research only in some cases agree well with existing literature data. This shows how the experimental approach employed in this

work (fast laser heating under quasi-containerless conditions and controlled atmosphere, coupled with fast multi-wavelength pyrometry) permits to overcome difficulties inherent to the experimental investigation of materials at very high temperatures, at which the sample reactivity is greatly enhanced and its chemical and mechanical stability becomes very limited. All these aspects will be extensively discussed in the following chapters for the different types of materials studied. Thus, the results and conclusions of this PhD project have the double objective of enriching the databases of physico-chemical properties of actinide compounds, and becoming a starting point for further research in this same field, where experimental data are still rare and often controversial.

3 Materials

3.1 Nuclear energy systems and nuclear fuels

A huge amount of energy is produced from the splitting of heavy nuclei, which is technically called nuclear fission[5]. Nuclear fission can occur spontaneously or be induced by neutron bombardment in a number of nuclides of actinide elements, which are then called *fissionable* nuclides[6]. Only very few of those nuclides can however produce, upon fission, neutrons in the right number and energy to induce a *chain reaction*, which can effectively be exploited for energy production. Those nuclides are called *fissile*. Technically, only three such nuclides can nowadays be exploited for the production of nuclear energy: ^{233}U, ^{235}U and ^{239}Pu. Among those, only ^{235}U is abundant enough in nature to be used as a nuclear fuel without further artificial isotope enrichment or production. ^{239}Pu is produced from neutron bombardment of ^{238}U (the most abundant uranium isotope in nature), whereas ^{233}U is obtained by neutron bombardment of ^{232}Th, through a complex and expensive process. In the end, the most used and common fission nuclear fuels are ^{235}U and ^{239}Pu. These isotopes are exploited as nuclear fuels in uranium – plutonium metal or compound.

3.2 Oxide and carbide fuels

Traditionally, and historically, the most common chemical form for the nuclear fuel elements is the dioxide, mostly UO_2 containing a certain amount of PuO_2. Compared to other fuel forms (pure metals, carbides, nitrides, fluorides, other oxides etc.) the dioxide has the

advantage of a good chemical stability at the reactor operational temperatures, and a fairly easy preparation process due to its stability at ambient conditions. The majority of existing light water reactor (LWR) plants utilizes uranium dioxide as fuel. However, plutonium (^{239}Pu) is created during irradiation through neutron capture by ^{238}U and chemically stabilized in the UO_2 crystal lattice. Although part of this plutonium is subsequently fissioned in the reactor, it is still present in significant amounts in the fuel at the end-of-life. In order to utilize this resource, a number of countries have chosen to adopt a plutonium recycling policy. The reprocessed plutonium is mixed with uranium dioxide to produce mixed oxide fuel (MOX). Originally intended for use in fast reactors, MOX is nowadays extensively used in light water reactors (LWRs). MOX is produced by a mechanical process to mix powders, but new techniques of manufacturing are developed for the preparation of these fuels. Based on co-precipitation or sol-gel methods, they focus on the production of a single powder with the required uranium plutonium ratio. In this way, the plutonium generated in nuclear power reactors can be re-used and the quantities of (enriched) uranium needed for fuel production as well as the volume of nuclear waste for final disposal are drastically reduced.

Generally, the plutonium content in LWR fuels remain relatively low and does not exceed the 15%, but liquid metal cooled fast reactor (LMFR), operate with MOX containing up to 30% plutonia. In future, the needs for faster disposition of plutonium, for the conception of compact reactor cores and of better efficiency will lead up to use MOX of high plutonia MOX (>30%). The use of this type of fuels requires accurate thermophysical data to ensure safe reactor operation. Available literature information for MOX containing more than 30% Pu is limited. Numerous questions remain, just to name few of them some doubts concern the chemical compatibility with the core materials of the reactor, with the coolant system, the fuel behavior under mechanical stress, irradiation or even under different oxygen partial pressures. It must be also mentioned that if the U-O system has been extensively investigated, the Pu-O, as all other actinide – oxygen systems, remains very uncertain. Consequently the U-Pu-O system is also not well known and the $(U,Pu)O_2$ experimental data and thermodynamic models still need to be assessed.

Carbide fuels constitute a valid alternative to oxides thanks to their higher density of fissile material. Moreover, the metallic thermal conductivity (Figure 2) and high melting temperature of actinides (An) carbides ensure a higher conductivity integral margin to melting (CIM) for these materials with respect to the traditional UO_2, UO_2-PuO_2 fuels. The CIM is an

important parameter of merit for the fuel performance, and is defined by the following integral:

$$CIM = \int_{T_{op}}^{T_{melt}} \lambda(T)dT \qquad (1)$$

Here, T_{op} is the reactor operational temperature at the fuel-cladding interface (around 800 K for LWR, up to 1500 K for the Generation IV very high temperature reactors) and T_{melt} is the fuel melting temperature. The higher is the CIM, the safer and more efficient is considered the reactor.

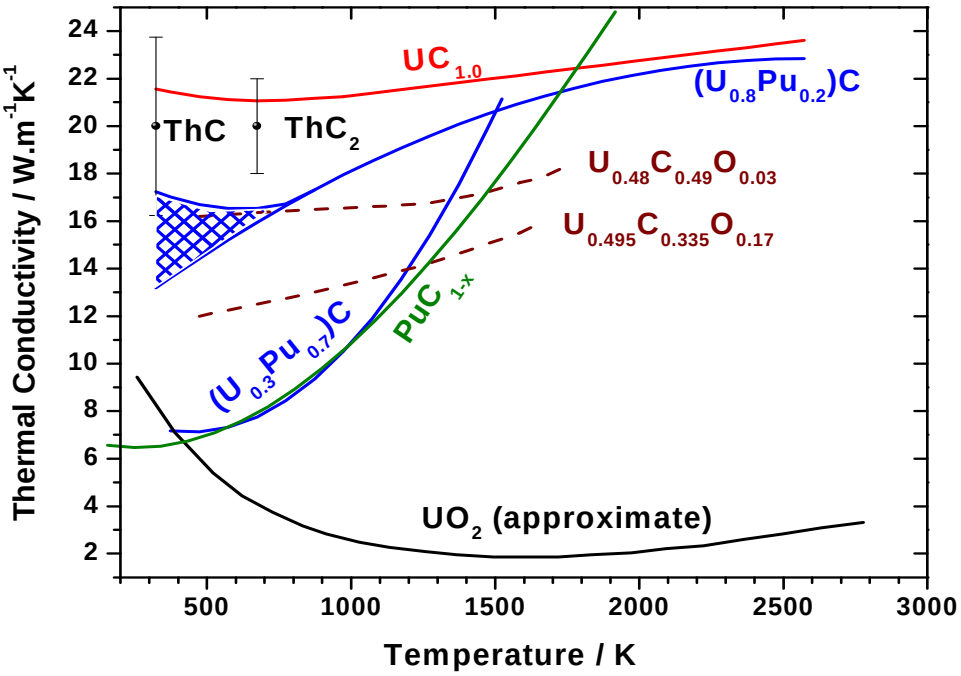


Figure 2: The thermal conductivity of some actinide carbides and carbide oxides compared to uranium dioxide. ±10% uncertainty bands should be assigned to each curve. The shaded area in the low-temperature part of the $U_{0.8}Pu0_{.2}C$ curve indicates larger uncertainty in the low temperature values for this compound. Heat conduction takes place in carbides via phonon and electron transport, the first prevailing at low temperature, and the second at high temperature[7].

This feature, together with the better compatibility with liquid metal coolants of carbides compared to oxides, are further reasons making of them good alternative candidates for high burnup and/or high temperature nuclear fuel. On the other hand, uncertainties on the An carbides behaviour mostly linked to metastability and uncontrollable oxygen and nitrogen

impurities still represent an obstacle to the fabrication and employment of these materials. A further drawback is represented by the difficulty in recycling unused fissile fuel from spent carbides through established chemical processes.

For all these reasons, carbide fuels are preferably foreseen in reactor types not conceived in view of fuel recycling, but rather for high burnup and operational temperature (GFR or VHTR). One interesting form for those sorts of reactors is represented by the coated particle fuel geometry. In this fuel conception (figure 3), the fissile material is included in the reactor core in coated micro-spheres (or "pebbles"). This way, the thermal exchange between the fuel elements (the microspheres) and the coolant is maximized, and the temperature drop between the fuel core and its periphery is minimized. These conditions are therefore optimal for a very high operational temperature of the plant. Moreover, the small volume of the fissile elements ensures effective passive safety against super-critical nuclear accidents.

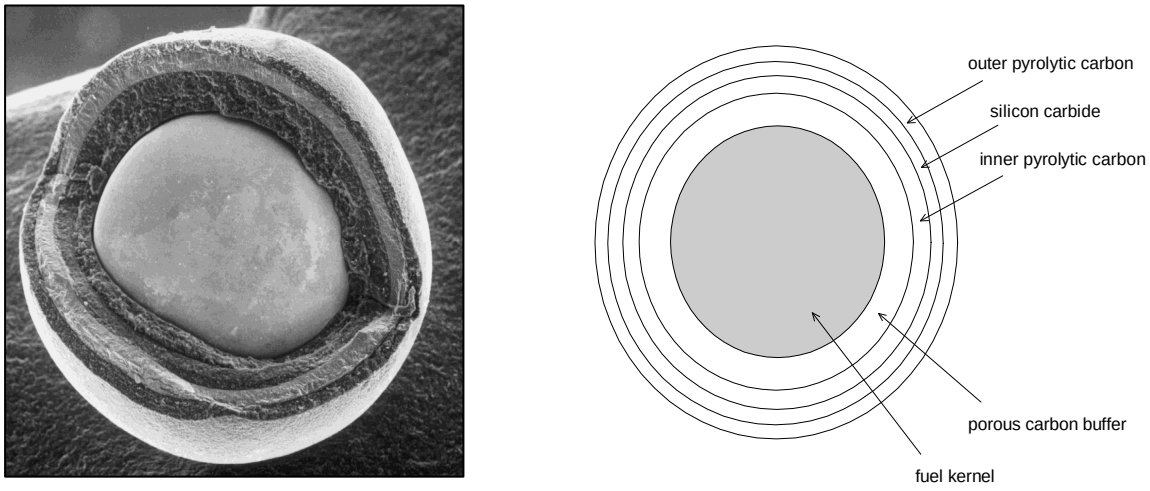


Figure 3: the coated particles fuel concept.

Uranium carbide pellets were traditionally used as fuel kernels for the US version of pebble bed reactors as opposed to the German version based on uranium dioxide[8]. As for the currently envisaged fuel for the Generation IV nuclear systems, mixed uranium-plutonium carbides (U, Pu)C constitute the primary option for the gas fast reactors (GFR), whereas monocarbide oxide UCO is the first candidate for the very high temperature reactor (VHTR). In the former case the fuel's high actinide density and thermal conductivity are exploited in view of high burnup performance. In the latter, UCO fuel is a good compromise between oxides and carbides both in terms of thermal conductivity and fissile density. However, in the

American VHTR design, the fuel is a 3:1 ratio of UO_2:UC_2 for one more essential reason, which was well explained by Olander[9]. During burnup, pure UO_2 fuel tends to oxidize to UO_{2+x}. UO_{2+x} reacts with the pyrocarbon coating layer according to the equilibrium:

$$UO_{2+x} + xC \rightarrow UO_2 + xCO \quad (2)$$

The production of CO constitutes an issue in the VHTR because the carbon monoxide accumulates in the porosity of the buffer layer. The CO pressure in this volume can attain large values and, along with the released fission gas pressure, it can compromise the integrity of the coating layers and contribute to the kernel migration in the fuel particle ("amoeba effect"). In the presence of UC_2, the following reaction occurs rather than reaction (2) in the hyperstoichiometric oxide fuel:

$$UO_{2+x} + xUC_2 \rightarrow (1+x)\, UO_2 + 2xC \quad (3)$$

Because reaction (3) does not release CO, it is more desirable than (2) in view of the fuel integrity.

The Pu-rich mixed carbide is used for the Indian Fast Breeder Test Reactor[22]. However, pure plutonium carbides present the drawback, with respect to pure U or mixed carbides, of some thermophysical properties (such as a low solidus temperature and low thermal conductivity) less suitable to a nuclear fuel.

Other chemical forms of the nuclear fuel have been used or envisaged, such as pure metals or nitrides. Although these are advantageous in terms of CIM and fissile density with respect to carbides and oxides, their reduced chemical stability and difficult preparation procedure have limited their application to a few particular cases. Like the actinide fluorides, essentially employed in the molten salt reactors (MSR), these fuel forms have not been investigated in the present study.

4 Phase diagrams

It is a primary goal of the present PhD project to investigate the high-temperature phase stability of chemical systems (namely actinide oxides and carbides) constituting specific nuclear fuels. Knowledge, as it can be found in the current scientific literature, of binary, pseudo-binary and, in some cases, ternary phase diagrams of such chemical systems is the starting point of the present research.

4.1 The uranium plutonium dioxide phase diagram at high temperature

The first experimental studies of the pseudo-binary UO_2 – PuO_2 phase diagram were performed in the 1960s. They were based on solidus – liquidus measurements obtained by thermal arrest technique on tungsten-encapsulated samples[10-12]. In the last decade, first Carbajo[13] and more recently Guéneau et al.[14] proposed a phase diagram based on these experimental data and thermodynamic modeling and optimization. According to these assessments, the uranium and plutonium dioxides form a continuous solid solution and the solidus and liquidus temperatures show a nearly ideal behavior as shown in Figure 6. Adamson et al[12] proposed the following equations to fit the solidus and liquidus curves (x is the PuO_2 mol%):

$$T_{solidus}(K) = 3120 - 655.3x + 336.4x^2 - 99.9x^3 \quad (4)$$

$$T_{Liquidus}(K) = 3120 - 388.1x - 30.4x^2 \quad (5)$$

However, recently Kato et al. published a new experimental study in which the commonly accepted phase transition temperatures were questioned and considerably higher values were proposed in the composition range from 20 to 100% PuO_2[15]. While they essentially used the same thermal arrest technique as in the 1960s, the authors of this latter study paid particular attention to the effect on the measured melting temperature of not only the exact oxygen-to-metal-ratio, as previous investigators had done, but also of sample-containment interactions. Thus, they obtained higher melting transition temperatures than earlier researcher did. They could also attribute the lower value of previous studies to

extensive interactions between MOX samples with a PuO_2-content higher than 20 mol% and tungsten, the typical crucible material in this temperature range. Their approach for avoiding this problem was to first encapsulate the high PuO_2-content samples in an inner rhenium container, which was in turn enclosed in the tungsten crucible. However, even so it was not possible to measure the melting temperature of pure PuO_2 directly, because in that case rhenium was not inert enough either, and the suggested value had to be estimated from an extrapolation of the measurements at lower PuO_2-concentrations based on an ideal solution model.

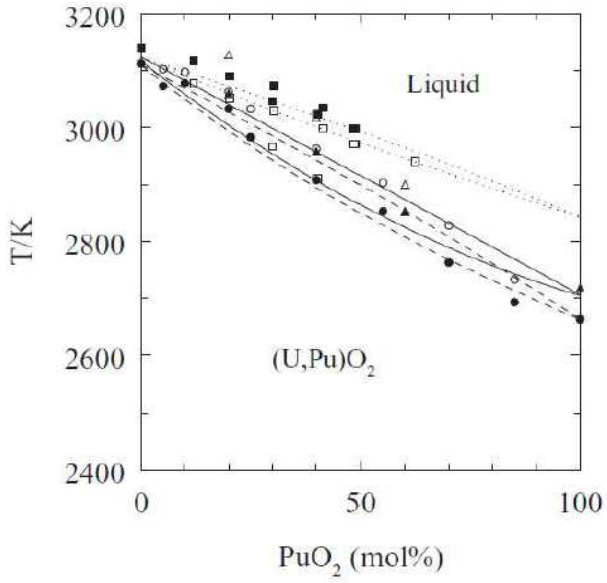


Figure 4: UO_2-PuO_2 region; The circles correspond to the experimental data by Lyon and Bailey[10], the triangles by Aitken and Evans[11], and the squares by Kato et al[15]; The solid lines represent the recommended liquidus and solidus by Adamson et al[12], the broken line the ideal liquidus and solidus based on Lyon and Bailey[10], and the dotted line the liquidus and solidus suggested by Kato et al.

UO_2 and PuO_2 have both the fluorite-type structure and both compounds have actinides with a +4 degree of oxidation. However, they can have number of different oxidation states and exist respectively as hypostoichiometric (MO_{2-x}) or hyperstoichiometric (MO_{2+x}) states. This particularity can be explained based on the degree of f-electron localization. Although this approach is beyond the scopes of the present research, it is important to recall its main conclusions in terms of electronic valence of these elements: uranium has delocalized f electrons and can display valence +3, +4, +5 and +6; on the other hand plutonium has more localized f electrons which are more bound to the actinide ion which normally has valence +3 or +4. Although recently Ashke et al.[16] demonstrated that, under particular conditions and in the presence of H_2O, the plutonium dioxide can also exist

with higher valence. However, these conditions are far from being reproduced in the current research. These phenomena can be resumed in thermodynamic terms by stating that stoichiometric PuO_2 has higher oxygen potential than stoichiometric UO_2 has. This results in an additional difficulty for the high temperature measurements. While the uranium dioxide is easily oxidized, the plutonium dioxide is easily reduced. Thus even with a general stoichiometry of the mixed oxide of uranium and plutonium, it is possible to create multiple oxide phases through oxygen exchanges and disproportioning of the actinides

Considering the assumptions of Kato et al.[15], it quickly appeared interesting to re-measure the melting temperatures of the (U, Pu) MOX with a new experimental approach. As explained above, the two main difficulties in this research are the sample reactivity with their holder/crucible, particularly for the high plutonium content, and the control of the oxygen/metal ratio during the thermal treatment. Two parallel series of experiments were performed: the first concerned the study of pure PuO_2 and the second the study of different MOX compositions with Pu content varying from 25 to 90 mol%.

4.2 The Neptunium dioxide

Neptunium is the first transuranic element. Its most stable isotope, ^{237}Np (half-life = $2.144 \cdot 10^6$ years), is a by-product of nuclear reactors and plutonium production. Neptunium is also found in trace amounts in uranium ores due to transmutation reactions.^{237}Np is formed either by α-decay of ^{241}Am or from ^{235}U by neutron capture:

$$^{235}U + n \xrightarrow{\gamma} {}^{236}U + n \rightarrow {}^{237}U \xrightarrow{\beta^-, 6.75d} {}^{237}Np \qquad (6),$$

^{237}Np is the most mobile actinide in the deep geological repository environment[17]. Moreover, due to its long half life, it becomes the major contributor to the radiotoxicity after 10000 years. This makes it and its predecessors such as ^{241}Am candidates of interest for destruction by nuclear transmutation. Knowledge of Np oxides properties[18] is therefore important for the management of fuel waste, as well as for transmutation concepts, like the Generation 4 idea of "minor actinide burning" and "deep burn"[19]. From a basic research viewpoint, a sound

determination of the NpO_2 melting point constitutes an important data in the actinide oxide series, which can help the understanding of the 5f electron behaviour in these compounds.

Melting point measurements of NpO_2 were published twice prior to the present research project, by Chikalla et al.[20] in 1971 and by Richter and Sari[21] in 1987. In both cases, NpO_2 specimens were heated to melting in a resistance furnace whereby the temperature was measured by filament pyrometry. The melting points reported in these two publications are in good agreement, (2830 ± 50) and (2820 ± 60) K respectively. Like in the case of PuO_2, however, these results may be affected by the high oxygen potential of quasi-stoichiometric NpO_2, resulting in important oxygen losses at high temperature. It has therefore been decided to undertake a new the measurement of the NpO_2 melting/freezing temperature with the innovative fast heating method used in this PhD study.

4.3 The uranium - carbon phase diagram

The uranium - carbon phase diagram (figure 5) presents three stable compounds, the uranium mono-carbide (UC), the dicarbide (UC_2) and the sesquicarbide (U_2C_3). The main characteristics of these compounds are summarized in Table 2.

Several experimental and theoretical studies exist on UC and the different authors generally agree on its physico-chemical characteristics. It is stable from room temperature to its melting point ((2780 ± 20) K). Its structure is rock-salt (B1, space group 225), however, at high temperature (>1400 K), UC can exist in both hypostoichiometric and hyperstoichiometric forms[23]. It can accommodate either carbon vacancies or an excess of carbon atoms substituting a single carbon with two carbons.

Some features of uranium sesqui- and di-carbide are still controversial. The uranium dicarbide phase exists in two different structures, a tetragonal form at lower temperatures (α-UC_2) and a cubic form at higher temperatures (β-UC_2). UC_2 exists in the hypostoichiometric form, its stability limits in equilibrium with C varying from $UC_{1.89}$ at the lowest temperatures to $UC_{1.92}$ at the highest[24]. α-UC_2 has a hypo-stoichiometry domain extending from the carbon-rich boundary to a phase limit in equilibrium with U_2C_3, which extends to $UC_{1.78}$ at its maximum temperature (2057 K – Figure 5). At higher temperature, U_2C_3 is in equilibrium with β-UC_{2-x}. The martensitic transformation from α- to β-UC_2 occurs at around 2050 K. The

latest studies on the β-UC_2 structure were performed by Allen et al.[25]. They used a high temperature neutron diffraction method to demonstrate that β-UC_2 is of the type B1 KCN. These conclusions rule out the CaF_2 structure previously proposed by Mallet and agree with the complete miscibility of UC and UC_2 at high temperature[26]. The sesquicarbide has a body-centered (bcc) cubic structure (space group I $\bar{4}$3d, No. 220). It is stable from 1200 K to (2100 ± 25) K[27]. Below these temperatures it exists as a metastable phase since UC+C are the stable phases. U_2C_3 decomposes with a peritectoidal reaction into UC_{1+x} and β-UC_{2-y}.

Sear[28] determined the borders of the miscibility gap between these two phases by microstructure analysis on quenched samples. The lower limit of this miscibility gap corresponds to a peritectoid (2106 K) delimited between C/U = 1.1 and C/U = 1.7 and its maximum temperature is 2323 K at a composition close to C/U = 1.3. The domain situated between the miscibility gap and UC_2 is still under discussion but some new studies on this point may help to understand the transition from UC_2 to U_2C_3. At higher temperature, UC_{1+x} and β-UC_{2-y} are fully miscible, so that some authors[29] identify them rather as $UC_{1+x'}$ and UC_{1+x}'. The liquidus line presents two maxima between UC and UC_2 at (2780 ± 20) K and (2730 ± 20) K corresponding to the melting point of UC and $UC_{1.9}$ respectively. A minimum temperature around 2675 K is observed between C/U = 1.5 and C/U = 1.6. Although melting temperatures in the literature show large dispersion, probably due to the sample impurities and alteration during the heat treatment, the points assessed by Fischer[30] can be considered as reliable within the reported uncertainties. The liquidus and solidus lines are very close together at all compositions, and can hardly be distinguished experimentally.

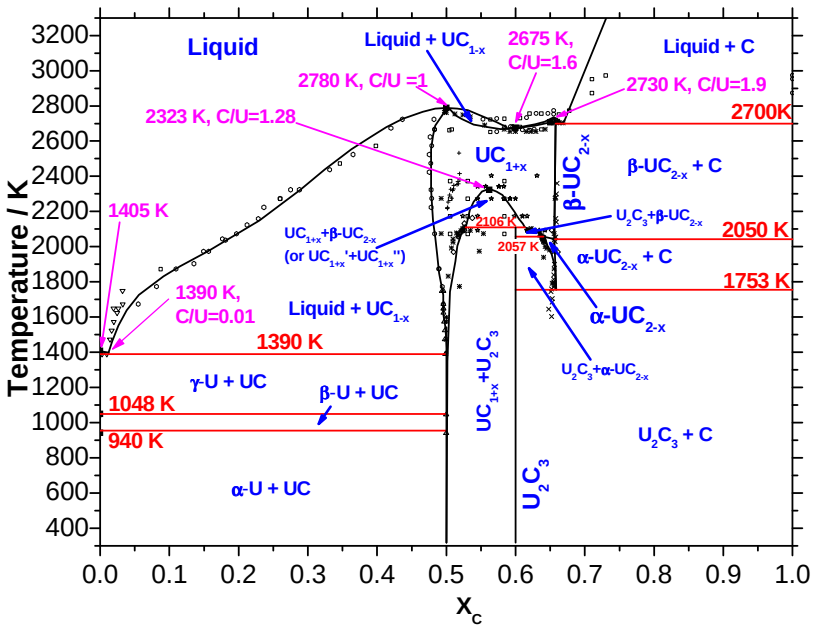


Figure 5: The uranium carbon phase diagram

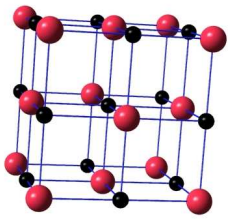
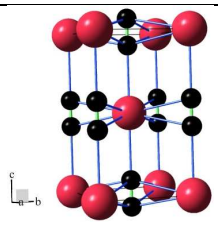
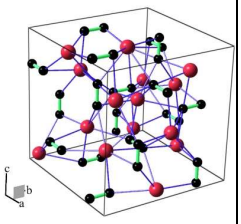
Compound		Lattice parameters	Space group	Structure - U/Pu ; - C
$UC_{1\pm x}$	$UC_{1.0}$	4.9605 Å	NaCl-FCC O_h^5 – Fm3m (Nr. 225)	
	$UC_{0.93}$	4.9563 Å		
UC_2 above 2038K		a = 5.488 Å		
UC_2 below 2038K	U-rich	a = 3.519 Å; c = 5.9787 Å	CaC_2-tetragonal D_{4h}^{17} – I4/mmm (Nr. 139)	
	C-rich	a = 3.5241 Å; c = 5.9962 Å		
U_2C_3		808.99 pm	BCC - 8 molecules per unit cell T_d^6 – $I\bar{4}3d$ (Nr. 220)	

Table 2: Uranium carbon compounds and characteristics (D. Manara, F. de Bruycker et al., submitted to comprehensive nuclear materials)

Despite the significant number of studies carried out on this phase diagram, uncertainties and questions remain. Part of the European F-Bridge project, to which some of the current research contributes, deals with these still open issues on the carbide fuel behaviour.

The data obtained from literature on the liquidus and solidus temperatures present a large dispersion of points. A series of experiments has been performed in the current PhD work to contribute to the determination of more accurate values. In order to accomplish this project, studies of eleven compositions of uranium carbon have been made in the range composition from C/U = 0.8 to C/U = 2.1.

4.4 The plutonium - carbon phase diagram

The plutonium carbon phase diagram is shown figure 6, four stable Pu-C compounds have been identified: Pu_3C_2, PuC_{1-x}, Pu_2C_3 and PuC_2 (table 3).The Pu-rich solid region is characterized by the six allotropies of Pu stable from room temperature to the melting point of ε-Pu at (910 ± 5) K[31]. The allotropic temperatures of pure Pu are not influenced by C additions, consistently with the negligible solubility of C in all the different Pu forms. The melting temperature of ε-Pu is reported to decrease by 8 K upon addition of C traces. The allotropies of pure Pu will not be treated in any further detail here. The two phase region extends to 40 at % C, corresponding to the composition Pu_3C_2. This compound (the so called ζ-phase) was observed already by researchers in the beginning of the 1960's, but its structure has not been determined yet. Pu_3C_2 decomposes into Pu+PuC at 848 K. Despite similarities in the crystal structures of carbides of uranium and plutonium, the phase diagrams of these two systems are very different. The main reason of this difference comes from the lower stability of plutonium monocarbide. It is always a hypo-stoichiometric compound whose homogeneity extends only to the narrow composition range $0.74 \leq C / Pu \leq 0.94$. Contrarily, UC is almost a line compound up to ~ 1400 K and has a very wide non-stoichiometry in the temperature range ~ 2300 to 2700 K. PuC_{1-x} decomposes peritectically into Pu_2C_3 + liquid at 1900 K. Pu_2C_3 is probably the most stable compound in the Pu-C system. It also melts peritectically at 2300 K and decomposes into PuC_2 + liquid. It has a small non-stoichiometry which is not very well established. Like UC_2, tetragonal PuC_2 is also stable in a narrow temperature range.

This phase, also called α-PuC_2, can be quenched to room temperature as a metastable phase, and was observed to transform into fcc KCN –like by Harper et al. around 1983 K[32].

The Pu-C system has been recently critically reviewed by Fischer, who proposed a phase diagram based on Gibbs energy CALPHAD optimization[33]. Fischer's phase diagram is shown in figure 6 but it has been corrected to fit experimental values of the temperature, rather than values obtained by Gibbs energy optimization. Also, the high-temperature C-rich part of Fischer's phase diagram has been slightly corrected to take into account the α-PuC_2 →β - PuC_2 transition detected by Harper et al. around 1983 K[32]. β - PuC_2 is assumed to melt congruently around (2520 ± 30) K, according to Marcon's phase diagram[34]. This behavior implies the existence of a PuC_2 – C eutectic in agreement with Fischer's Gibbs energy calculations. This eutectic has never been experimentally investigated until now, although Marcon's Pu partial pressure measurements show that the liquid formation temperature remains probably constant for a certain composition range between PuC_2 and pure C.

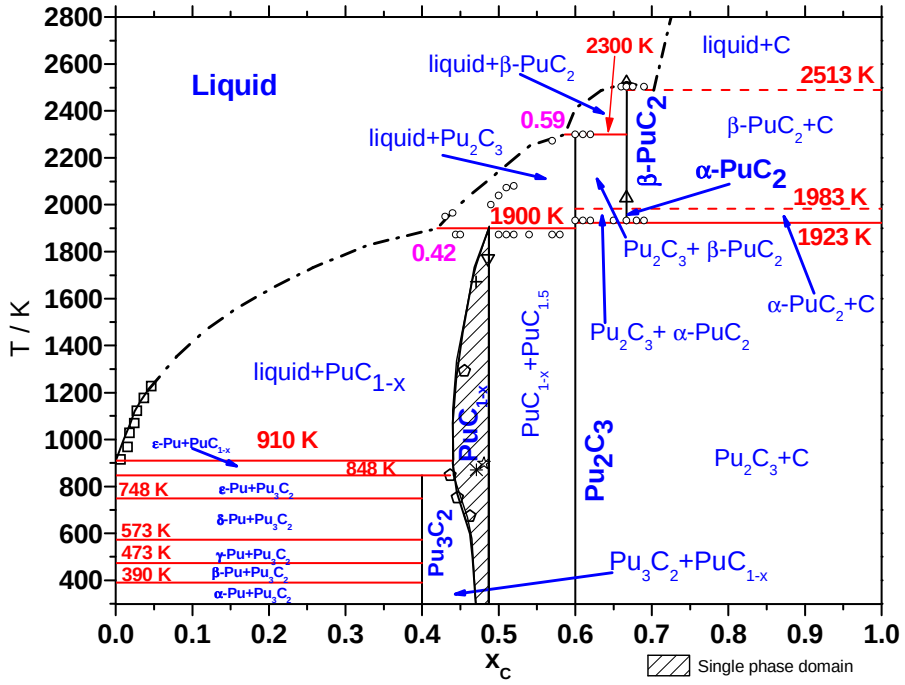


Figure 6: The plutonium carbon phase diagram

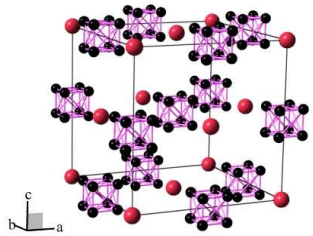
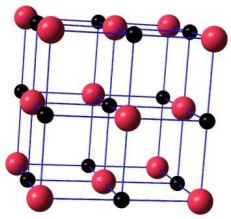
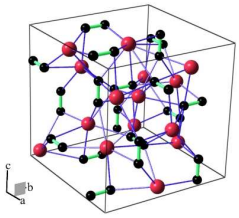
Compound	Lattice parameters	Space group	**Structure**  **- U/Pu ;**  **- C**
PuC_2	a = 3.63 Å; c = 6.094 Å a = 5.72 Å (2023 K)	KCN-FCC $\mathbf{O_h^5 - Fm3m\ (Nr.\ 225)}$	
PuC_{1-x}	a=498.13–1.50·(1–C/Pu) pm	NaCl-FCC $\mathbf{O_h^5 - Fm3m\ (Nr.\ 225)}$	
Pu_2C_3	812.1 ≤ a ≤ 813.4	BCC - 8 molecules per unit cell $\mathbf{T_d^6 - I\bar{4}3d\ (Nr.\ 220)}$	

Table 3: Uranium carbon compounds and characteristics

The experiments carried out for this PhD thesis were focused on the two compounds PuC_{1-x} and Pu_2C_3. These studies were needed to complete the literature data. Only few authors[35] proposed some measured values for the liquidus and the calculated phase diagrams[33] do not perfectly fit these points. Knowledge of both the uranium - carbon and plutonium - carbon phase diagrams is also the starting point for the investigation of the ternary uranium-plutonium carbon phase diagram.

5 References – Chapter 1

1 U. S. DOE Nuclear Energy Research Advisory Committee and the Generation IV international forum, "A Technology Roadmap for Generation IV Nuclear Energy System", December 2002.

2 R. W. Grimes, R. J. M. Konings and L. Edwards, Nature Materials 7 (2008) 683.

3 R. W. Ohse, Pure and Appl. Chemistry 60 (1988) 309.

4 R.W. Ohse, J.-F. Babelot, A. Frezzotti, K. A. Long, J. Magil, High Tern.-High Press., l2 (1980) 537.

5 R. W. Ohse and P. R. Kinsman, High - Temp. High - Press. 8 (1976) 209.

6 J. Magill, G. Pfennig and J. Galy, "Karlsruher Nuklidkarte", Report EUR 22276 EN, 2006.

7 Hj. Matzke, "Science of advanced LMFBR fuels", North Holland, 1986.

8 H. Holleck and H. Kleykamp, "Uranium Carbides" Gmelin Handbook of Inorganic Chemistry U, Supplement Volume C12, Springer-Verlag 1987.

9 D. Olander "Nuclear Fuels – Present and Future", J. Nucl. Mater. 389 (2009).

10 W. L. Lyon and W. E. Baily, J. Nucl. Mater. 22 (1967) 332.

11 E. A. Aitken, S. K. Evans , A thermodynamic data program involving plutonia and urania at high temperatures, GEAP-5672, General Electric, 1968.

12 M. G . Adamson, E. A. Aitken and R. W. Caputi, J. Nucl. Mater. 130 (1985) 349.

13 J. J. Carbajo, G. L. Yoder, S. G. Popov and V. K. Ivanov, J. Nucl. Mater. 299 (2001) 181.

14 C. Guéneau, C. Chatillon and B. Sundman, J. Nucl. Mater. 378 (2008) 257.

15 M. Kato, K. Morimoto, H. Sugata, K. Konashi, M. Kashimura and T. Abe, J. Nucl. Mat., 373 (2008) 237.

16 J. M. Haschke, T. H. Allen, L. A. Morales, Science, 287 (2000) 285.

17 R. C. Eckhardt, Los Alamos Science 26 (2000) 464.

18 G. K. Johnson, E. H. Van Deventer, O. L. Kruger, W. N. Hubbard, R. J. Lemire, J. Fuger, H. Nitsche, P. E. Potter, M. H. Rand, J. Rydberg, K. Spahiu, J. C. Sullivan, W. J. Ullman, P. Vitorge and H. Wanner (2001), OECD, Chemical Thermodynamics Series - Chemical Thermodynamics of Neptunium and Plutonium, vol. 4, Elsevier, North-Holland.

19 C. Rodriguez, Nuclear Engineering and Design 222 (2003) 299.

20 T. D. Chikalla, C. E. McNeilly, J. L. Bates and J. J. Rasmussen, *Int. Colloquium on Study of Crystal Transformations at High Temperatures above 2000 K*, Odeillo, France, 1971 *(Centre National de la Recherche Scientifique, 75, Paris, 1972)* p. 351.

21 K. Richter and C. Sari, J. Nucl. Mater. 148 (1987) 266.

22 A. K. Sengupta, U. Basak, A. Kumar, H. S. Kamath, S. Banerjee, J. Nucl. Mater. 385 (2009) 161.

23 P. Guinet, H. Vaugoyeau and P. L. Blum, *"Métallographie – Sur le système binaire uranium-monocarbure d'uranium"*, C. R. Acad. Sc. Paris, t.261 (2nd August1965) Groupe 7 p. 1312-1314.

24 H. Holleck and H. Kleykamp, "Uranium Carbides", Gmelin Handbook of Inorganic Chemistry U, Supplement Volume C12, Springer-Verlag 1987.

25 A. L. Bowman, G. P. Arnold, W. G. Witterman, T. C. Wallas N. G. Neresson, Acta. Cryst. 21 (1966) 670.

26 U. Benedict, J. Less Common Metals 128 (1987) 7.

27 E. A. Harper, H. J. Hedger, J. T. Dalton, Nature 219 (1968) 151.

28 M. B. Sears, L. M. Ferris, J. Nucl. Mater. 32 (1969) 10.

29 J. Laugier, P. L. Blum, J. Nucl. Mater. 39 (1971) 245.

30 E. Fischer, P. Y. Chevalier, J. Nucl. Mater. 288 (2001) 100.

31 R. D. Baker, S. S. Hecker, D. R. Harbur, "Plutonium: A Wartime Nightmare but a Metallurgist's Dream". Los Alamos Science (Los Alamos National Laboratory): 148 (1983) 150.

32 E. A. Harper, H. J. Hedger and J. T. Dalton, Nature 219 (1968) 151.

33 E. Fischer, CALPHAD 32 (2008) 371.

34 J. P. Marcon, J. of Inorg. Nucl. Chem. 32 (1970) 2581.

35 J. G. Reavis, L. Reese, Quaterly Status Report on the Advanced Plutonium Fuels Program, April 1 to June 30, Los Alamos Scientific Laboratory of the University of California, LA-4494-MS, Project 463, (1970).

Chapter 2: Experimental

1 Laser heating experiment

Measurements of thermophysical properties at high temperatures are hampered by the enhanced reactivity of materials, particularly in the liquid state, as well as increased heat transfer, vaporization, loss of mechanical strength etc. These experimental difficulties steadily grow with temperature, just like the kinetics of some of those undesired phenomena, placing severe limitations on steady-state and quasi-steady-state techniques. Limiting the time during which the investigated materials are subjected to high temperatures is one way of overcoming, or at least reducing, some of these limitations. This, as well as advances in sensor technology and high-speed instrumentation, has been driving the development of modern sub second pulse-heating techniques [1-3]. These techniques can be traced back to the late 1960s and the pioneering work at the U.S. National Bureau of Standards (presently National Institute of Standards and Technology). Combining these two principles, namely short measurement duration and containerless conditions, a technique has been developed[4] in recent years at ITU with the specific goal of investigating nuclear materials at very high temperatures and particularly around their solid-liquid transition (figure 1).

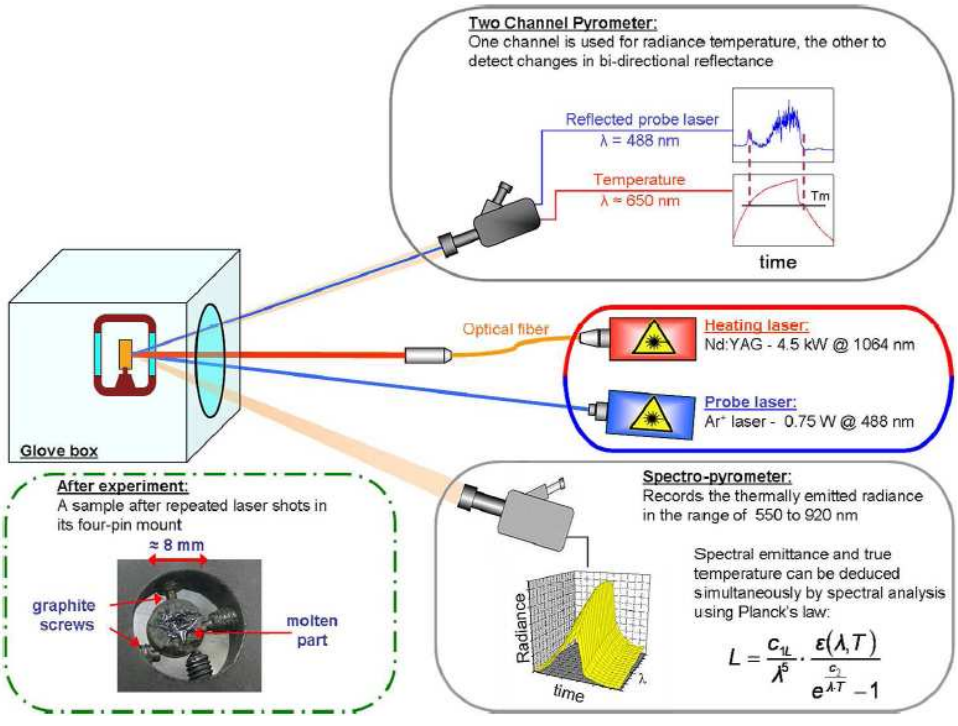
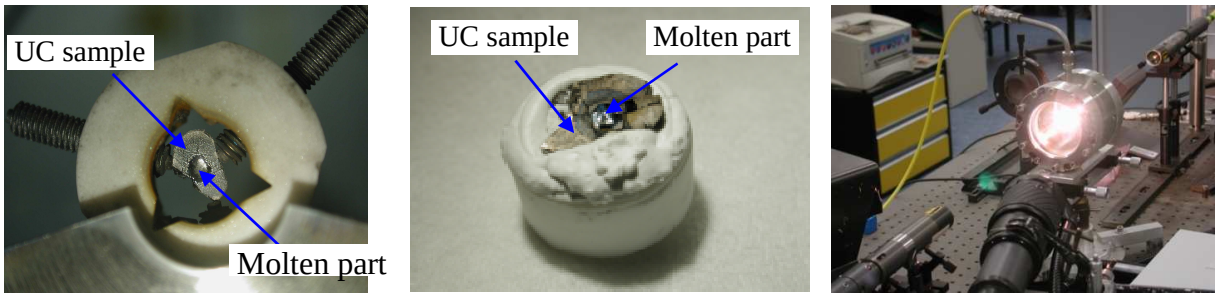


Figure 1: Schematic of the laser heating setup employed in this research

In a typical experiment, the sample is mounted inside an autoclave with controlled atmosphere. The surface of the sample is laser-heated above its melting transition and left to cool naturally. The temperature is measured with a fast pyrometer and classic thermal analysis is then applied on the cooling part of the recorded thermogram for the determination of phase boundaries. Deviations from a smooth curve may reveal phase changes, a freezing plateau being the most prominent example. For measurements on α-emitting radioactive materials, the autoclave is placed inside a Plexiglas glove box that provides adequate shielding. The non-contact character of laser-driven heating and of optical diagnostics, in general, is then of great advantage as it simplifies glove box design by reducing the number of the necessary feedthroughs.

1.1 Sample holder

Depending on the size and shape of the sample, it is either supported in a 3- or 4-pin mount, in practice realized by graphite or tungsten screws (Figs. 1 and 2a), or fixed in an alumina ring using a Cotronics® high temperature resistant ceramic glue (Fig. 2b). The autoclave (Fig. 2c) allows performing heat treatments under appropriate gases with a maximum pressure of 0.25 MPa in order to limit vaporization. By focusing the laser onto a spot that is smaller in diameter than the sample surface, only a limited area in the central part of the sample surface is melted. The surrounding part of the sample is still solid in both the radial and the axial directions, and is considerably cooler the further it is from the laser-irradiated area. This solid part of the sample itself can be considered to form a kind of “self-crucible”, assuming the role of a buffer that insulates the area of interest from the sample holder. It thereby effectively establishes containerless conditions in the sense that no contamination with foreign material takes place in that area.



(a) **(b)** **(c)**

Figure 2: Uranium carbide sample (a) supported in a 3-pin mount, or (b) held in place by ceramic glue, and (c) laser-heated to a high temperature.

1.2 Heating agent

The core component of the current setup is an industrial-strength, continuous-wave Nd:YAG laser operating in the near infrared (1064 nm). Its high maximum power of 4.5 kW, coupled with the surface-heating character of a laser impinging on an opaque material, allows achieving heating rates on the order of 10^5 K·s^{-1} and temperatures exceeding 3000 K in a few tens of milliseconds. The laser power *vs.* time profile (length and power) is programmable with 1 ms resolution via a computer, and fast pulses can therefore be generated. The heating and cooling rates are adapted to the needs of each experiment, with a time scale varying from some milliseconds to several minutes or longer. Going through an optical fiber, the laser beam is focused on the sample surface with a spot diameter varying between 3 and 8 mm depending on of the lenses used.

1.3 Pyrometry and temperature measurement

a) Theoretical Background

Optical pyrometry is practically the only temperature measurement technique available for the fast measurement (sub-millisecond resolution) of high temperatures (above 2000 K)[5]. Temperature is inferred from a measurement of the radiant flux thermally emitted by an area A on the sample defined by the pyrometer's measurement spot, into the solid angle of acceptance ω of the pyrometer, and within the wavelength interval $\Delta\lambda$ over which the instrument responsivity is significantly non-zero. If $\Delta\lambda$, i.e. the spectral bandwidth of the pyrometer, is sufficiently narrow, the instrument may be treated as quasi-monochromatic operating at some effective wavelength λ within $\Delta\lambda$. In addition, if A and ω are sufficiently small, the signal current i_p of the photon detector may be expressed as:

$$i_p(T) = \Theta \cdot \tau_{\lambda p} \cdot R_\lambda \cdot \Delta\lambda \cdot \tau_{\lambda w} \cdot L_\lambda(T) \tag{1}$$

with

$$\Theta = \iint_{A,\omega} \cos\theta \cdot d\omega \cdot dA \tag{2}$$

$\tau_{\lambda p}$ is the effective transmittance (including reflection losses) of all the optical elements of the pyrometer, $\tau_{\lambda w}$ is the effective transmittance of any optical windows between the sample and the pyrometer, R_λ is the flux responsivity of the detector (in units of A·W^{-1}), and $L_\lambda(T)$ is

the spectral radiance thermally emitted by the sample at temperature T and wavelength λ into ω. Θ is the throughput of the beam collected by the pyrometer optics, also called its étendue, in the direction θ, defined by the polar angle between the normal to the sample surface and the direction of emission.

The spectral radiance L_λ is defined[6] at a point on a surface in the direction of a ray through that point as the radiant power Φ within an infinitesimal wavelength interval $d\lambda$ per unit projected area perpendicular to the ray and unit solid angle in the direction of the ray at that point:

$$L_\lambda = \frac{d^3\Phi}{dA \cdot \cos\theta \cdot d\omega \cdot d\lambda} \tag{3}$$

Planck's radiation law establishes a link between the spectral distribution of radiance emitted by an incandescent body and its temperature. For so-called blackbodies and in terms of the 'local' wavelength λ in a medium with refractive index n it takes the form:

$$L_{\lambda b}(T) = \frac{c_{1L}}{n^2 \cdot \lambda^5}\left[\exp\left(\frac{c_2}{n \cdot \lambda \cdot T}\right) - 1\right]^{-1} \tag{4}$$

where $c_{1L} = 2 \cdot h \cdot {c_0}^2$ is the first radiation constant (for radiance L) and $c_2 = h \cdot c_0 \cdot k_B$ is the second radiation constant. c_0 is the speed of light in vacuum, h is Planck's constant of action, and k_B is the Boltzmann constant. It should be noted that c_{1L} is related to c_1, the first radiation constant for exitance usually encountered in literature, by $c_1 = \pi \cdot c_{1L}$. For the purposes of the present work, the index of refraction was always taken to be equal to 1, whereas a value[7] of 14388 $\mu m \cdot K$ was used for c_2.

A blackbody is a surface (material or geometrical) that absorbs all radiant flux of all wavelengths and polarizations incident upon it from all possible directions. For a prescribed temperature and wavelength, no surface can emit more thermal radiation than a blackbody. Furthermore, a blackbody is an isotropically diffuse (lambertian) emitter, i.e. the radiation emitted by it is independent of direction. Although there is no real surface that precisely has these properties, the concept of a blackbody is useful in describing the radiative characteristics of real surfaces. The closest approximation to a blackbody surface is given by the aperture of a cavity (an opaque enclosure) whose inner surface is at uniform temperature.

The ability of a real surface to emit thermal radiation, as compared to that of a blackbody at the same temperature, is expressed in terms of its spectral-directional emissivity[(1)] ε_λ:

$$L_\lambda(T) = \varepsilon_\lambda(T) \cdot L_{\lambda b}(T) \tag{5}$$

As the name implies, ε_λ, and therefore also L_λ, will generally depend on the direction of emission, in addition to its spectral and temperature dependence. For emission in the direction of the surface normal ($\theta = 0°$), in particular, it is called normal spectral emissivity. For near-normal emission (θ up to approximately 20° for metallic materials, up to larger angles for non-metallic materials) ε_λ is very nearly constant and equal to the value of the normal spectral emissivity[8]. Since pyrometers in the present work were always set up near-normal with respect to the sample surface, the angle dependence of ε_λ was not considered and, unless explicitly stated otherwise, 'emissivity' will always refer to normal spectral emissivity.

A practical approximation to Planck's law, accurate to better than 1% for wavelength-temperature products $\lambda \cdot T \leq 3100\ \mu\text{m} \cdot \text{K}$, is Wien's law:

$$L_{\lambda b}(T) = \frac{c_{1L}}{\lambda^5} \exp\left(-\frac{c_2}{\lambda \cdot T}\right) \tag{6}$$

For non-blackbodies:

$$L_\lambda(T) = \varepsilon_\lambda(T) \cdot \frac{c_{1L}}{\lambda^5} \exp\left(-\frac{c_2}{\lambda \cdot T}\right) \tag{7}$$

A very useful concept in pyrometry is that of radiance temperature T_λ. This is the temperature measured directly by a pyrometer that has been calibrated in terms of blackbody radiance. In other words, it is the temperature measured by a pyrometer assuming that the emissivity of the target is equal to unity (perfect blackbody radiator). It is related to true temperature, within the range of validity of Wien's law, by

---

[(1)] Emissivity is the term normally reserved for the intrinsic property of the bulk material, which is function of its electronic and vibrational structure. Emittance, on the other hand, refers to an extrinsic property, which of course depends on the emissivity of the material, but also on its surface morphology (i.e. roughness). An extreme example would be a blackbody cavity that has an emittance very close to unity even though the material is is constructed of can have a significantly lower emissivity. For an optically smooth, perfectly clean surface emittance and emissivity are identical. However, most often in literature emissivity is used regardless of the surface morphology and this practice is adhered to also in the present work.

$$\frac{1}{T} - \frac{1}{T_\lambda} = \frac{\lambda}{c_2} \ln \varepsilon_\lambda \tag{8}$$

as can easily be verified by setting $L_{\lambda b}(T_\lambda) = L_\lambda(T)$ and combining Eqs. 6 and 7. Since for non-blackbodies ε_λ is always lower than unity, it follows that $T_\lambda < T$ and that the difference between the two depends on the operating wavelength of the pyrometer.

b) Fast two-channel pyrometer

Two pyrometers have been used during this thesis. Both are two-channel pyrometers utilizing logarithmic amplifiers. They are used to measure simultaneously the radiance temperature of the sample surface close to 650 nm and the Reflected Light Signal (RLS) of a Ar^+ probe laser at 488 nm. The first pyrometer, described in detail in Ref. 9, is equipped with an adjustable grating system that allows tuning the two radiation detectors at different wavelengths in the visible range. The second one is a newer instrument with fixed operating wavelengths. It is more compact and, therefore, more suitable for use in tight spaces, such as when a glovebox is set up on the optical table for measurement on active samples. This latter pyrometer is described in the following paragraphs.

A simplified functional block diagram is shown in Figure 3. The dynamic range of the logarithmic amplifiers LOG1 and LOG2 allows an operational temperature range from 1750 to 6000 K with a temporal resolution of 10 μs (settling time to 1% of log outputs). The objective lens (2) collects thermal radiation from an area of 0.5 mm nominal diameter on the sample (1) at a working distance of about 400 mm from it. It focuses this light onto a tilted mirror (4) with a central pinhole that acts as the system's field stop. A folding mirror (8) reflects the image of the sample, which is formed on the pinhole mirror (4), into a telescope (3) for visual alignment on the sample area of interest. Light passing through the field stop is collimated by a lens (6) and spectrally split into two beams by a dichroic mirror. Each of these beams passes through an interference filter before being detected by a Si photodiode. The channel used for temperature measurements is centered about 650 nm with a bandwidth of 27 nm, whereas the channel used for the RLS detection is tuned to the laser wavelength of 488 nm with a bandwidth of 7 nm. The photodiodes are mounted in a bulk metal case that is maintained at constant temperature by a high-precision miniature thermostat with a microprocessor controller.

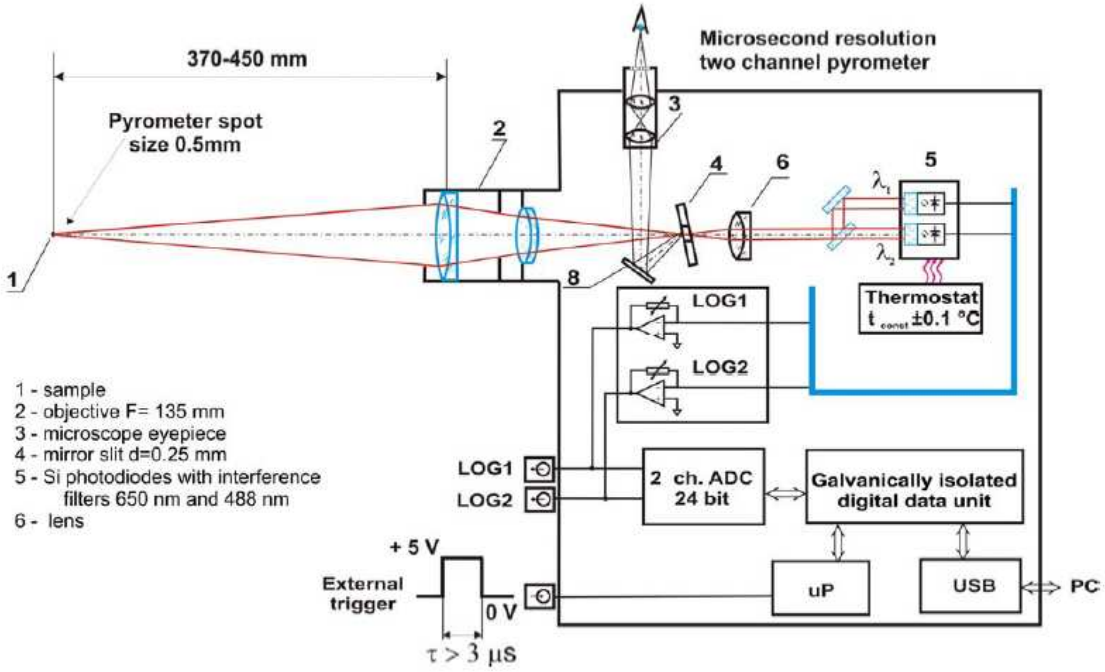


Figure 3: The simplified functional block diagram of the pyrometer

The signal currents of the two photodiodes are converted into voltage output signals by the logarithmic amplifiers, which are then recorded on a Nicolet Pro® 44C digital oscilloscope with a maximum sampling rate of $5 \cdot 10^6$ samples$\cdot$s^{-1}. For the temperature channel this output signal may be expressed, within the sample temperature range for linear operation, as:

$$V_{out}(T) = k_{\log} \cdot \log\left[\frac{i_{ref}}{i_p(T)}\right] \tag{9}$$

where $k_{\log}$ is the scaling constant of the amplifier, i.e. its gain in units of V/decade, and i_{ref} is a reference current internal to the amplifier integrated circuit. In terms of the sample temperature T or radiance temperature T_λ a working equation is obtained by combining Eqs. (1), (7), and (9):

$$V_{out}(T) = A + \frac{B}{T} - k_{\log} \cdot \log[\tau_{\lambda w} \cdot \varepsilon_\lambda(T)] = A + \frac{B}{T_\lambda} - k_{\log} \cdot \log[\tau_{\lambda w}] \tag{10}$$

$$A = k_{\log} \cdot \log\left(\frac{i_{ref}}{\Theta \cdot \tau_{\lambda p} \cdot R_\lambda \cdot \Delta\lambda} \cdot \frac{\lambda^5}{c_{1L}}\right) \tag{11}$$

$$B = k_{\log} \cdot \log e \cdot \frac{c_2}{\lambda} \tag{12}$$

A and *B* are instrument constants determined by calibration, *e* is the base of the natural logarithm (*e*=2.7182818).

c) Calibration

Two Polaron® lamps with 2 mm-wide tungsten ribbon filaments were used for pyrometer calibration. A type 22/V vacuum lamp (serial no. P224c) was used in the range of 1100 to 1800 K, whereas a type 22/G argon-filled lamp (serial no. P213c) was used from 1800 to 2500 K. The lamps had been calibrated in 1997 by KR Technologie GmbH Stuttgart and were calibrated again in 2010 by the Physikalisch-Technische Bundesanstalt in Berlin in terms of their radiance temperature at 650 nm as a function of filament current.

For calibration, the pyrometer and the lamp are set up on an optical table. The lamp is adjusted so that the tungsten ribbon is vertical. A sighting pointer inside the lamp indicates the correct position for calibration halfway along the ribbon's midline (Figure 4). The pyrometer is focused on it and the lamp is rotated about its vertical axis to ensure that the pyrometer's optical axis is perpendicular to the ribbon. A mark on the back side (i.e. away from the pyrometer) of the lamp's glass bulb serves as a visual aid in this.

A stable constant-current power supply is used to heat the tungsten ribbon. The current is slowly increased up to the first calibration temperature on the lamp's certificate. A slight re-alignment of the pyrometer is necessary at this point because of the ribbon's thermal expansion. This is important in view of the significant temperature gradient away from the position indicated by the sighting pointer toward the cooler filament supports. The signal of the pyrometer is recorded with the Nicolet and transferred to a PC through GPIB using NI LabView® software. The current is then increased to the next point on the calibration certificate and the procedure is repeated up to the highest calibration temperature of the lamp. The pyrometer is shielded from the lamp when not taking data to prevent the pyrometer's optical components from heating up during calibration.

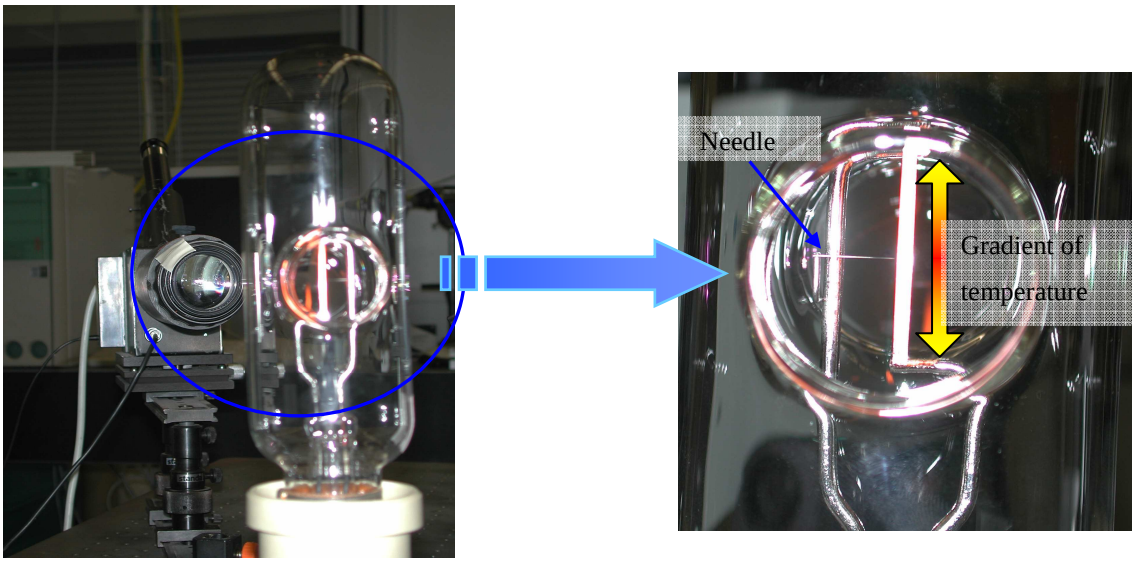


Figure 4: Alignment of the pyrometer on the calibration lamp.

Since no optical window is used between the lamp and the pyrometer during calibration, Eq. (10) becomes:

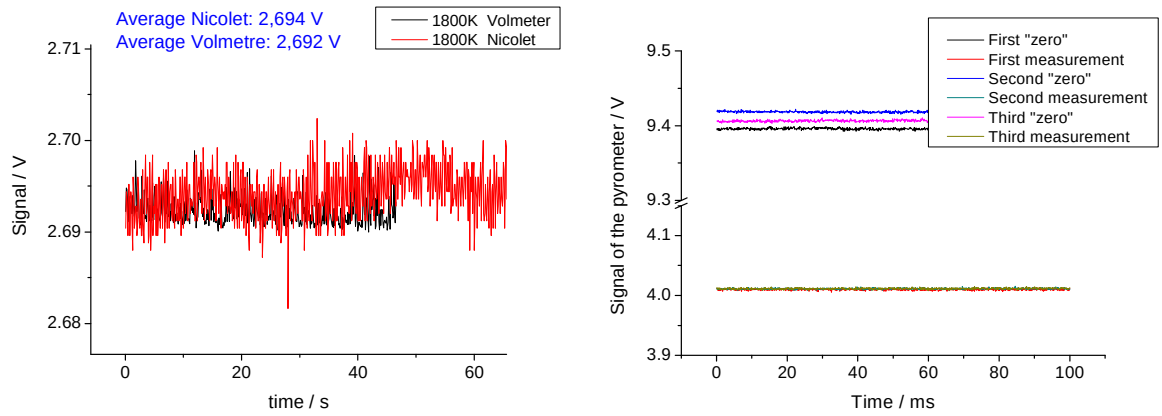
$$V_{out}(T) = A + \frac{B}{T_{\lambda}} \tag{13}$$

The linear dependence of the output signal on the inverse radiance temperature of the lamp is exploited to derive the instrument constants A and B by means of a linear least-squares fit. Using Eq. (12), the effective wavelength of the pyrometer is then computed from the slope of the fit.

Sapphire windows are typically used in the optical ports of the autoclave and of the glovebox. Even though sapphire is highly transparent in the visible range, its higher index of refraction, as compared for instance to BK7 glass, leads to increased reflectance losses. Therefore, the effective transmittance of a sapphire window at the pyrometer wavelength was measured by inserting it between the pyrometer and the lamp at a radiance temperature of 2000 K. A value of 0.857 was determined, in excellent agreement with the value calculated directly from the index of refraction of sapphire at 650 nm. The angle dependence of this window transmittance was also studied because the pyrometers are normally set up slightly off-normal with respect to the sample and window. It was found, that this angle dependence is insignificant for the purposes of this work, as corroborated by index-of-refraction-based calculations.

Measurements were performed with the ceiling lights on and off to check for any effect of background light on the calibration, but no difference was noticed.

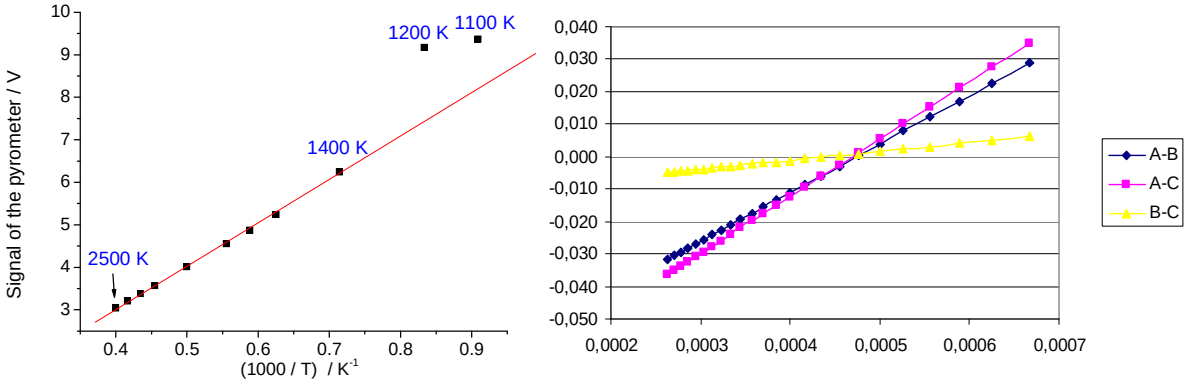
In order to check the offset stability with respect to the internal noise of the oscilloscope, this signal was compared to that obtained with a simple voltmeter without interface (Fig. 5a) and the difference observed was about 2 mV which is negligible. Electronic fluctuations can be visible through slight variations of the offset signal. To quantify this effect, different series of measurements are performed at regular intervals; both the zero and the radiance of the lamp were measured each time during 1 minute. Even if the offset (zero) varied the radiance measured was always identical (Fig. 5.b).



(a) (b)

Figure 5: (a) Comparison of signals recorded with the oscilloscope and a voltmeter. (b) Pyrometer signal recorded on three different occasions with the lamp at 1800 K. Even though the "zero"-offset of the pyrometer varied, the "on"-signal was highly reproducible.

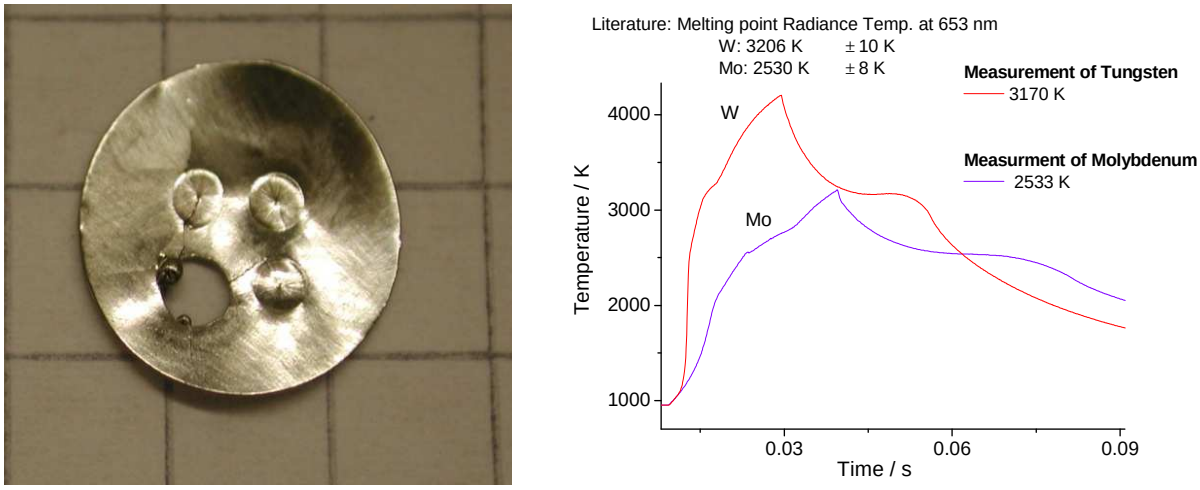
The calibration equation of the pyrometer was obtained by recording its voltage signal for different temperatures with the two calibration lamps from 1100 to 2500 K (Figure 6.a). If it appears that the pyrometer response is not linear below a certain temperature, its effective operational domain must be accordingly reduced. Thus three equations of calibration are established by fitting the measured points for different temperature ranges, namely A, B and C. These equations are respectively obtained between 1400 and 2500 K, 1800 and 2500 K, and 2200 and 2500 K. The deviations from one to the others are plotted Figure 8.b. From these results it can be considered that the pyrometer response is linear already from at least 1800 K.



(a) (b)

Figure 6: (a) Pyrometer signal vs. inverse lamp temperature during calibration. (b) Difference between calibration equations covering different temperature ranges.

The highest lamp-based calibration temperature is 2500 K, but most temperatures of interest in the present work are higher. This means that the calibration equation has to be extrapolated. At 3000 K, uncertainties of ±1% (typical for the current equipment) already correspond to ±30 K. It is therefore important to check the actual temperature accuracy by measuring well-established melting points in the same temperature range. The radiance temperatures on melting of molybdenum and tungsten can serve as secondary reference points for high-temperature pyrometry[10], and were used to check in-situ the obtained pyrometer calibration.



(a) (b)

Figure 7: (a) A molybdenum foil on which four laser shots were performed. (b) Measured thermograms on molybdenum and tungsten.

Because of the significant thermal conductivity of these materials, thin foils (about 0.1 mm thick) were used. The 1 cm diameter allowed performing laser shots at several positions on the same sample (Fig. 7a). Argon atmosphere of about 2 bar pressure was used to minimize oxidation. The difficulty was to melt enough matter to get a pronounced thermal

arrest without burning a hole through the samples. Figure 7b presents thermograms obtained with the molybdenum and tungsten samples. Long and horizontal freezing plateaus were obtained. The agreement of the measured melting-point radiance temperatures with the widely accepted values at 653 nm was generally very good, on the order of 0.5%. Nonetheless, it was often noticed that the measured temperatures were lower than the published values. This can be caused by insufficient purity of the samples, as well as by the presence of an oxide layer on their surface. However, some dependence of the deviation on the experimental parameters (mainly the laser spot size, the laser power, and the heating pulse duration) was also noticed. A series of experiments was designed to examine whether the so-called size-of-source effect could also have contributed to the observed differences.

d) The size-of-source effect

The temperature reading of every pyrometer depends to some extent on the size of the source it is aiming at. In other words, sources of equal temperature but different size will give rise to different apparent temperatures[11]. This is, of course, clear if the source underfills the nominal measurement spot of the pyrometer. However, it is also the case with larger sources and is referred to as the size-of-source effect (SSE). The SSE is caused by the effects of straylight originating from diffraction, inter-reflections between optical elements or between surfaces of the same optical element (e.g. a lens or a window), scattering at imperfections of optical components and dust particles on them, and from optical aberrations inherent in the imaging elements[12]. The combined effect is that part of the radiation from the nominal target spot of the pyrometer is lost and, conversely, part of the radiation originating from the surroundings is measured by the detector. The balance is only null in case of equal radiance temperatures between target and surroundings. For pyrometers optimized for high-temperature measurements the output signal generally increases as the diameter of the hot target increases beyond the nominal measurement spot[12].

In laser-driven melting experiments large temperature gradients are generated on the sample. The area of uniform temperature is limited to the center of the laser spot and surrounded by considerably colder parts. As soon as the laser power is reduced to initiate cooling and, subsequently, freezing of the molten area, the size of the uniform-temperature area decreases and may quickly become comparable to the nominal measurement spot.

Depending on the laser spot diameter, which is the dominant factor determining the initial size of the uniform temperature area on the sample when cooling starts, and the magnitude of the SSE of the pyrometer, its reading will be affected by this process sooner or later along the thermogram. In the normal case this is simply noticed as the typical gradual transition from freezing-of-the-liquid to cooling-of-the-solid (instead of the ideal abrupt one), in other words an apparently shorter freezing plateau with a rounded end. It is conceivable that if the molten area on the sample is too small to begin with, the pyrometer reading will be influenced by the SSE earlier, in the worst case resulting in a noticeably lower freezing temperature and a "plateau" which is not ideally horizontal anymore but exhibits downward slope.

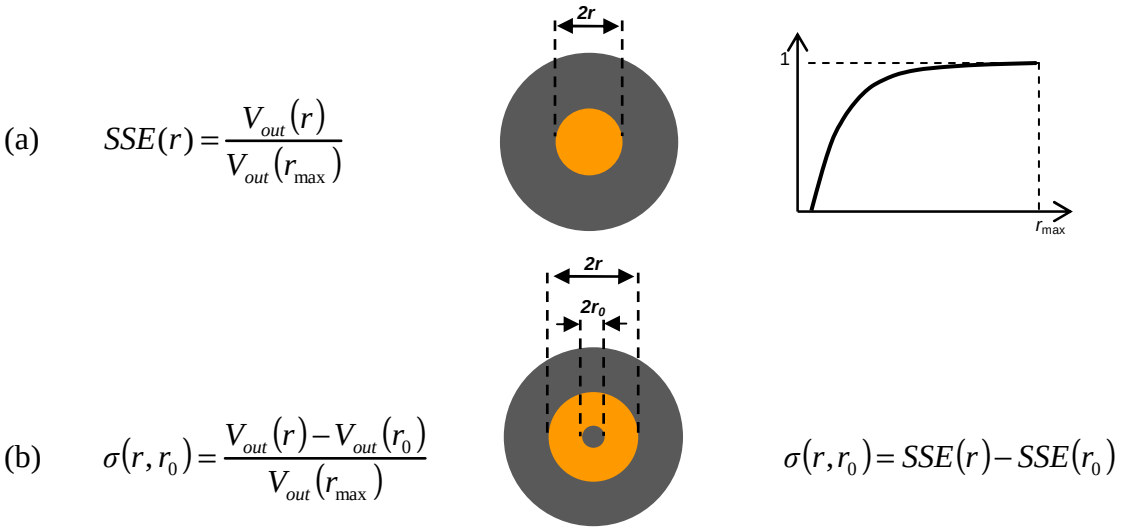
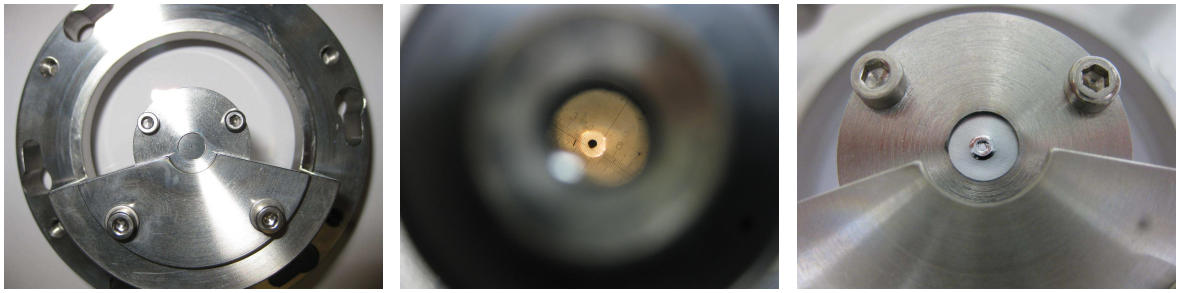


Figure 8: Methods for SSE evaluation: (a) direct, (b) indirect. In both cases the radius r of the aperture in front of the uniform radiance source is varied.

Estimating the influence the SSE can have on the measurement accuracy of our pyrometer required (i) its SSE to be measured and (ii) the radial temperature profile on the samples to be known for the laser parameters used in the molybdenum and tungsten shots. For the first part, a series of experiments were specially designed and performed. For the second part, numerical simulations of the molybdenum and tungsten measurements were performed in the frame of an ongoing collaboration with the group of Prof. M. Malki at the Polytech'Orléans and the CEMHTI-CNRS Orléans, and more recently also at ITU.

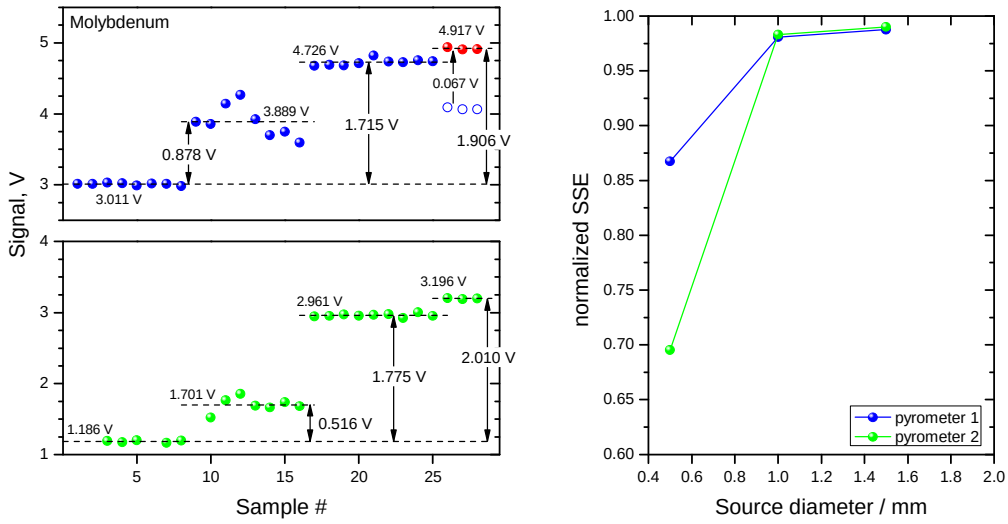
The SSE is usually determined using one of two techniques. The direct method is depicted schematically in Figure 8a. Apertures of various sizes are placed in front of a large, uniform radiance source. The pyrometer is focused on the center of the aperture each time and its output signal is recorded as a function of aperture diameter and normalized with respect to

the signal obtained with the largest aperture. The indirect method is explained in Figure 8b. The difference is that the pyrometer is now focused on a central obscuration that is placed in the center of the apertures. The size of this obscuration is slightly larger than the nominal measurement spot. Ideally, i.e. in the absence of any SSE, the output signal should be exactly zero. In reality it is not and the difference as a function of aperture diameter is a measure of the SSE. The indirect method generally yields lower uncertainties and has become the main method for SSE evaluations.



(a) (b) (c)

Figure 9: (a) Sample with ∅0.5 mm hole mounted in its holder. (b) Sample with ∅1.5 mm hole as seen through the pyrometer. The black spot indicates the measurement spot. (c) Sample with ∅1.0 mm hole after melting.



(a) (b)

Figure 10: (a) Pyrometer signals at the freezing temperature of molybdenum recorded on intact samples and on samples with a ∅0.5, ∅1.0, and ∅1.5 mm hole. (b) Normalized SSE derived from these measurements.

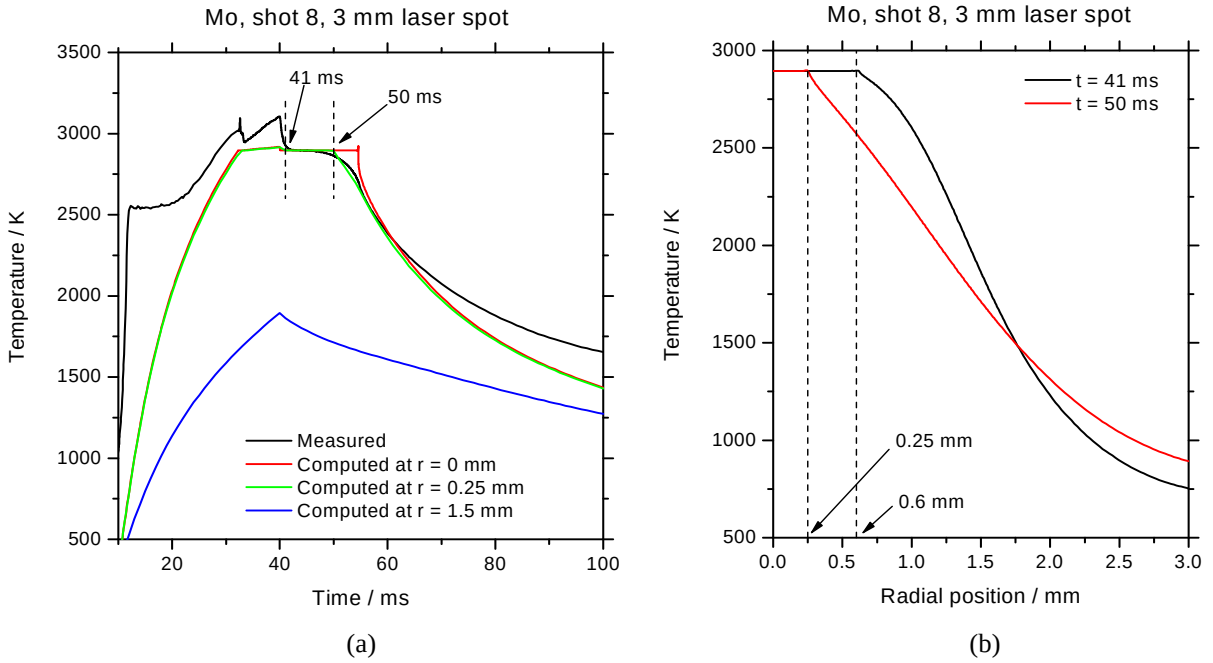
In order to measure the SSE of our pyrometer, a modified indirect technique was implemented in-situ. Thin molybdenum and niobium disks of 8 mm in diameter and 0.1 or 0.125 mm in thickness were used as samples. A hole of 0.5, 1.0, or 1.5 mm diameter was

drilled through their center. The samples were heated above their melting point with a large laser spot of about 5 mm in diameter centered every time on the hole. Measurements were taken along the freezing plateau with the pyrometer focused on the hole, as well. The signal at the freezing point was also measured on samples without the hole to serve as a reference. The difference was then a measure of the contribution to the signal of radiation emitted from the central sample area of 0.5 mm, 1.0 mm, or 1.5 mm in diameter. Figure 9 shows pictures of samples (a) in the sample holder, (b) as seen through the pyrometer, and (c) after melting. Figure 10 summarizes the current results for two different pyrometers. Pyrometer 1 with a nominal target spot of about 0.5 mm in diameter and pyrometer 2 with a 0.8 mm spot. The latter was not used in the present work but is shown here for comparison. It should be remembered that, according to Eq. (9), the measured signals are logarithmic and that they decrease with increasing radiance.

As already mentioned, the second piece of information necessary to compute the influence of the SSE on the temperature measurement under different conditions is the radial temperature profile on the sample during freezing. Simulated thermograms on molybdenum at various radial positions on the sample are shown in Figs. 11 and 12, for a laser spot diameter of 3 mm and 5 mm, respectively, together with the measured thermograms. In both cases, 30 ms-long square laser pulses were used. With the smaller spot the sample was irradiated with 2 kW, whereas a higher power of 3.5 kW was used with the larger spot. It should be noted that, because of the high laser irradiance and the significant reflectance of molybdenum (on the order of 70% at the laser wavelength), the reflected laser light is not completely rejected by the pyrometer giving rise to a high (~2500 K) apparent temperature of the sample very early in the shot. Only later in the thermogram does the thermal radiation exceed this background light significantly. However, this does not matter once the laser is switched off.

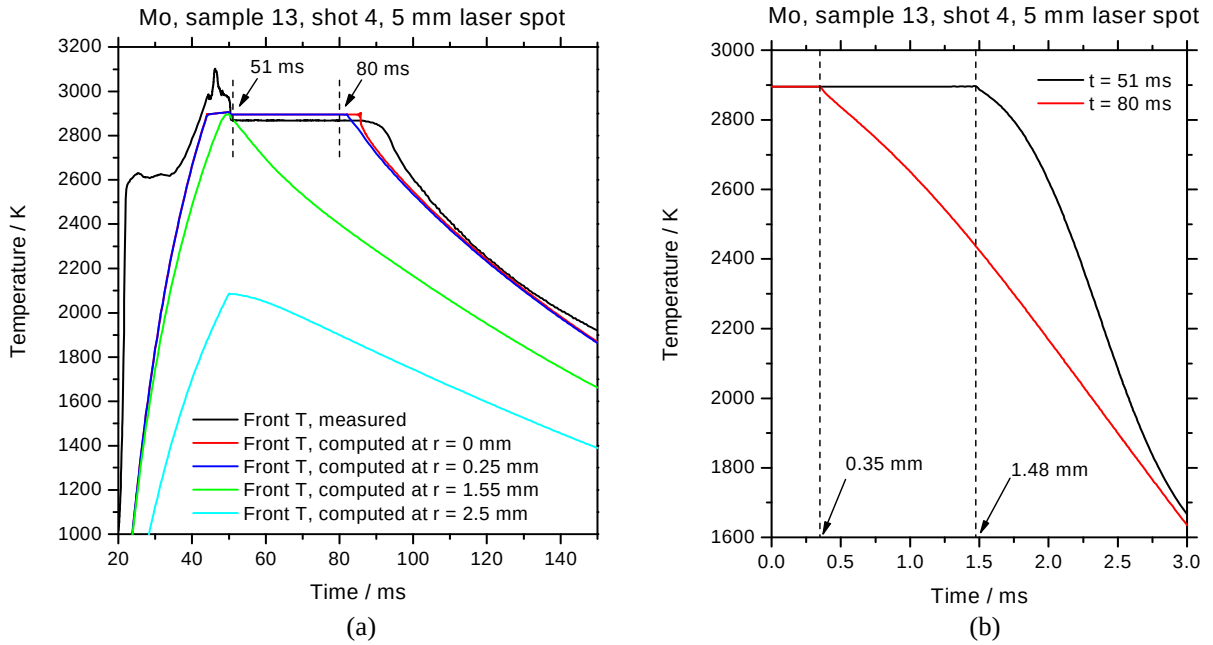
The agreement between the simulated thermogram in the center of the sample (r = 0 mm) and the measured one is fairly good, although there is still room for improvement. The significant radial temperature gradients on the sample are evident. For instance, at the onset of the freezing plateau the temperature at the edge of the laser-irradiated area is lower by about 1000 K. The right-hand plots in these figures show radial temperature profiles at two instances in time, near the beginning and the end of the freezing plateau. Near the end of the plateau, the area at uniform (freezing) temperature is of comparable size to the pyrometer measurement spot. At this point in time, just before the sample surface is completely frozen,

the pyrometer also “sees” colder areas on the sample indicating a progressively lower apparent temperature due to the SSE. This explains the rounded end of the measured plateau, which is not present in the simulated thermogram at the center.



(a) (b)

Figure 11: (a) Measured and simulated thermograms at various radial positions on a molybdenum sample that was heated with a 3 mm-diameter laser spot at 2 kW for 30 ms. The vertical dashed lines indicate the times at which the radial temperature profile is shown on the right. (b) Simulated radial temperature profiles near the beginning and the end of the freezing plateau.



(a) (b)

Figure 12: (a) Measured and simulated thermograms at various radial positions on a molybdenum sample that was heated with a 5 mm-diameter laser spot at 3.5 kW for 30 ms. The vertical dashed lines indicate the times at which the radial temperature profile is shown on the right. (b) Simulated radial temperature profiles near the beginning and the end of the freezing plateau.

Figure 13 shows the calculated temperature error at the melting points of molybdenum and tungsten due to the measured SSE. ΔT is shown as a function of the "effective" measurement spot size of the pyrometer, i.e. the area from which virtually 100% of the detected radiance originates. The difference between a 3 mm and a 5 mm laser spot is apparent.

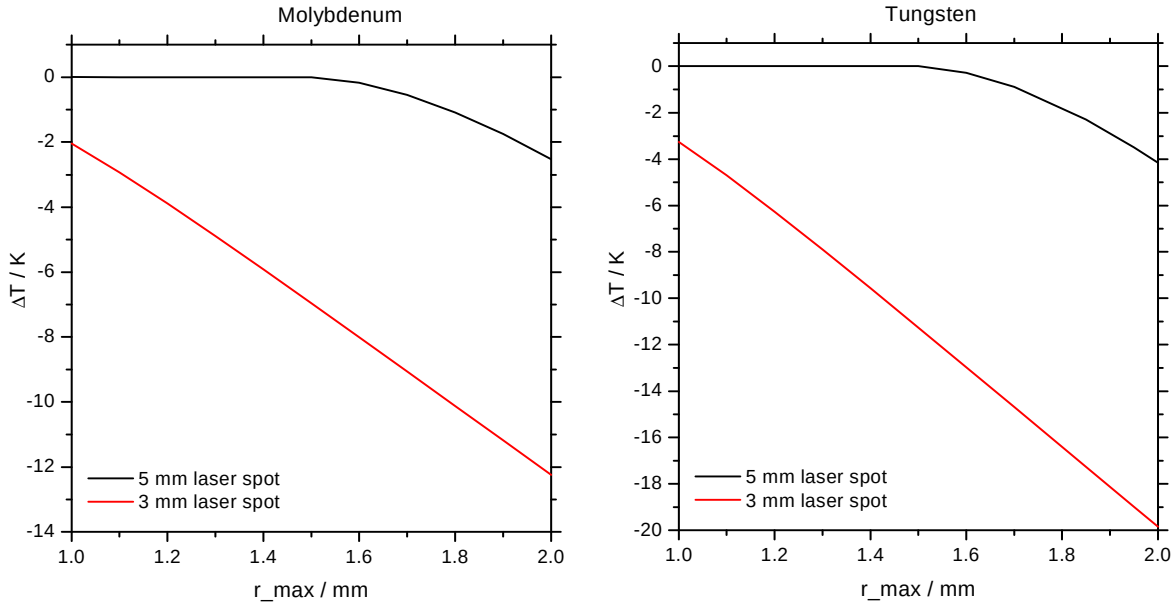


Figure 13: Computed temperature measurement error due to the measured SSE at the freezing point of (a) molybdenum and (b) tungsten for two different laser spot sizes. ΔT was computed based on the assumption that 100% of the radiance that reaches the pyrometer detector originates from an area of XX mm in diameter on the sample.

This work on the SSE has not yet been finalized. The niobium experiments also have to be modeled and the reason for the remaining disagreement between the simulations and the measurements has to be found. The preliminary conclusion is that the SSE can definitely affect the temperature measurement along the freezing plateau when the experimental parameters are not chosen correctly. The size of the molten area on a sample and good alignment of the pyrometers on it is paramount in minimizing this effect and warranting good accuracy.

2 Emissivity measurements

A pyrometer calibrated in terms of blackbody radiance can only provide a direct measurement of radiance temperature T_λ at its operating wavelength. Knowledge of the spectral emissivity of the target at the same wavelength is necessary to convert this to true

temperature, according to Eq. (8). This property is measured in the current research with a multi-channel pyrometer[4]. This consists of a 256-element linear array of Si photodiodes recording the signal at different wavelengths from 488 to 1011 nm. Once the photodiode at 649 nm is calibrated with a reference lamp in the same way as a single-wavelength pyrometer (Fig. 14a), different measurements are repeated with a high temperature blackbody (up to 3500 K) in order to determine the transfer function $K(\lambda)$ for the entire spectral range as[9]:

$$K_4(\lambda) = \frac{\tau_w(\lambda)}{C_{\text{det}}(\lambda, T_{bb})} \frac{1}{\lambda^5 \left[\exp\left(\frac{C_2}{\lambda T_{bb}} \right) - 1 \right]} \tag{14}$$

In the above equation, $\tau_w(\lambda)$ is the window effective transmittance at the wavelength λ, $C_{\text{det}}(\lambda, T_{\text{bb}})$ is the measured intensity (in analog-to-digital converter counts), and T_{bb} the blackbody temperature measured by the already calibrated pixel at 649 nm. At each of these temperatures a spectrum spanning the 256 photodiodes is recorded with an integration time of 4 ms. Whenever a different integrating time τ_i is used, the experimental intensity should be multiplied by a factor $4/\tau_i$ in order to convert it into radiance using the same calibration.

The transfer function $K_4(\lambda)$, 4 indicating the 4 ms of the integration time, independent of the sample temperature (Fig. 14b), transforms the voltage signal output by the photodiodes into a quantity that is directly proportional to the thermally emitted spectral radiance:

$$E_{\text{det}}(\lambda, T) = K_4(\lambda) \cdot C_{Det}(\lambda, T) \tag{15}$$

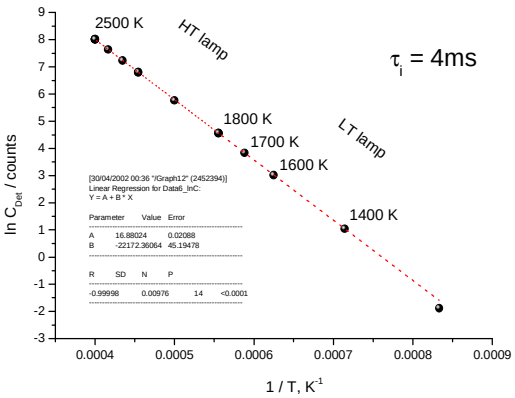


Figure 14a: Calibration of the photodiode at 649 nm against standard W-ribbon lamps.

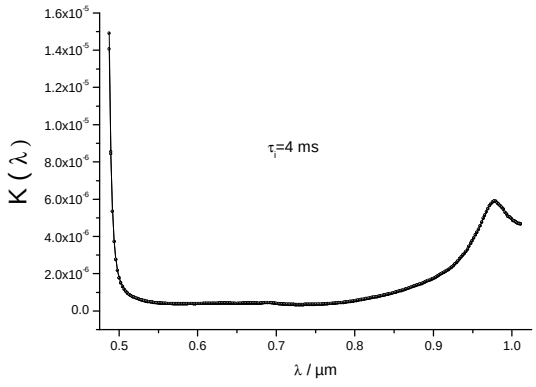


Figure 14b: The transfer function of the opto-electronic system represented by the 256-channel pyrometer.

Thus during the experiments, the radiance spectrum emitted by the sample is measured at different temperatures by multiplying the multi-channel pyrometer rough voltage spectrum by the transfer function $K(\lambda)$. The thus obtained radiance spectrum corresponds to the sample blackbody emission (which only depends on temperature and wavelength and follows Planck's radiation law) multiplied by the sample spectral emissivity, as in Eq. (16).

Three slightly different approaches can be used to obtain the sample emissivity from the measured radiance spectra. These approaches have been tested on zirconium carbide, commonly employed as a high-temperature reference material. This compound is known to be very stable (low vaporization rate, high mechanical stability) at high temperature. Moreover, the ZrC-C eutectic temperature has recently been established to be 3155 K with great accuracy[15,16]. A more detailed laser heating study of the Zr-C system is reported elsewhere[17]. Results are only mentioned here as valuable tests of the current experimental method.

1) The determination of the emissivity was possible by non-linearly fitting the obtained thermal emission spectra with the equation:

$$E_{\mathrm{det}}(\lambda) = \frac{L_{\lambda}(T)}{c_{1L}} = \frac{1}{\lambda^5} \cdot \frac{\varepsilon(\lambda, T)}{\exp\left(\frac{c_2}{\lambda T}\right) - 1} \tag{16}$$

the normal spectral emissivity $\varepsilon(\lambda,T)$ and the temperature T being the free parameters. The emissivity is approximated by polynomials of the form:

$$\varepsilon(\lambda) \cong \sum_{i=0}^{n} a_i \lambda^i \tag{17}$$

ε = constant, i.e. $n = 0$, would correspond to the greybody approximation. The summation is generally extended to $n = 2$, but results are often already acceptable in the greybody approximation. Equation (17) represents the most general expression for the emissivity as a function of wavelength and its terms do not have any particular physical meaning. More meaningful functions can be used in some cases, if the electro-optical behavior of the sample is somehow known in the investigated spectral range. An example application of this method to freezing ZrC_{1+x} at the eutectic temperature is reported in Figure 15.

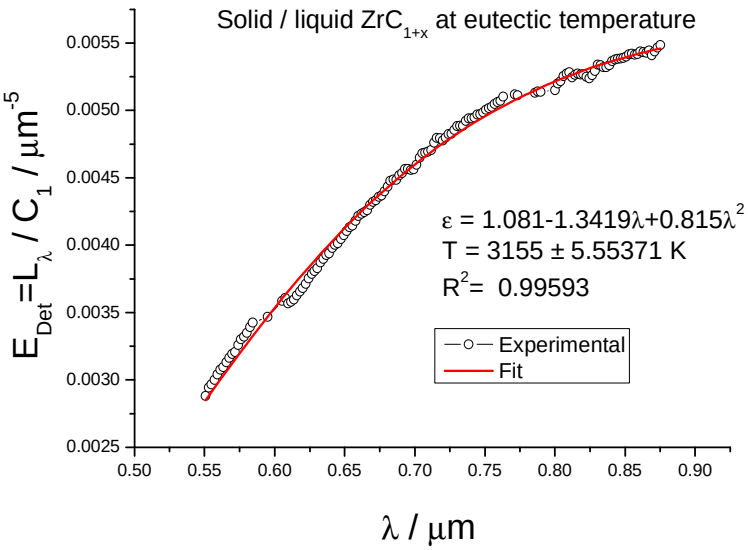


Figure 15: Thermal emission spectrum of ZrC_{1+x} at the eutectic point fitted with a function of the type reported in Eq. (16).

2) As an alternative, the measured radiance intensities can straightforwardly be converted into the inverse of the radiance temperatures. From Eq. (16) with $\varepsilon(\lambda,T) = 1$, T_λ is obtained as:

$$\frac{1}{T_\lambda} = \frac{\lambda}{c_2} \cdot \ln\left(\frac{1}{\lambda^5 \cdot E_{\text{det}}(\lambda)} + 1\right) \tag{18}$$

This curve can then be plotted as a function of wavelength, as in Figure 16, which shows another test performed on ZrC_{1+x}. In the range of validity of Wien's law, the curves thus obtained are fitted based on a slightly re-arranged Eq. (8):

$$\frac{1}{T_\lambda} = \frac{1}{T} - \frac{\lambda}{c_2} \ln \varepsilon(\lambda) \tag{8'}$$

Once more, $\varepsilon(\lambda)$ can be expressed as a Taylor expansion like in Eq. (17), or by using another more specific function. If ε is independent of wavelength or at least constant at the wavelengths at which T_λ is measured, then plotting $1/T_\lambda$ as a function of λ results in a straight line that, when extrapolated to zero wavelength, intersects the inverse-temperature axis at the inverse real temperature $1/T$, as one can easily see from Eq. (8').

This method has been called "extrapolation to zero wavelength"[14]. Even though it may be regarded as mathematically equivalent to the previous approach, this technique allows displaying more accurately the real wavelength dependence of the measured radiance intensity. It therefore permits having a more precise idea of how good the physical

assumptions on emissivity are, e.g. the greybody behavior, and the presence of possible artifacts in the experimental spectra. For example, it can be deduced from Eq. (8') that a negative slope of the curve $1/T_\lambda(\lambda)$ would be physically meaningless, as it would imply an emissivity larger than 1.

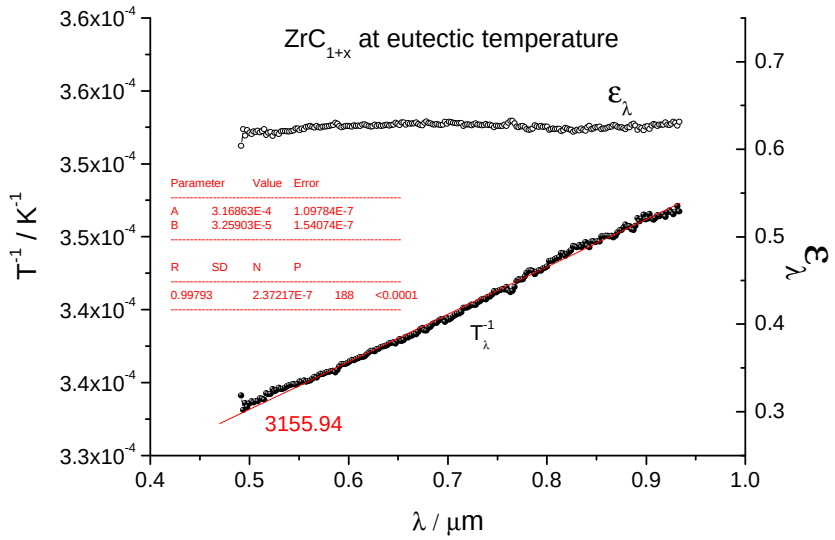


Figure 16: The "extrapolation to zero wavelength" method applied to ZrC_{1+x} at the eutectic point. The deviation from a constant of emissivity values (empty circles) gives an idea of the validity of the "greybody" assumption in this case.

3) In the absence of any direct information on the actual emissivity wavelength dependence of the sample of interest or the class of materials to which it belongs, it is impossible to estimate the uncertainty of the results obtained by the two previous approaches[18,19]. Including too many terms in the summation of Eq. (17) will generally decrease the sum of squares in the least-squares fitting, but even if this sum is equal to zero the calculated emissivity may deviate from the real one[1], whereas numerical instability may arise leading to very high deviations. Therefore, whenever sound enough temperature references exist for the material system under investigation, the experimentally obtained radiance spectra can preferably be used as direct emissivity measurements of solid and liquid samples at a known temperature. As mentioned, this is a possible option, for example, at the eutectic temperature of ZrC_{1+x}, which has been determined at (3155 ± 1) K with great accuracy. This was imposed to be the temperature of the two thermal arrests (melting and freezing) of Figure 17.

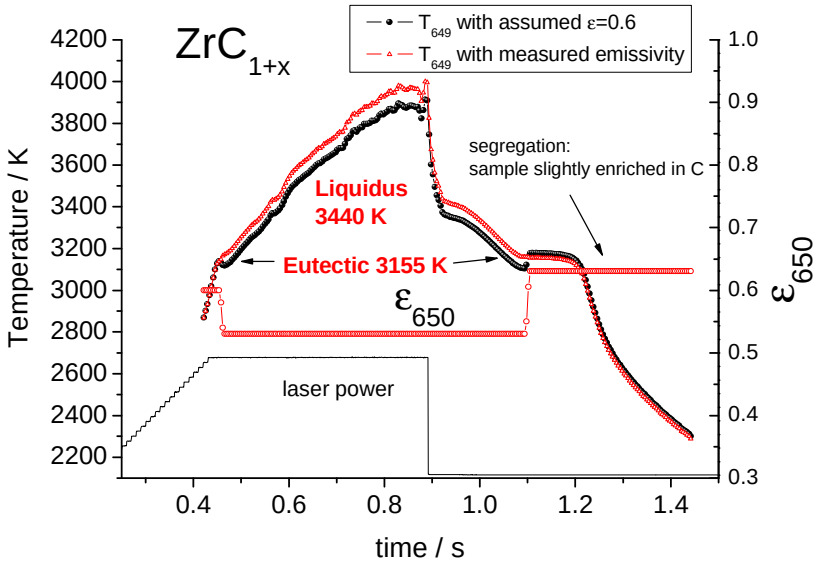


Figure 17: Thermogram of a ZrC_{1+x} sample measured at 650 nm. The thermal arrests corresponding to the eutectic have been fixed at 3155 K. Emissivity of solid and liquid ZrC_{1+x} could then be deduced accordingly. Black curve: thermogram corresponding to an assumed constant emissivity ε(650)=0.6. Red curve: thermogram corresponding to the real emissivity values.

One can observe that for a fixed constant emissivity 0.6 on melting, the thermal arrest is followed by an apparent temperature decrease, while on freezing the opposite effect is observed (black thermogram-corresponding to constant emissivity). This phenomenon can be explained on the basis of an emissivity decrease upon formation of liquid[(2)]. By fixing the melting/freezing temperature at 3155 K, this emissivity effect can be evidenced. Thermal radiation spectra were recorded at several points during the melting and freezing arrests. Calling $S_i(\lambda)$ each of these spectra, and $P(3155)$ the Planck (ideal blackbody) radiance function at 3155 K, the sample normal spectral emissivity for each experimental spectrum is by definition

$$\varepsilon_i(\lambda) = \frac{S_i(\lambda,3155)}{P(\lambda,3155)} \qquad (19)$$

Emissivity values are thus obtained in the investigated wavelength range of 0.55 to 0.9 µm for each of the experimental spectra recorded during the melting and freezing arrests. Twelve spectra were recorded on melting and twelve on freezing. The spectra taken on the maximum recalescence in both cases were considered as corresponding to the solid, whereas

(2) Since the same effect occurs both on melting and freezing, it cannot be related to supercooling of the liquid. Supercooling of the liquid can be avoided by suitably setting the laser heating parameters.

those taken at the minimum temperature during the phase transition were attributed to the liquid. Spectra in-between were considered as a mixture of the two. Results of emissivity as a function of wavelength for solid and liquid ZrC under these assumptions are shown in Figure 18. Uncertainty bands are given by the composition (according to the uncorrelated error propagation law) of the uncertainty on the eutectic temperature of ZrC_{1+x} and the dispersion on the current experimental emissivity data.

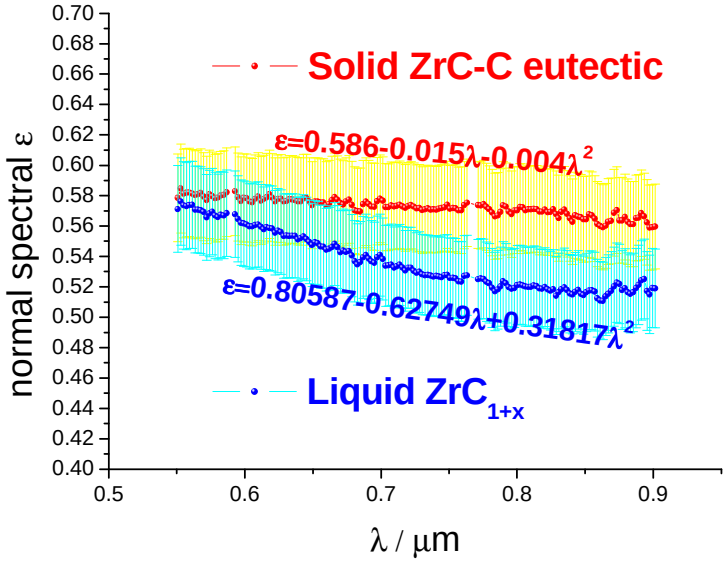


Figure 18: Emissivity as function of wavelength in liquid and solid ZrC_{1+x} at the eutectic temperature.

Emissivity values for a certain material system obtained with the current approach can be used to fit Planck's curves recorded on samples having different compositions in the same system. The spectra will then be fitted with temperature as the only unknown parameter. This latter test permits to check the validity of the measured $\varepsilon(\lambda)$.

3 Ultra - Violet Pyrometry

In addition to the depicted pyrometry techniques, the sample radiance temperature could be measured in some cases in the ultraviolet range at 0.215 μm.

These measurements were performed within an exploratory research project and should therefore be considered as preliminary only. Nonetheless, the results they yielded were useful for uranium carbides, where they helped resolve some doubts about the spectral emissivity correction needed in order to obtain the real temperature of the investigated material. In fact, the main advantage of UV pyrometry is the short wavelength at which

radiance is measured, resulting in a small difference between the measured radiance temperature and true temperature. This can be easily seen from Eq. (8):

$$\lim_{\lambda\to 0} \Delta\left(\frac{1}{T}-\frac{1}{T_\lambda}\right)=0 \Rightarrow \lim_{\lambda\to 0} T_\lambda = T \;\text{ if }\; \lim_{\lambda\to 0}\varepsilon_\lambda \neq 0 \qquad (8'')$$

which, of course, is also the basis of the previously described "extrapolation to zero wavelength" technique. Figure 19 depicts the linear dependence of $\Delta(1/T)$ on wavelength.

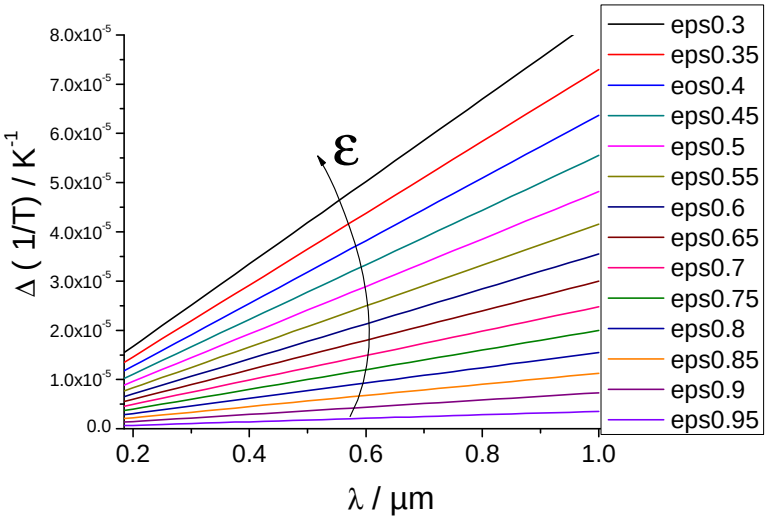


Figure 19: $\Delta\left(\frac{1}{T}\right)$ **as a function of wavelength.**

Rearranging terms in Eq. (8) leads to:

$$\Delta T \equiv T - T_\lambda = -T_\lambda \cdot T \cdot \Delta\left(\frac{1}{T}\right) \approx -T^2 \frac{\lambda}{c_2}\ln\varepsilon_\lambda \qquad (20)$$

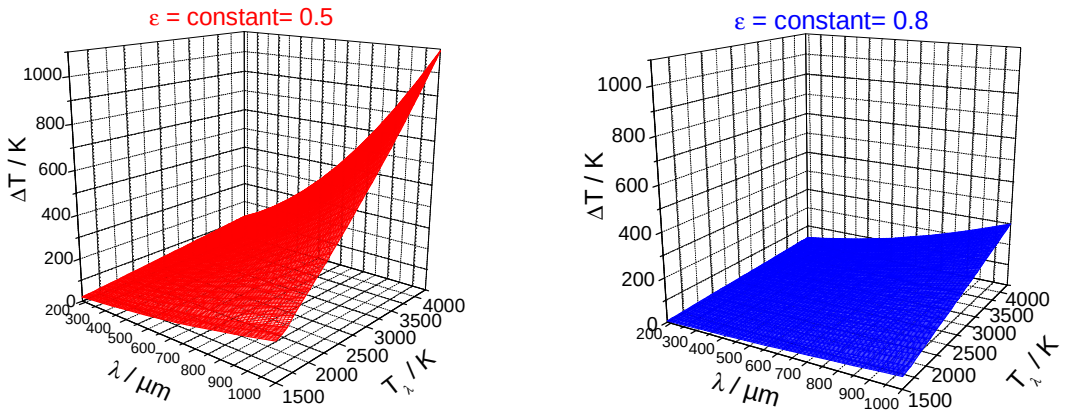
which also demonstrates the well-known strong increase of the temperature error (keeping in mind that $\ln\varepsilon_\lambda$ is negative) in the absence of an emissivity correction at high temperatures.

Expressing this temperature error in terms of measured radiance temperature yields:

$$\Delta T = -\frac{\lambda \cdot T_\lambda^2 \ln\varepsilon_\lambda}{C_2 + \lambda \cdot T_\lambda \cdot \ln\varepsilon_\lambda} \qquad (21)$$

Eq. (21) is plotted in Fig. 20 for two different values of emissivity, making again clear the advantage of short wavelength measurements, particularly at high temperatures.

In addition to the lower difference between radiance and true temperature at short wavelengths, measuring radiance in the visible and UV ranges at the same time permits to apply the methods of multichannel pyrometry described in this chapter to a broader spectral domain.



(a) **(b)**

Figure 20: ΔT as a function of wavelength and radiance temperature T_λ for a constant emissivity of (a) 0.5 and (b) 0.8.

In this context, a UV pyrometer is currently being developed within a co-operation between the CNRS–CRMHT Orléans and the JRC–ITU Karlsruhe. Preliminary, but already useful, results have been obtained with the setup illustrated in figure 21.

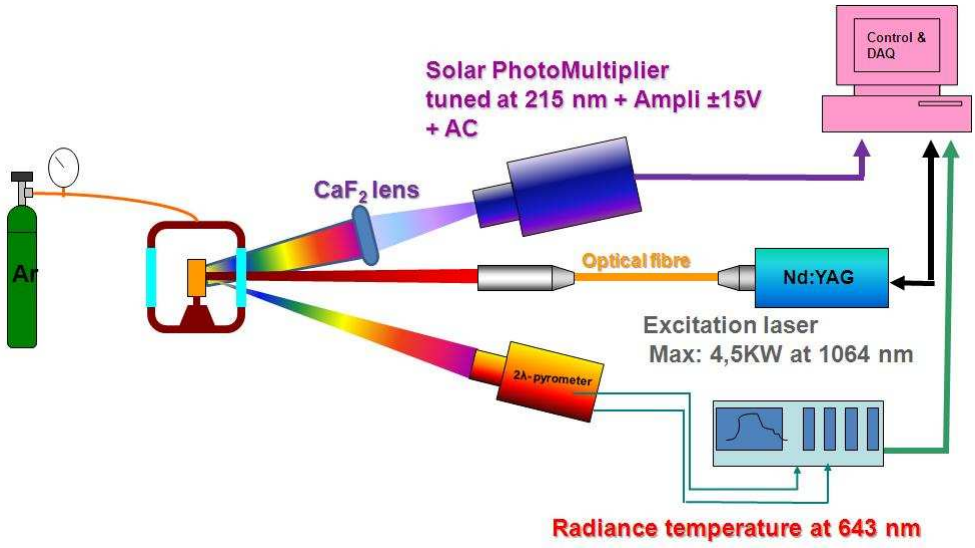


Figure 21: The experimental setup under development for UV–pyrometry measurements.

While the sample was heated under the same conditions described previously, an additional UV pyrometer was mounted in parallel to the usual pyrometers. This latter

consisted, in the current first approach, of a CaF_2 lens and a photomultiplier (PM) connected to a ±15 V amplifier and AC converter. The employed PM tube was a Hamamatsu® R6834 for UV radiation detection with a Cs-Te 28 mm-diameter photocathode of the head-on type with solar-blind response (160 nm to 320 nm), and an 11-stage photomultiplier. An interference filter centered at 215 nm was mounted in front of it for wavelength selection. The Signal/Noise ratio of the amplifier was adequate to amplify the small intensity variations which can be deduced from Planck's curves in the temperature range of interest for the current work at 215 nm (Fig. 22). However, because of the much lower thermal radiance available at this wavelength, the lowest detectable temperature was at about 2200 K.

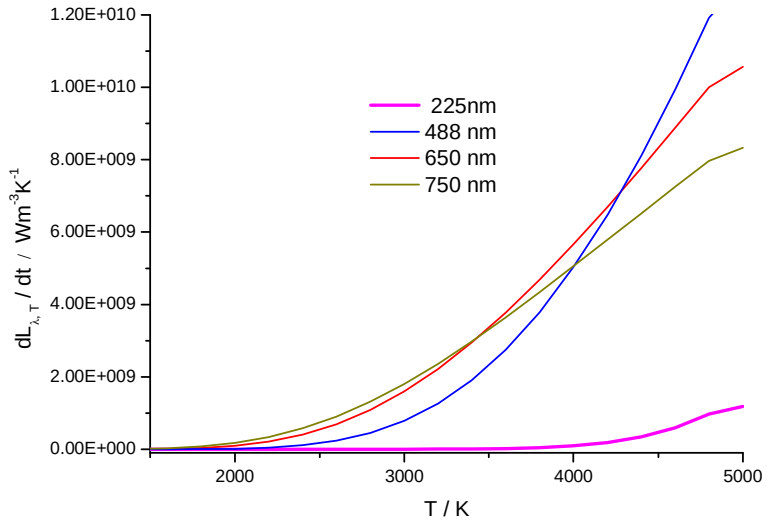


Figure 22: Sensitivity of the radiation intensity to temperature at different wavelengths as a function temperature T for an ideal blackbody.

The calibration of the temperature curve was performed taking as a reference the melting/freezing point of scandium sesquioxide Sc_2O_3 (figure 5). This transition point is reported to be (2757 ± 20) K (Reference 21 converted to the current temperature scale ITS-90), with a spectral emissivity $\varepsilon(\lambda)$ of approximately 0.9. These conditions are therefore ideal for calibrating the current apparatus, as it can be calculated through Eq. (21) that the emissivity effect on the radiance melting temperature of Sc_2O_3 is approximately 13 K, i.e. much less than the datum uncertainty itself. In other words, this calibration reference is, under the current experimental conditions, equivalent to an ideal blackbody reference within the experimental uncertainty.

The calibration was performed without protective sapphire window between the sample and the UV pyrometry apparatus, the Sc_2O_3sample was therefore heated in air.

The PM-measured intensity I_{PM} (215 nm) is thus related to the blackbody radiance through Planck's equation as

$$I_{PM}\,(215\text{ nm}) = P\,(215\text{ nm}, 2757\text{ K}) \cdot A \tag{22}$$

P(215 nm, 2757 K) is Planck's function evaluated at the Sc_2O_3 melting point and 215 nm, and A is a calibration factor accounting for the CaF_2 lens transmittance, the transfer functions of the detection electronics and the emissivity of the reference sample (here assumed to be equal to 1 within the reference temperature uncertainty).

Once A is determined, radiance temperature is obtained from the intensity measured by the UV-pyrometry apparatus as

$$T_{215} = \frac{1}{\frac{\lambda}{c_2}\ln\left(\frac{c_{1L}}{\lambda^5}\cdot\frac{A}{I_{PM}}\right)} \tag{22}$$

In Eq. (22), which is valid within Wien's approximation, c_{1L} and c_2 are the two radiation constants, and $\lambda = 0.215\ \mu m$.

A first application of this calibration was the direct measurement of the sapphire window transmittance at 215 nm. This was obtained by measuring the apparent melting temperature of Sc_2O_3 with and without sapphire window. The window transmittance was measured as the ratio between the experimental intensities detected at the freezing point in the two cases, and resulted to be

$$\tau\,(\text{sapphire}, 215\text{ nm}) = 0.551 \tag{23}$$

This value was then used in all the successive measurement that were performed under controlled atmosphere and, therefore, in the presence of the sapphire window.

Another test of the UV pyrometry setup was performed on the eutectic temperature of the system ZrC-C. Although this material, due to its lower emissivity (around 0.6 in the visible), is less suitable for the calibration of a UV temperature detector, its melting-freezing temperature established with great accuracy (3155 ±1 K) constitutes a good reference. The radiance temperature of this eutectic at 215 nm was measured to be (3072 ± 8) K (Figure 24), corresponding to a spectral emissivity of 0.56 ± 0.03. This latter result shows that solid ZrC_{1+x} approximately behaves as a greybody in the UV – VIS spectral domain.

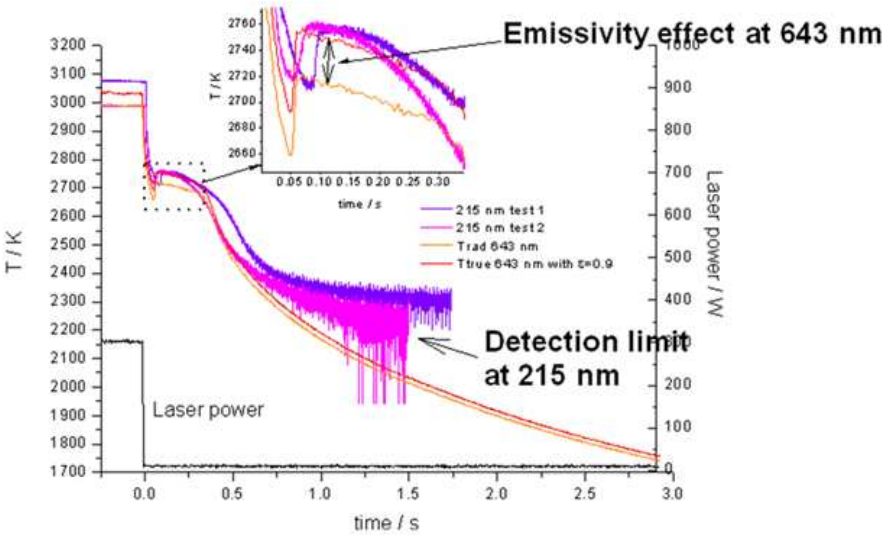


Figure 23: Solidification temperature measurements performed on Sc_2O_3 to calibrate the current UV–pyrometer. UV radiance temperature curves are compared with radiance and true temperature (calculated with ε = 0.9) plots at 643 nm. Solidifying Sc_2O_3 behaves, within the experimental uncertainty, as a blackbody source at 215 nm.

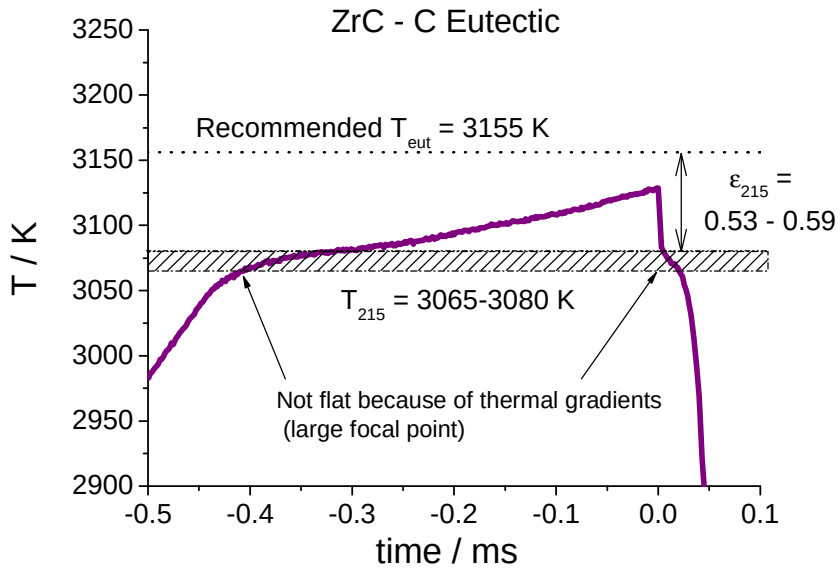


Figure 24: Melting / solidification temperature measurements performed on eutectic ZrC_{1+x} with the current UV – pyrometer.

4 Reflected Light Signal

A second laser is used, focused on the same position as the heating laser, in such a way that the laser beam is reflected from the sample surface directly into a fast pyrometer photodiode tuned exactly at the same wavelength. A cw Ar^+ laser of 0.75 W at 488 nm ("blue

laser") is used as probe laser in the present research. The thus obtained Reflected Light Signal (RLS), recorded in parallel with the radiance during the laser heating, is a very sensitive method to determine the onset of the melting/freezing transitions. Abrupt changes in the sample's reflectivity may indicate phase transitions. In particular, a characteristic noise-like structure appears in the RLS upon melting, due to vibrations of the sample's liquid surface, which disappear again upon freezing (Fig. 25).

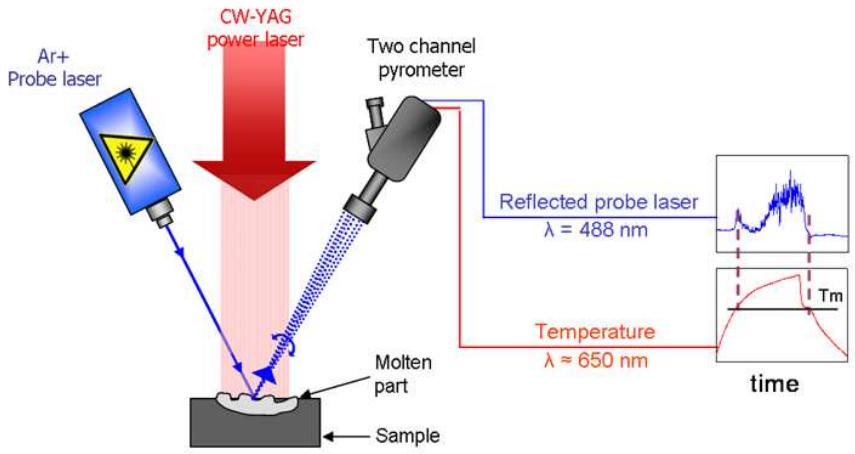


Figure 25: Schematic of the Reflected-Light-Signal technique for the detection of the melting and freezing transitions.

5 Sample Characterization

A systematic control of the composition, purity or even homogeneity of the samples is necessary in parallel to the high temperature behaviour investigation. The quality of both "fresh" (before laser irradiation) and laser heated samples has to be controlled, to check about possible degradation occurring during the laser treatments. These characterizations, for carbides and oxides, involve a number of analyses and also imply extra difficulties because of the radio-activity of the investigated materials. For example, in order to analyze the same sample before and after heat treatment, one has to move it several times between different α-shielding gloveboxes. The weight of each actinide-containing sample has to be well known prior to transfer (the uranium and plutonium weights have to be respectively known with a precision of 1 and 0.001 g) which impose an intermediate passage in an intermediate glovebox for weighing. Any sample handling inside a glove box is obviously much more awkward and slower. Finally, all these experimental constraints and the limited amount of

available samples limit the number of possible analyses. It was consequently possible to characterize only a few representative samples per series of compositions.

The following paragraphs give a general description of the equipment employed for the different materials characterizations performed before and after laser irradiation. More details about the composition characterization and the specific precautions taken for carbides and oxides are more thoroughly reported in chapters 3 and 4. All equipment presented, except the scanning electron microscope used for the uranium carbides, are installed inside a glovebox.

5.1 X-Ray Diffraction

Two different devices are used for X-Ray Diffraction (XRD). The analyses performed on uranium carbides were done with a Siemens ® D8 advanced diffractometer (Bragg-Bentano configuration) equipped with a Ge(111) incident beam monochromator and a Vantec position sensitive detector, covering 6° in 2θ. For the structure refinement and the quantitative phase analysis by the Rietveld method, the XRD patterns were typically collected in the 2 θ range 10-110° (step of 0.0085°), with an exposure time of 5 s per step. Samples were rotated during the data collection in order to improve the sample statistic and reduce the effects of possible preferential orientation. The analysis of the plutonium carbide and oxide samples were performed using a Bruker® D8 Advanced diffractometer (Cu-Kα_1 radiation) with a 2θ range of 10°-120° using 0.009° steps with 2 s of count time per step at operating conditions of 40 kV – 40 mA. The XRD instrument was equipped with a Lynxeye® 3° linear position sensitive detector. In both cases, the fitting and refinement were performed using the Fullprof® software.

5.2 Scanning Electron Microscope and Electron Microprobe

Secondary electron (SE) and backscattered electron (BSE) images were recorded on two different Scanning Electron Microscopes (SEM). They permit to study the morphology and control the homogeneity and purity of the fresh and laser-irradiated samples. In particular, after laser heating, pictures of the molten area can provide interesting indication on the freezing mechanisms. In some cases, semi-quantitative and quantitative information on the

elemental composition were also acquired from Energy Dispersion X-ray (EDX) and Electron-Probe Micro Analysis (EPMA).

The uranium carbides were analyzed with a Tescan Vega SEM, Model TS5130 LS, operated with a 30 kV electron beam accelerating potential and 50 µA beam current under an ultra-high vacuum of 10^{-8} mbar. For the samples containing plutonium, images were recorded on a Philips® XL40 scanning electron microscope installed in a glove box operated at 20 kV. Quantitative analysis and X-ray element maps were acquired using a shielded Cameca® SX100R electron microprobe operated at 20 kV and 20 nA. Whereas no particular preparation of the specimens was needed for SEM analysis, in the case of EPMA samples were embedded in epoxy resin, cut to get a cross section showing the thickness of the molten area, and finely polished. Backscattered electron (BSE) and absorbed current (Abs) images were acquired, and the beam current was adjusted in order to get the best possible contrast in the images.

5.3 Fusion extraction - infrared determination

This method is used to measure the carbon and oxygen content. It is based on the combustion of a sample at high temperature that permits to form gaseous carbon dioxide (CO_2) from either the carbon or the oxygen contained in the specimen, depending on the atmosphere and the crucible material in which the measurement is carried out (Fig. 26). The measurement is then based on the measured IR of the produced CO_2 at a characteristic wavelength (2640 cm^{-1} or 3.79 µm).

In order to measure the carbon content, the sample is placed in an Al_2O_3 crucible inside an electrical induction furnace and heated up to 3500 K under a flow of oxygen (99.99% pure). It is assumed that all and only the carbon from the sample reacts with oxygen to produce CO and CO_2. These gases pass through a system of filters and catalysts to obtain only CO_2 which is measured by IR-absorption spectroscopy. From the quantity of CO_2 analyzed, one can easily obtain the carbon content of the sample.

In the same way, using a graphite crucible inside a resistance furnace and a helium flow, it is possible to measure the oxygen contained in the sample. In this case, it is assumed that all the oxygen contained in the sample reacts with the crucible during heating and forms CO and CO_2. The amount of CO_2 is quantitatively determined by IR spectroscopy after the

cleaning step and, in this case, all the measured CO_2 corresponds to the oxygen content in the sample.

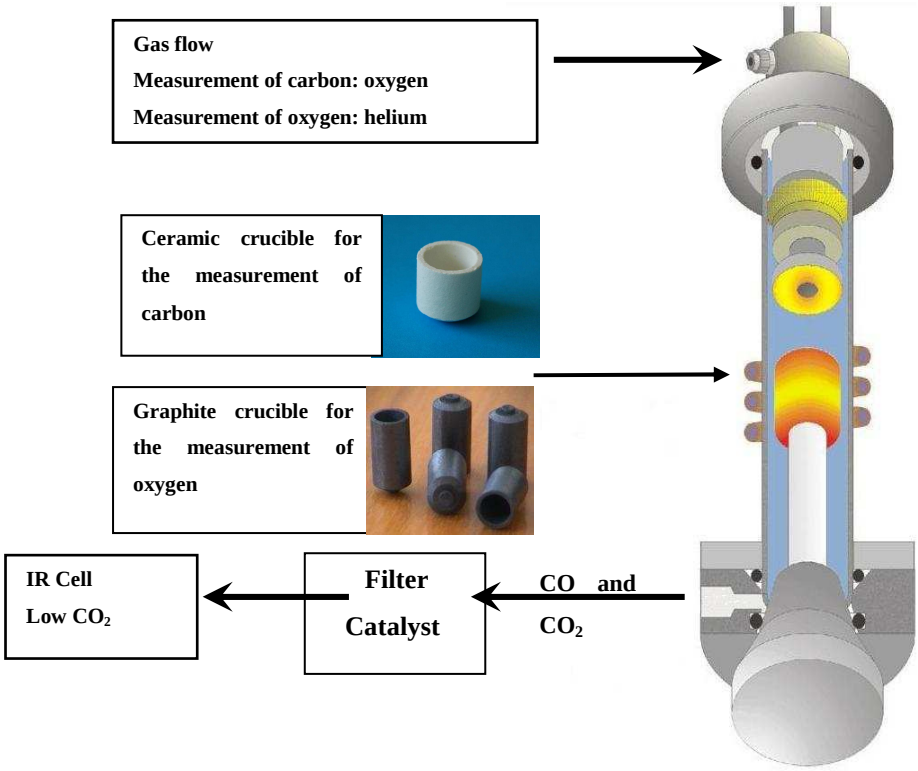


Figure 26: Fusion extraction - infrared determination apparatus

6 References – Chapter 2

1. A. Cezairliyan, and V. E. Peletsky, eds., Plenum, New York, 1 (1984) 643.
2. F. Righini and T. Matsumoto, Int. J. Thermophys. 26 (2005) 941.
3. M. Boivineau and G. Pottlacher, Int. J. Mater. Prod. Technol. 26 (2006) 217.
4. D. Manara, M. Sheindlin, W. Heinz, and C. Ronchi, Rev. Sci. Instrum. 79 (2008) 113 901.
5. M. A. Sheindlin, Sov. Rev. B. Therm. Phys. 4 (1992) 1.
6. F. E. Nicodemus, ed., *"Self-study manual on optical radiation measurements"*, NBS Technical Note 910-1, Chapters 1-3 (1976).
7. H. Preston-Thomas, Metrologia 27, 3 and 27, (1990) 107.
8. D. P. DeWitt and J. C. Richmond, *"Thermal radiative properties of materials"*, in Theory and practice of radiation thermometry, D. P. DeWitt and G. D. Nutter, eds.,Wiley, New York (1988).
9. D. Manara, "Melting transition measurements in uranium dioxide", PhD Thesis, Technical Note JRC-ITU-TN-2004/05 (2004).
10. R. E. Bedford, G. Bonnier, H. Maas, and F. Pavese, Metrologia 33 (1996) 133.
11. T. Ricolfi and L. Wang, *"Experiments and remarks on the size-of-source effect in precision radiation thermometry"*, in Proceedings of TEMPMEKO 1993, Fifth International Symposium on Temperature and Thermal Measurements in Industry and Science, Prague, (1993) 161.
12. P. Bloembergen, Y. Duan, R. Bosma, Z. Yuan, *"The characterization of radiation thermometers subject to the size-of-source effect"*, in Proceedings of TEMPMEKO 1996, Sixth International Symposium on Temperature and Thermal Measurements in Industry and Science, Torino, (1997) 261.
13. G. Machin and M. Ibrahim, "Size of source effect and temperature uncertainty: I – High temperature systems", in Proceedings of TEMPMEKO 1999, Seventh International Symposium on Temperature and Thermal Measurements in Industry and Science, Delft, (1999) 681.
14. A. S. Tenney, "Radiation ratio thermometry", in Theory and practice of radiation thermometry, D. P. DeWitt and G. D. Nutter, eds.,Wiley, New York (1988).
15. E. R. Woolliams, G. Machin, D. H. Lowe, and R. Winkler, Metrologia 43, R11, (2006).

16. J. Hartmann, Phys. Rep. 469 (2009) 205.
17. H. F. Jackson, D. D. Jayaseelan, W. E. Lee, M. J. Reece, F. Inam, D. Manara, C. Perinetti-Casoni, F. de Bruycker, and K. Boboridis, Int. J. Ceram. Technol. 7 (2010) 316.
18. P. B. Coates, Metrologia 17 (1981) 103.
19. P. B. Coates, High Temp. – High Pressures 20 (1988) 433.
20. Control in Science and Industry, Vol. 6, pp. 787-789, J. F. Schooley, ed., AIP, New York (1992).
21. J. Hlavac, Pure and Appl. Chem., vol. 54, 3 (1982) 681.

Chapter 3: Experimental Study of the Melting Behaviour of Oxide Nuclear Fuels

1 Introduction

As already described in Chapter 1, mixed oxide fuel (MOX) is employed for the generation of nuclear energy for civil purposes with PuO_2 concentrations in UO_2 typically varying between 0 and 30 mol %. Thus, many physico-chemical properties of low Pu-content (U,Pu) mixed oxides (MOX) have been thoroughly investigated since the 1950s. The difficulties inherent to the study of these compounds considerably increase with Pu content and temperature, essentially due to the high oxygen potential and the reactivity of plutonium dioxide. Figure 1[1] shows the different oxygen potentials of actinide oxides, and in particular that stoichiometric $PuO_{2.00}$ has a higher oxygen potential than stoichiometric $UO_{2.00}$. Moreover, UO_2, unlike PuO_2 (under the current conditions), can be further oxidized to form hypostoichiometric UO_{2+x}. Therefore, even a well conceived heat treatment, ensuring an overall fuel with an oxygen to metal ratio O/M=2 (which can be checked by thermogravimetry or other methods), does not guarantee a homogeneous oxygen distribution in the material in the presence of gradients (compositional, thermal, of density etc.). This uneven oxygen distribution is well known to occur in the oxide fuel, particularly under in-pile operational conditions[2].

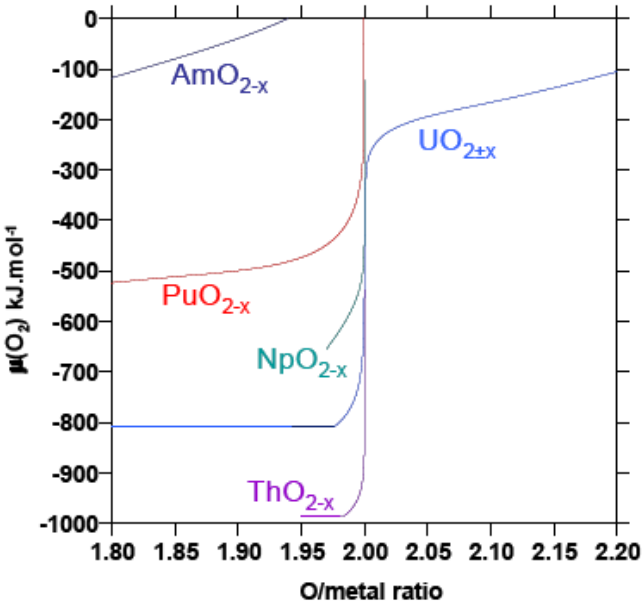


Figure 1: Oxygen potential of different actinide oxides[1]

As for the current research, it has been one of its primary goals to determine the melting behavior of the UO_2 –PuO_2 pseudo-binary system ensuring as much as possible that no segregation or second phase were formed during the heating cycles. These conditions can hardly be produced with any practical experimental approach. Nonetheless, the short duration of the experiments and the containerless conditions obtained with the current laser heating technique can be effective in reducing as much as possible the mentioned out-of-equilibrium phenomena. The main purpose of such an approach is to provide reference experimental data as close as possible to those corresponding to the ideal thermodynamic equilibrium conditions. In doing so, one should bear in mind that such conditions can never be actually realized, particularly in a complex system like the present. For this reason, obtaining general trends and correlations while keeping under control as many uncertainty sources as possible can already be considered as a major achievement.

The study of the pure compounds, PuO_2 and UO_2, the end members of the pseudo-binary system, has constituted a first step of this investigation. While the melting behavior of stoichiometric UO_2 was fairly well established before the beginning of this work, the solid-liquid transition of stoichiometric and sub-stoichiometric PuO_2 is still a controversial subject. For this reason, the first has been checked here mostly in order to validate the good functioning of the current approach, whereas the second has been studied thoroughly. Subsequently, a number of mixed UO_2 – PuO_2 compositions have been investigated, in order to determine a general trend for the solidus and liquidus lines of this pseudo-binary system. Finally, the present experimental approach has been used for the investigation of the melting point of neptunium dioxide, a compound less well known until now. This last part of the study constitutes a starting point of the investigation of other minor actinide oxides and more complex multi-oxide systems, of great interest for the nuclear fuel of the Fourth Generation.

2 Uranium Dioxide

A first test for the validity of the current experimental method for the investigation of U and Pu oxides consisted in measuring the well established melting temperature of $UO_{2.00}$. The samples used for this test were industrial, nuclear plant grade uranium dioxide pellets

fabricated by Advanced Materials Inc.®. The pellets, cylinders 1.5 cm thick by 8 mm in diameter, were cut into thinner disks 2-3 mm thick, in order to better fit into the sample holder. The disk composition was checked by thermogravimetry (full oxidation to U_3O_8 under air at 1200°C) to be $UO_{2.000\pm0.005}$.

The laser heating experiments provided thermograms showing a clear and pronounced thermal arrest upon freezing (Figure 2). The corresponding congruent melting/freezing temperature, obtained with the literature emissivity value[3] of 0.83 is (3130 ± 20) K. This value agrees perfectly with the most recent literature recommendations[4,5]. Since this test was successful, the present research was continued with the investigation of the melting temperature of (U, Pu) MOX, starting with pure PuO_2.

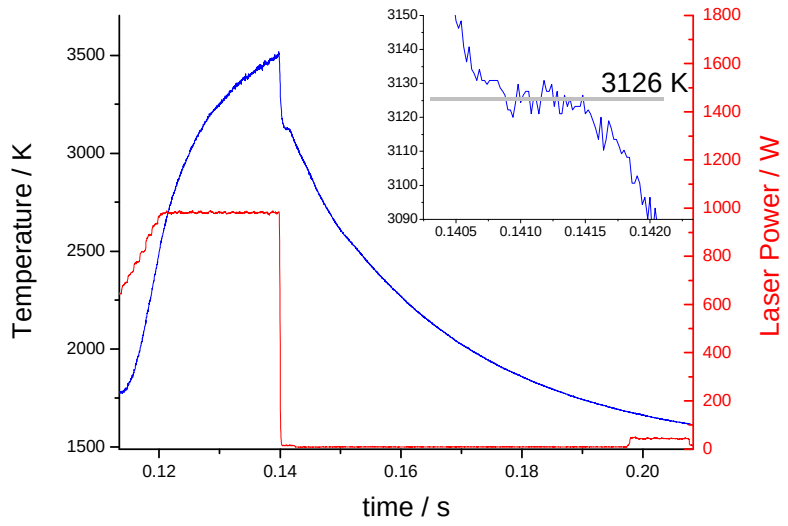


Figure 2: Representative thermograms recorded with the fast pyrometer at 652 nm on $UO_{2.00}$ samples.

3 Plutonium Dioxide

Plutonium dioxide is one of the components of mixed oxide-based nuclear fuels, normally in a mixture with uranium dioxide. Although pure PuO_2 is generally not employed in industrial applications, its melting temperature is an important reference parameter for the comprehension of the UO_2-PuO_2 phase diagram at high temperature. Historically, this point was assessed to be near 2700 K in the beginning of the 1970s, essentially based on the most

recent of a series of measurements performed by Lyon and Baily[6] and by Aitken and Evans[7] using the thermal arrest technique and induction heating of tungsten-encapsulated samples. Riley[8] combined visual detection of melting with a variety of experimental setups, including flame melting under controlled atmosphere. However, these measurements were certainly affected by reaction of the sample with the tungsten crucible in the first case, and by reduction of the investigated specimen reported by Riley himself in the second. This latter issue was also reported in the review by Lemire et al.[9]. Since then, no further experimental research was performed on this subject until the last decade, as summarised in the reviews of Carbajo et al.[10] and of Guéneau et al.[11].

In the period 2007-2009 Kato et al.[5;12-14] published a series of novel experimental studies on the (U, Pu) MOX fuel used for the Monju reactor, in which the commonly accepted PuO_2 melting point was questioned, together with the solidus and liquidus temperatures of other compositions, and a considerably higher one (by about 200 K) was proposed. Kato et al. performed a traditional thermal arrest analysis, but used crucibles of different shapes and materials (tungsten, rhenium) to demonstrate that in Pu-rich MOX and, especially, in pure PuO_2 samples, the interaction between sample and containment affected the apparent solidus and liquidus points well beyond the intrinsic uncertainty limits of the experimental method (Figure 3).

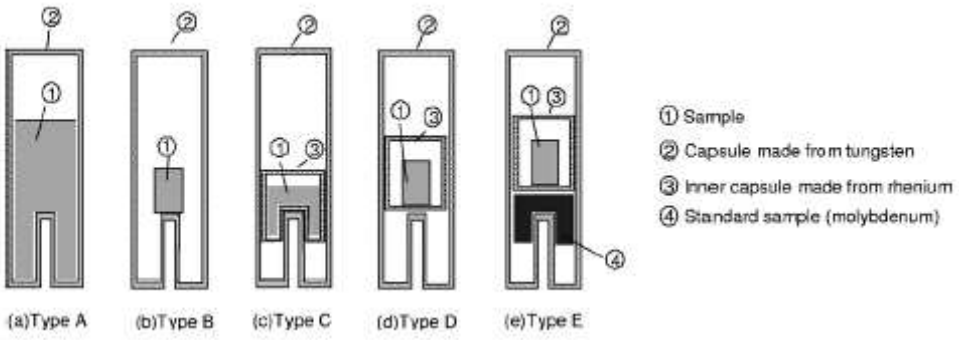


Figure 3: Crucibles used by Kato et al for the melting behaviour investigation in (U, Pu) MOX, and the observed solidus trend as a function of the used crucible in low-Pu samples.

Because of this interaction, even Kato et al. were not able in the end to measure the melting point of pure PuO_2 directly, as instead of the expected congruent melting they observed two distinct transition temperatures differing by about 150 K. They attributed this result to the high reactivity of liquid PuO_2 towards rhenium, just as in the case of tungsten

crucibles and all MOX with a PuO_2-content higher than about 20 mol%. More specifically, they suspected that the high oxygen potential of PuO_2 resulted in the oxidation of Re and the simultaneous reduction of the samples. Nonetheless, it was a big merit of Kato et al. to highlight this source of uncertainty, and also to perform a systematic study of the oxygen potential influence on experimental data. Their work, summarized in the UO_2 – PuO_2 solidus-liquidus curves reported in figure 4, has largely encouraged the current research, whereby the containerless conditions and the very short heat treatments permitted with the laser apparatus represented a strong asset to undertake novel studies on the $(U,Pu)O_2$ phase diagram.

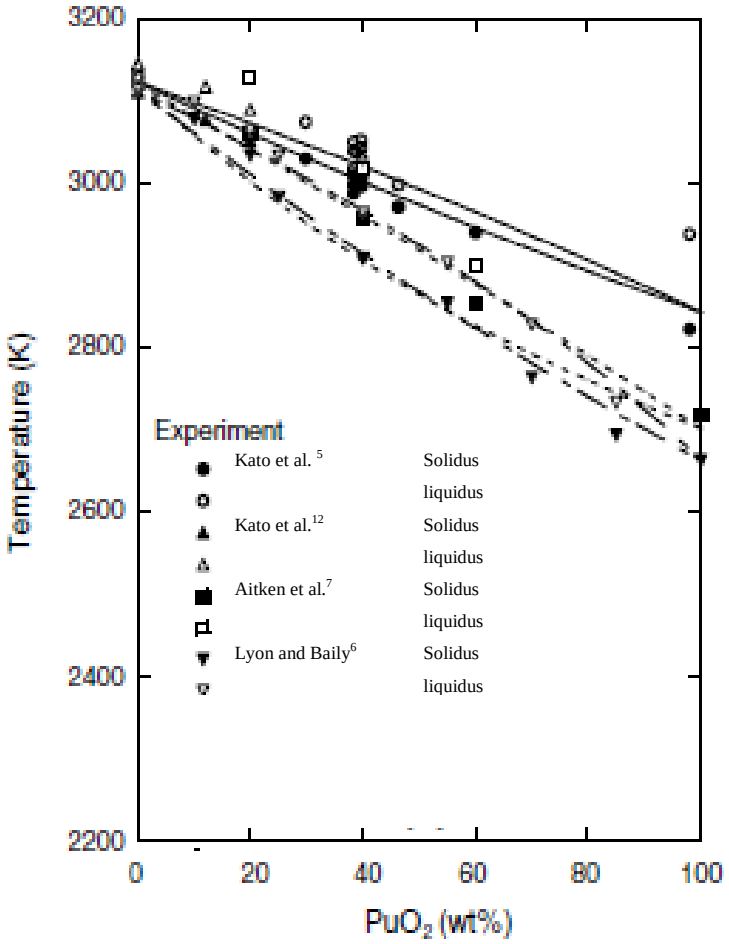


Figure 4: Solidus and liquidus temperature in the UO_2-PuO_2 system.

3.1 Sample preparation

A series of seven samples of plutonium dioxide was prepared for melting temperature investigation (Table 1). The isotopic composition of the plutonium employed was checked by High Resolution Gamma Spectroscopy (HRGS) to be 93.4 wt.% ^{239}Pu and 6.4 wt.% ^{240}Pu.

Traces (<0.2 wt. %) of ^{241}Pu and ^{241}Am stemming from β-decay of ^{241}Pu were detected by Thermal Ionisation Mass Spectrometry (TIMS). The starting material was powder or beads obtained by gel-supported precipitation (SOL-GEL). Disk-shaped samples of 8 to 9 mm in diameter and about 4 mm in thickness were obtained using a bi-directional press. The samples were then sintered in an atmosphere of $Ar + H_2$ with approximately 1500 ppm of H_2O to obtain dense material. In order to obtain the exact O/Pu = 2 stoichiometry, samples C and D were subjected to two consecutive heat treatments under a flow of air at 1423 K for 8 hours. Already after the first heat treatment the measured weight gain of the samples corresponded to stoichiometric PuO_2 separately measured by thermo-gravimetry (TG). TG tests were realised by oxidising PuO_2 samples in an air flux at temperatures up to 1200°C, up to stabilization of the sample weight. Since it was recently proven by Martin et al.[15] that hyper-stoichiometric PuO_{2+x} cannot be formed under such conditions, the weight stabilisation was interpreted as corresponding to the exact O / Pu = 2.00 stoichiometry. This was cross-checked by observing that no further change was noticed after annealing the samples under air for a second time. Similar heat treatments under air were performed on the remaining samples E, F, and G. A lattice parameter of 5.396(1) Å was measured by X-ray diffraction (XRD) on sample G, corresponding to the literature value for PuO_2[16].

Sample	**Name**	**Starting Materials**	**Sintering (gas / temperature (K) / time (h))**	**Annealing gas / temperature (K) / time (h))**
$PuO_{1.83}$	A – B	Powder	Ar +2% H_2 + 1500 ppm H_2O / 1923 / 8	No
$PuO_{2.00}$	C - D	Powder		Air / 1423 / 8 Two times
		Powder		
	E – F - G	Sol gel beads	Ar +2% H_2 + 2000 ppm H_2O / 1923 / 8	Air / 1073 / 24 Two times

Table 1: PuO_2 and PuO_{2-x} samples prepared in this research

Selected samples were examined after the laser experiments by TG and XRD. The microstructure, homogeneity, and purity of specimens taken from both molten and non-molten sample areas were analysed by Electron Probe Micro Analysis (EPMA) and Scanning Electron Microscopy (SEM).

3.2 Laser melting experiments on $PuO_{2.00}$

To obtain a pronounced freezing arrest, it was necessary to melt enough matter by using sufficiently energetic laser pulses. The dwelling time at the highest temperatures had to be as short as possible to minimize vaporisation, while at the same time care had to be taken not to destroy the samples by thermal shocks due to excessively high heating rates. In order to optimize the pulse parameters, sample C was heated repeatedly with gradually increasing laser power. The thermograms recorded in these successive tests are shown in Figure 5. It can be seen that at low laser power solidification upon cooling was merely indicated by an inflection. By contrast, increasing the power, and consequently the peak surface temperature by about 180 K, led to the formation of more liquid mass, hence to very clear and reproducible freezing arrests.

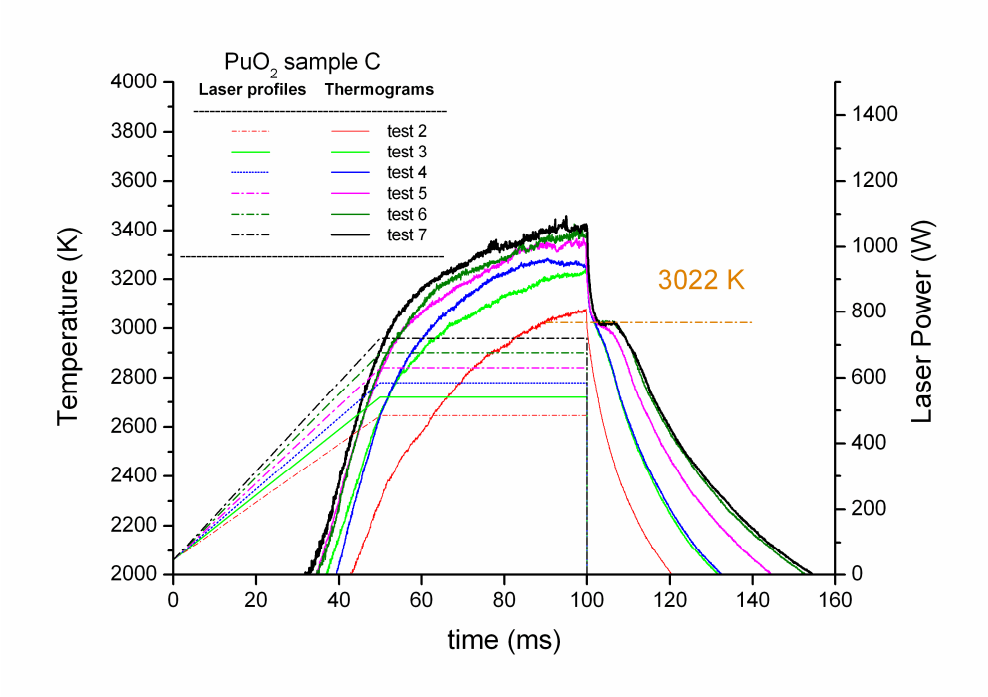


Figure 5: Thermograms recorded in successive laser heating experiments performed on sample C. The observed solidification temperature, 3022 K, is very close to the mean value of all measurements performed on five different samples (3017 ± 28) K. The dash-dotted lines indicate the laser power-vs.-time profiles.

Similar settings were then used in subsequent experiments, allowing a reduction of the number of laser shots per sample, thereby further reducing the risk of cracking and breaking the specimens. The shape of the thermograms and particularly of the freezing arrests varied

slightly depending on the sample morphology (cracks) and its evolution under rapid heating, the occurrence of supercooling, or simply the pyrometer alignment relative to the laser spot. Application of the RLS technique on sample F is depicted in Figure 6. The strength of this technique is in detecting a phase transformation when it is not evident in the thermogram. In this particular case, the melting transition, which is not accompanied by a thermal arrest is easy to spot by the initiation of the noise-like structure, characteristic of a liquid surface, which is even more apparent when plotting the time derivative of the RLS, as was done in this graph. However, the high heating rate did not give enough time for materials to disperse energy and form liquid phase. It was then more relevant to determinate the melting temperature of PuO_2 during cooling.

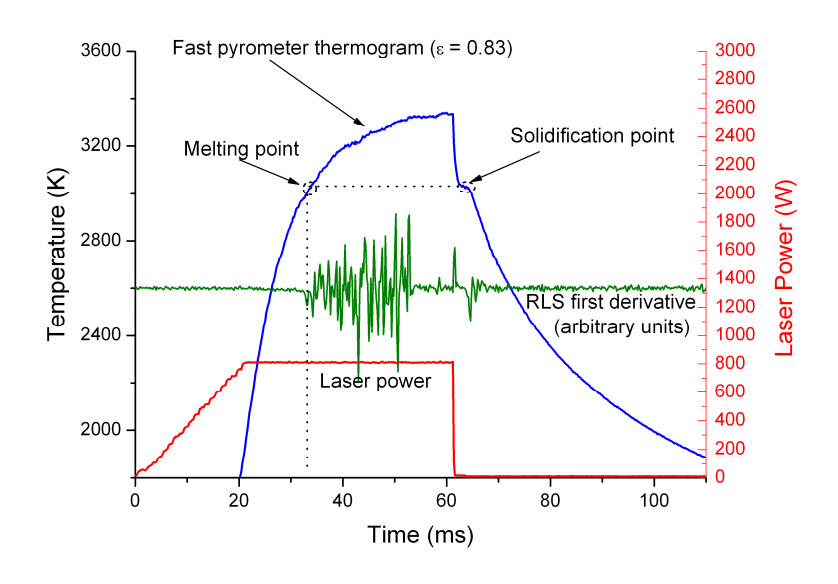


Figure 6: Thermogram, laser power profile and first derivative of the reflected light signal (RLS) recorded in a laser melting experiment on the PuO_2 sample F. Onset of melting on the sample surface can be observed with the help of the RLS technique. A clear thermal arrest due to solidification is visible on the cooling stage, at a temperature corresponding (within uncertainty) to the melting point. The dotted circles around the melting and solidification points indicate the uncertainties on the exact time and temperatures at which melting and solidification occurred.

Figure 7 summarises all experiments that were taken into account for the determination of the PuO_2 melting temperature. The overall reproducibility was excellent. Sample E shows a prominent example of freezing arrests obtained upon recalescence after supercooling. When solidification was not accompanied by a clear horizontal plateau, as was the case for sample D, the freezing temperature was determined from the early and more reproducible part of the arrest, as also suggested by the measurement sequence on sample C.

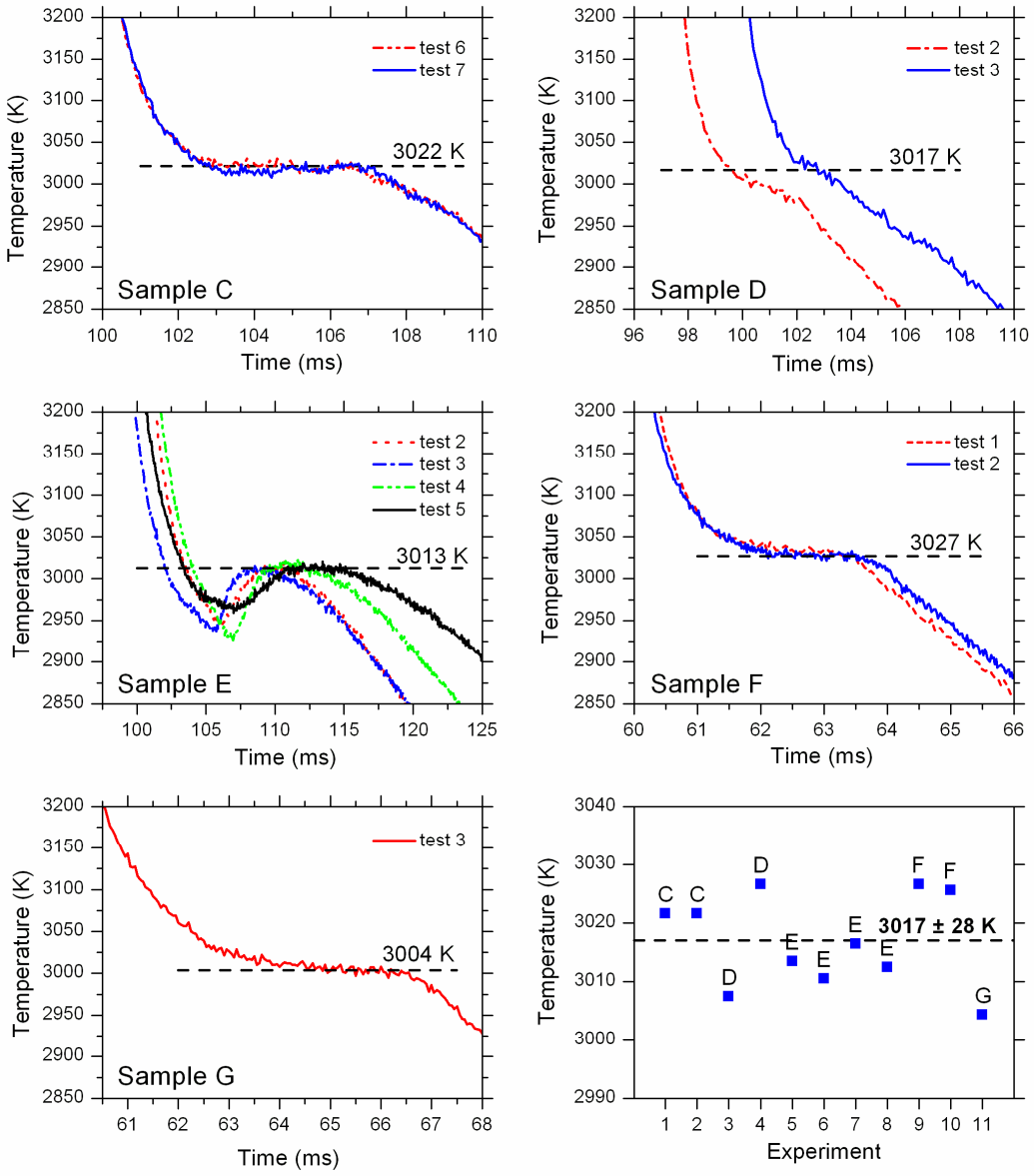


Figure 7: Thermal arrests observed in the cooling stage of thermograms recorded on five PuO_2 samples (C to G). The horizontal dashed lines show the accepted solidification temperature for each sample. A summary of all eleven measurements is shown in the lower right plot with the dashed line indicating the overall mean value for the melting and solidification temperature of PuO_2 (3017 K). In this plot, the indicated ± 28 K uncertainty band combines the current data dispersion with uncertainties on the sample emissivity and the temperature calibration.

As described in chapter 2, the normal spectral emissivity (NSE) of PuO_2 was obtained from an analysis of radiance data measured with the multi-wavelength spectro-pyrometer. One such data set is shown in Figure 8. The two insets depict two of the radiance spectra, one of the liquid sample and one during solidification, as well as the respective least-squares fits based on greybody behaviour. A similar radiance spectrum was recorded and fitted to obtain each of the full (temperature) and empty (NSE) circles plotted in the figure. Because of the limited time resolution (2 ms per point in this case), the temperature and NSE values obtained with this spectro-pyrometer, are influenced by heating and cooling rates, therefore the fitting is only meaningful where the temperature does not vary too rapidly. Moreover, the analysis was more accurate in liquid plutonia at high temperature, where the temperature was more stable and the signal/noise ratio higher. Finally, this instrument was essentially used to estimate the NSE only. Although temperature values obtained from the recorded radiance spectra were always within 2% of those yielded by the fast pyrometer at 652 nm with fixed NSE, only the latter were retained for the reported melting/freezing temperature and error analysis. The mean value of the NSE of liquid and solid PuO_2 near the freezing transition was 0.83 ± 0.05 throughout the analysed wavelength range and for five successive runs on the same sample. This value was used in the conversion of all radiance temperatures measured by the monochromatic pyrometer at 652 nm to true temperatures. It should be noted that the "systematic" uncertainty due to the greybody assumption is difficult to estimate within the current method. Nonetheless, the presented results are in excellent agreement with those calculated ab-initio from low-temperature electronic properties of PuO_2[17]. The "extrapolation to zero wavelength method", also described in Chapter 2, was employed as well in a few cases to check the numerical stability of the current spectral emissivity analysis.

These results are supported not only by the electron density of state calculations performed by Shi et al.[17], but also by earlier direct emissivity measurements carried out by Bober et al.[3] on UO_2, which showed also a behaviour very close to greybody with $\varepsilon_\lambda=0.83$ for UO_2. This latter oxide, which is likely to have very similar optical properties as PuO_2, was already studied by Manara et al.[4] with the current method, yielding an average grey-body emissivity of 0.825 upon solidification. The current value can therefore be reasonably employed, within the experimental uncertainty, for stoichiometric PuO_2 and also all the UO_2 – PuO_2 mixed oxide compositions studied in this research. This assumption leads to a very limited additional uncertainty in the current datapoints, thanks also to the high emissivity value (cf. Equation (1) and related discussion below). The situation is much more difficult for

the metallic uranium and plutonium carbides, which have a lower spectral emissivity which is dependent on wavelength in a non-negligible way (non-greybody behaviour). This point will be extensively addressed in the next chapter.

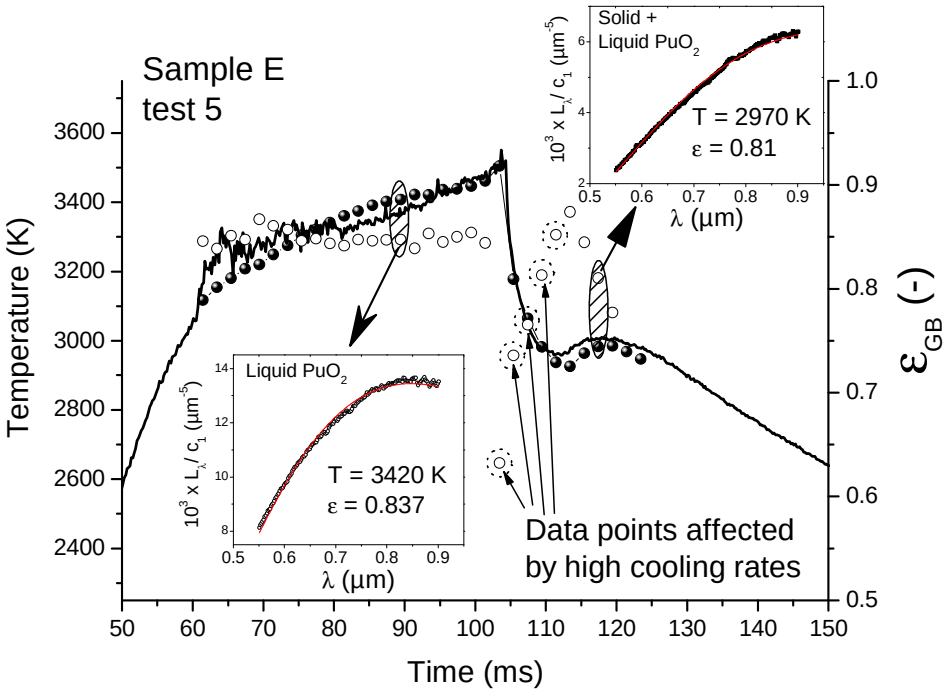


Figure 8: Thermogram recorded on the PuO_2 sample E, including the spectral emissivity analysis based on regression to Planck's radiance law. The two insets show example spectra recorded and fitted in liquid and freezing PuO_2, respectively. In these plots, the radiance L_λ is divided by the first radiation constant c_1 for the sake of simplicity. The main thermogram was obtained using a constant emissivity of 0.83.

A total of eleven measurements of the PuO_2 melting temperature on five different samples yielded a mean value of (3017 ± 28) K (Figure 7). Expanded uncertainties reported here are estimates with a coverage factor k = 2 (2-standard deviations)[18]. Although a direct emissivity measurement in the future will probably reduce the uncertainty, a dramatic change in the melting temperature value is rather unlikely, considering that a change by 10% of the NSE at this wavelength and temperature would translate into a corresponding change in true temperature of less than 1.5%, as can easily be verified using the equation below:

$$\frac{1}{T_r} = \frac{1}{T} - \frac{\lambda}{c_2} \ln \varepsilon \qquad (1)$$

The samples were controlled after each laser experiment. No indication of vaporisation was noticed; the molten/refrozen material looked shiny and well confined in the centre of the sample. The appearance of the non-molten part did not change upon the heating/cooling process. No signs of any (already unlikely) interaction between the molten part and the holding screws were observed. Furthermore, the repeatability of the measurements both for each sample and for the overall five samples (originating from different batches) indicated good chemical and structural stability of the samples under the laser heat treatment.

The micro-structure of a molten and re-solidified sample was studied by SEM. From the micrograph shown in Figure 9 it is likely that the top 30 µm (zones 1 and 2) of the sample were molten. Zone 1 is characterized by the presence of some porosity and columnar grains, whereas zone 2 appears highly dense and porosity-free. Zone 3 represents the unaltered starting material. However, the origin of the formation of the two distinct zones in the molten layer is not clear. A possible explanation is that cooling of the melt starts from two sides, i.e. the sample surface and from the bulk. These two solidification fronts move towards each other and meet at the interface between zone 1 and 2. It is important to stress again that the entire molten matter was surrounded by the bulk so that no contamination was possible.

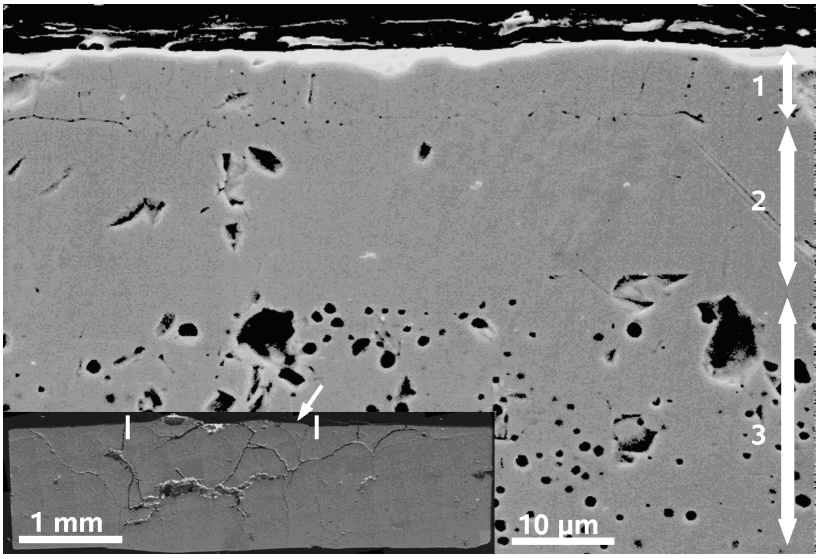


Figure 9: SEM images of a cross-section through a partly molten PuO_2 pellet. The extent of the molten zone is indicated by the two bars in the overview image. The location of the magnified image is marked by the arrow in the inset. Three different zones were observed: 1) A top surface zone where re-solidified grain shapes are visible, zone 2) that shows no porosity, and zone 3), corresponding to the original unheated bulk. A sharp interface can be seen between the three zones.

The molten matter was partially detachable from the bulk. XRD analysis was performed on both a piece of fresh PuO_2 taken from the bulk and a molten/refrozen part. The resulting lattice parameters could be compared and, using the analysis reported by Gardner *et al.*[15], the respective O/Pu ratios before and after melting could be determined. Figure 10 shows the two diffractograms obtained on sample G before and after melting and freezing. One can clearly observe that both pieces had the same crystal structure, fluorite-like face centred cubic. It was necessary to magnify some of the XRD pattern features at high diffraction angles to see some slight differences (insert in Figure 10). The fcc lattice parameter obtained for the unmolten material was 5.396(1) Å. The diffractogram of the molten part displayed peaks slightly broader and twinned, possibly corresponding to the presence of two very similar phases with lattice parameters of 5.4018(1) Å and 5.3989(1) Å. In reality, the molten part being only 15 mg in weight, it is very likely that it was not removed and isolated perfectly, so that non-negligible traces of unmolten material were analysed by XRD together with the frozen one. Taking into account the uncertainties, calculated from the equipment precision and the fit of the diffractogram, the measured lattice parameters based on the correlation curve reported in reference 16 corresponded in both cases to stoichiometric plutonium dioxide $PuO_{2.00\pm0.01}$. This uncertainty on the composition is largely negligible in terms of observable effects on the melting temperature.

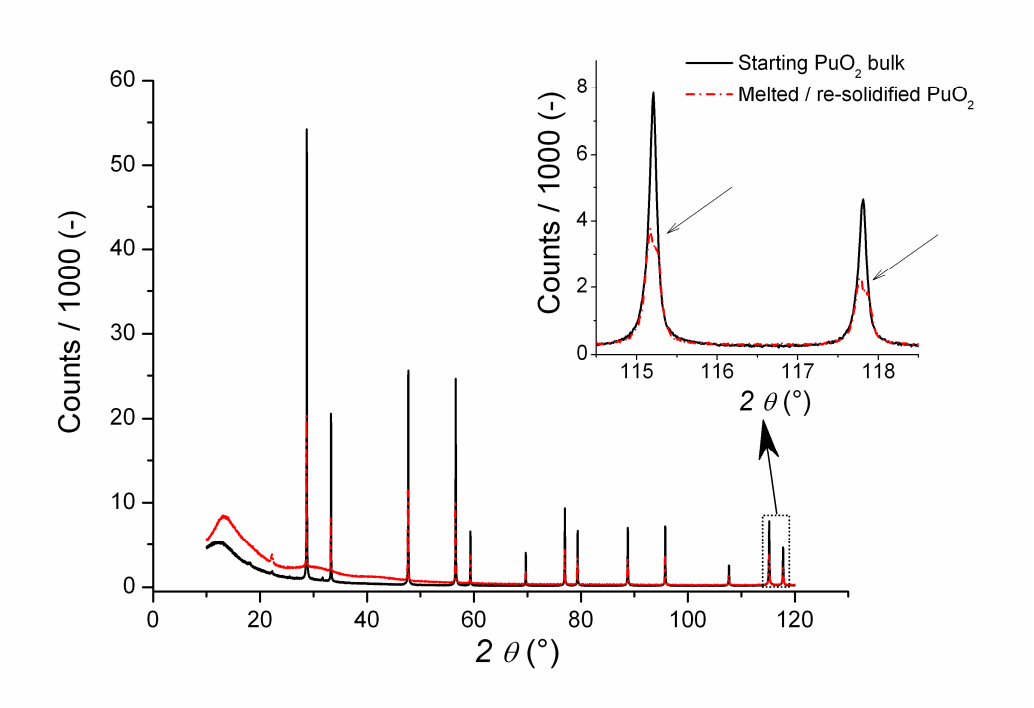


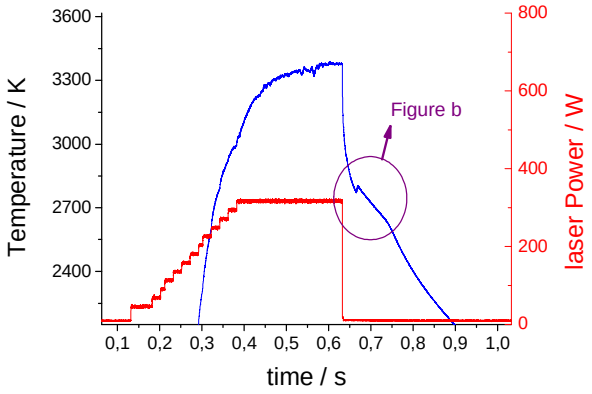
Figure 10: XRD comparison of the bulk and molten/frozen part of sample G. Inset: magnification of XRD comparison of the bulk and molten/frozen part of sample G at high diffraction angles.

EPMA was also performed on molten and refrozen plutonium dioxide samples in order to check their composition and homogeneity. This kind of characterization, although affected by a larger uncertainty, corroborated the XRD results. It can therefore be assured that the PuO_2 samples investigated were, within the experimental uncertainty, stoichiometric and pure before and after being subjected to laser heating and melting. This implies, moreover, that stoichiometric plutonium dioxide melts congruently as any substantial composition difference between solid and liquid would have resulted in segregation in the refrozen material, as was never observed in the current samples.

3.3 PuO_{2-x}

The previous section deals with stoichiometric plutonium dioxide. A second approach to the high temperature behavior of this compound consists in the study of non-stoichiometric samples. It is in particular interesting to have a view of the melting temperature of PuO_{2-x} as a function of the oxygen content. In fact, different hypotheses on the plutonium-oxygen phase diagram exist, proposing congruent melting and maximum of the solidus/ liquidus lines either at O/Pu=2.00 (e.g.: reference 11) or at O/Pu<2 (e.g.: reference 12).

PuO_{2-x} samples A and B were sintered in Ar+5% H_2 (1500 ppm H_2O) and not annealed in air (Table 1 above). The O/Pu of these samples was established by thermogravimetry to be $PuO_{1.83}$. Laser heating performed under air led in these cases to more complex thermograms than those obtained for stoichiometric PuO_2. Three thermograms were obtained with sample A and one with B. All of them presented the same behavior during cooling. Figure 11.a displays the thermogram obtained with sample B. A first inflexion point, visible with difficulty, is observable around 2954 K. This feature is followed by a thermal arrest characterized by pronounced supercooling and recalescence, after which a second slight inflexion is also present at lower temperature (figure 11.b).



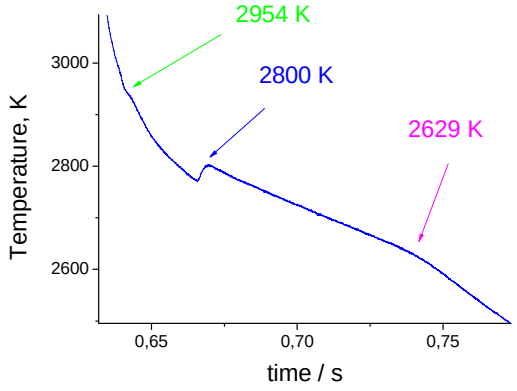


Figure 11.a: Thermogram, laser power profile recorded in a laser melting experiment on the sample B.

Figure 11.b: cooling part of the thermogram.

The values obtained from all the thermograms recorded on these PuO_{2-x} samples are summarized in figure 12. The first (highest temperature) transition is difficult to observe but well reproducible from one shot to the other, also in different samples. The second thermal arrest, much more pronounced, is likely to correspond to the total solidification of most of the molten mass. Some segregation which probably occurs in the solid/liquid/solid transition, due to the high heating and cooling rates and the non-congruency of the transition. This would result in the formation of a small liquid mass depleted in oxygen, which would then solidify at a lower temperature, explaining the third, less pronounced inflection in the thermograms. This interpretation of the experimental curves is obviously largely speculative, and should be supported by further experiments and a suitable theoretical simulation of the heating cycles [cf. reference 19]. Nonetheless, this picture gives, at least in a first approach, a satisfactory explanation of all the experimental observations, including the pre- and post-melting XRD analyses. Figure 13 shows these XRD analyses performed on sample B before and after the laser melting experiments. A second phase ($PuO_{1.52}$) is present in both cases in addition to PuO_{2-x}. Nonetheless, the two diffractograms look very similar, indicating that if segregation is likely to occur upon the melting/solidification process, this should result in the formation of a very limited amount of oxygen-depleted phase.

In summary, and in a first approximation, these experimental facts can explain the three transitions observed on the cooling flank of the thermograms: the first and the second

may correspond to the solidus and liquidus of the initial composition, whereas the third can be attributed to the solidus of a phase poorer in oxygen.

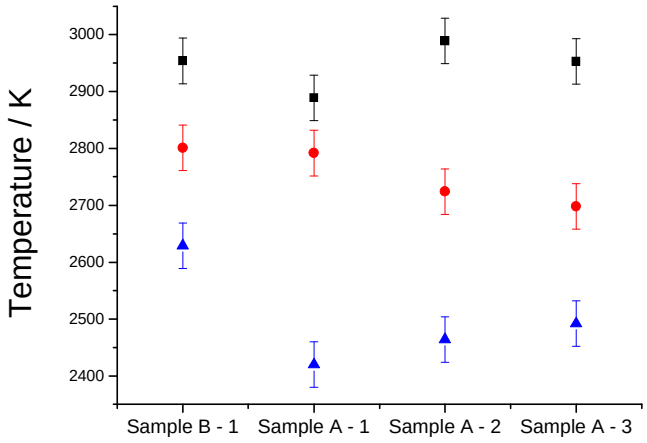


Figure 12: summary of the values recorded on the PuO_{2-x} samples.

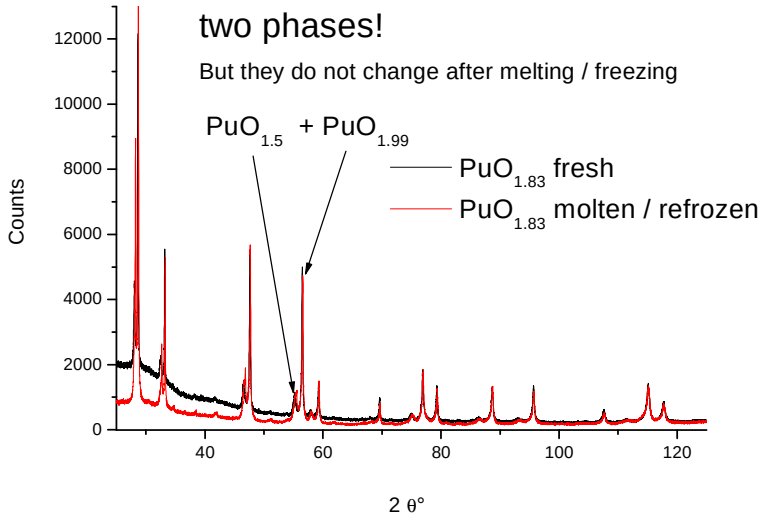


Figure 13: XRD analyses on sample B before and after laser heating.

A second series of tests was performed to observe the behavior of stoichiometric PuO_2 under reducing conditions. Four experiments were performed under air with the stoichiometric $PuO_{2.00}$ sample E: the melting temperatures were constant and equal, within uncertainty, to the already established melting point of stoichiometric $PuO_{2.00}$ (figure 7). The sample was then left in the autoclave whereby the air was removed and substituted by argon.

A similar laser pulse was then applied to heat the sample, but under argon the solidification thermal arrests were observed at a lower temperature. A second identical laser shot was then repeated under argon, and the thermal arrest temperature decreased again. The autoclave was finally purged to perform new experiments under air and after two consecutive heat cycles the melting temperature rose again very close to the established $PuO_{2.00}$ melting point.

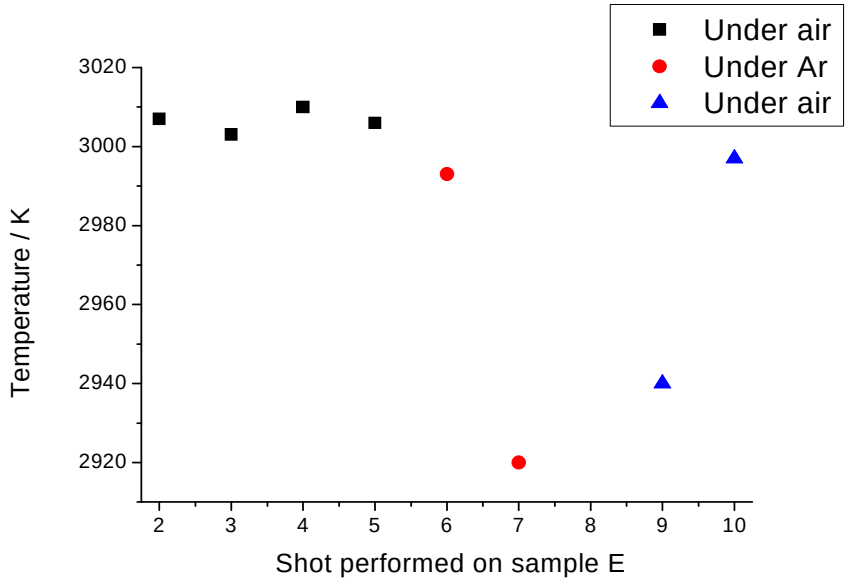


Figure 14: Consecutive experiments performed under air or argon on a stoichiometric $PuO_{2.00}$ sample, shot 8 did not bring any result.

In conclusion, it has been observed that by varying the atmosphere, the melting/freezing temperatures of PuO_{2-x} change. More precisely, their values decrease together with the oxygen content and reversely. Since it has been proven that, in these conditions, plutonium dioxide can not be hyperstoichiometric[15], the observed melting temperatures must correspond to different O/Pu ratio lower than 2. It is reasonable to assume that the lower is the oxygen partial pressure in the atmosphere, the lower must be the actual O/Pu ratio in the solidifying sample. Contrarily, when shooting under air, the sample surface can be re-oxidized and the ratio O/Pu restored to close to 2.

3.4 Discussion

The current results are in line with the recent conclusion of Kato *et al.*[4], who conclude that the older investigations[7,6] yielded too low transition temperatures because of sample-containment interaction during the heat treatments across the melting transition. Yet, Kato

proposed a temperature of melting still 170 K lower than that found in this work (Figure 7). This could be due to underestimation of the interaction between the PuO_2-rich MOX samples and the rhenium capsule employed during the experiments. These interactions could result from not only the contamination of the plutonium dioxide samples with metal coming from the holder, but also, and probably more effectively, the chemical diffusion of oxygen from the samples into the crucible, as the authors themselves pointed out. Moreover, it should be noted that most researchers performed this sort of measurements with pyrometers calibrated against the melting points of metals recommended as secondary references. However, even during the measurement of these reference melting points reaction between the standard samples and their containment could have occurred, thus affecting the entire calibration procedure and, hence, the temperature scale definition. The main goal of the current experimental technique is to neutralize all these possible error sources. In addition, a series of post-melting analyses were performed to make sure that the thermal arrests measured in samples with nominal O/Pu = 2.00, actually corresponded to the melting point of stoichiometric PuO_2 and that no detectable composition changes occurred at high temperature because of incongruent vaporisation or segregation.

Studies on sub-stoichiometric samples are still ongoing. Nonetheless, relying on the fact (checked, essentially, by pre- and post-melting XRD) that the reported melting/freezing temperatures were effectively measured for the compositions $PuO_{2.00}$ in the stoichiometric samples and $PuO_{1.83}$ in the sub-stoichiometric ones (samples A and B), the current data points can be superimposed to the Pu-O phase diagram optimized by Gueneau et al.[11] (figure 15). These points clearly suggest that only stoichiometric PuO_2 melts congruently, whereas the solidus and liquidus temperatures, well separated in the hypostoichiometric domain, tend to decrease whith decreasing O/Pu ratio.

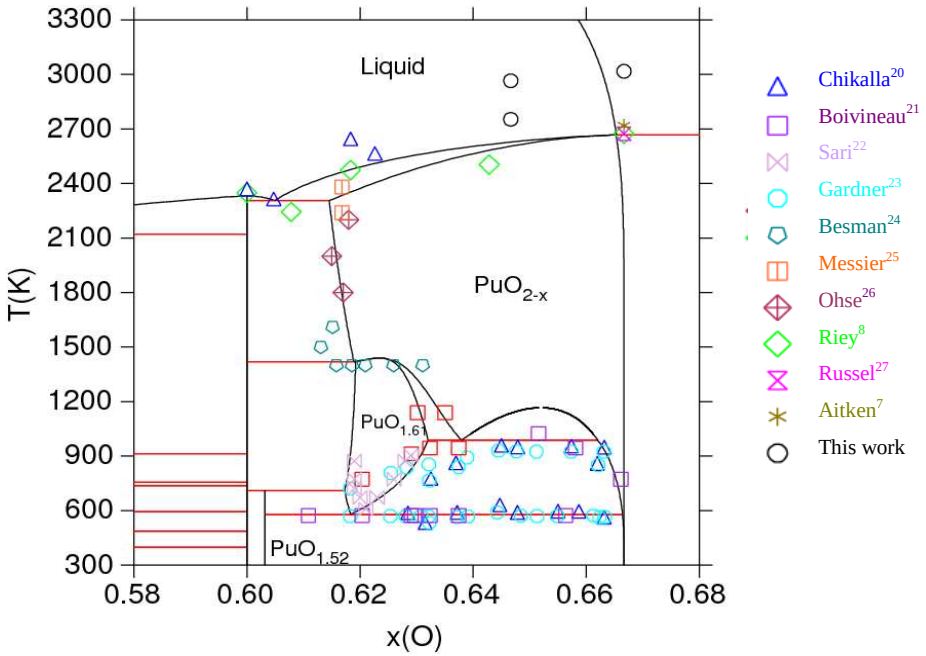


Figure 15: current data points superimposed to the Pu-O phase diagram optimized by Gueneau et al.[11]

4 Uranium – plutonium mixed dioxides (MOX)

Five different compositions of (U, Pu) mixed oxides (MOX) have been studied in this work (Table 2). Additional difficulties had to be taken into account for these compounds with respect to the pure end members of this pseudo-binary system (UO_2 and PuO_2). In particular, it is difficult to control the actual and the exact uranium, plutonium and consequently oxygen distribution in the material. Moreover, U/Pu/O segregation was more likely to occur here during the heating experiments. In addition, evaporation phenomena had to be limited as much as possible.

4.1 Sample preparation

A series of 5 compositions of mixed $(U,Pu)O_2$ samples from 25 to 90 mol% PuO_2 were prepared (Table 2). They were named with the label MOX followed by the PuO_2 mol% and a letter is assigned to distinguish samples having the same composition. MOX 25 A is the first sample of MOX prepared with 25 mol% of PuO_2. The starting material was powder or beads obtained by gel-supported precipitation (SOL-GEL). In the case of the MOX 80 and 90,

they are prepared by infiltration performed on PuO_2 powder with a solution of uranium (1 $mol \cdot L^{-1}$). Calcinations are performed in three steps, two heating cycles in air, the first at 673 K during 2 h and the second at 1073 K during 2 h followed by a heat treatment under Ar + 1500 ppm H_2 during 4 h at 1073 K. Disk-shaped samples of 8 to 9 mm in diameter and about 4 mm in thickness were obtained using a bi-directional press. The samples were then sintered in an atmosphere of Ar + H_2 with traces of H_2O to obtain dense material. After sintering, the samples were sub-stoichiometric, (O/M) < 2. Thermogravimetry experiments (TG) were performed to set the annealing parameters and obtain stoichiometric samples. In these TG tests, MOX samples were heated under an oxidising gas flux of CO/CO_2 (1/100) with an oxygen potential of 350-400 $kJ \cdot mol^{-1}$, depending on the U/Pu composition. Since the gas composition was fixed, the oxygen potential was imposed by gradually increasing temperature, according to the equation:

$$\Delta G_{O2} = RT \ln p_{O2} \qquad (2)$$

Here, the oxygen partial pressure is imposed by the CO / CO_2 equilibrium

$$2CO + O_2 \rightarrow 2CO_2$$

And

$$p_{O_2} = \frac{p_{CO_2}^2}{p_{CO}^2} \cdot K_{EQ} \qquad (3)$$

In Eq. (2), the equilibrium constant K_{EQ} can be calculated after the data recommended in reference 28:

$$K_{EQ} = \exp(-566+0.17506 \cdot T \ kJ \cdot mol^{-1}) \qquad (4).$$

Once a steady weight was obtained at a given temperature (Figure 16), the corresponding oxygen potential was assumed to be the one in equilibrium with the stoichiometric MOX (O/M = 2).

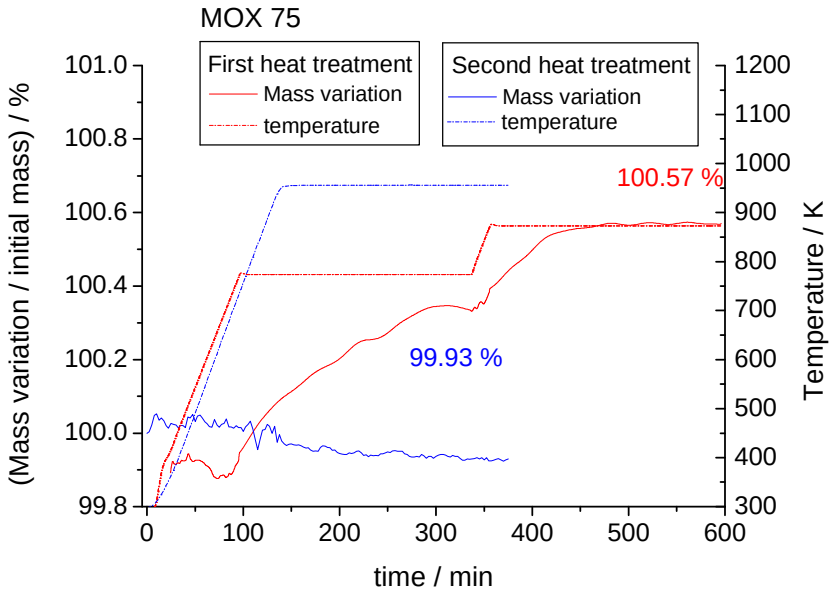


Figure 16: Two successive heat treatments during thermogravimetry measurements, mass variation values lower than 100% indicate experimental fluctuations.

The same oxygen potential was then used for the oxidizing annealing of the disks prepared for the laser melting experiments. Two such annealing cycles were performed per each composition. The relative weight gain per each sample was checked to correspond to the one previously measured by TG. If, in addition, no further change was noticed after annealing the samples for a second time, it was considered that $(U,Pu)O_{2.00}$ stoichiometry had been reached. Both the sintering and the oxidising annealing treatments had the secondary, very important goal of homogenising the U-Pu distribution inside the sample. As previously stated, this is an essential point also for ensuring a homogeneous oxygen distribution in the sample. It should be note that the whole procedure for the oxidation of MOX samples to O/M = 2 was more uncertain and less precise than the one employed for the preparation of stoichiometric pure PuO_2. This was due to the presence of uranium dioxide, which, unlike PuO_2, has a tendency to be further oxidised to UO_{2+x}. This risk was minimised in the current work by annealing the samples at T< 1000°C.

Sample	Name	Starting Materials	Sintering (gas / temperature (K) / time (h))	Annealing (gas / temperature (K) / time
UO2	A	Pellet already prepared		
MOX 25	A – B – C	Sol gel	Ar +2% H_2 + 1500 ppm H_2O / 1923 / 8	no
	D – E	Sol gel		CO/CO_2 (1/100) / 873 / 8
MOX 50	A – B C - D	Sol gel	Ar +2% H_2 + 1500 ppm H_2O / 1923 / 8	First : CO/CO_2 (1/100) / 873 / 8 Second: CO/CO_2 (1/100) / 973 / 3
MOX 75	A - B	Sol gel	Ar +2% H_2 + 1500 ppm H_2O / 1923 / 8	First : CO/CO_2 (1/100) / 873 / 8 Second: CO/CO_2 (1/100) / 973 / 3
MOX 80	A – B – C	Infiltration	Ar +2% H_2 + 1500 ppm H_2O / 1923 / 8	Air / 1300 / 8
MOX 90	A –B - C	Infiltration	Ar +2% H_2 + 1500 ppm H_2O / 1923 / 8	Air / 1300 / 8

Table 2: MOX composition, starting material and heat treatments.

4.2 Laser melting experiments on MOX samples

Laser melting experiments were performed on (U,Pu) MOX samples with the same procedure already employed for the pure uranium and plutonium dioxides. Thermograms recorded for different compositions are shown in figures 17 to 19.

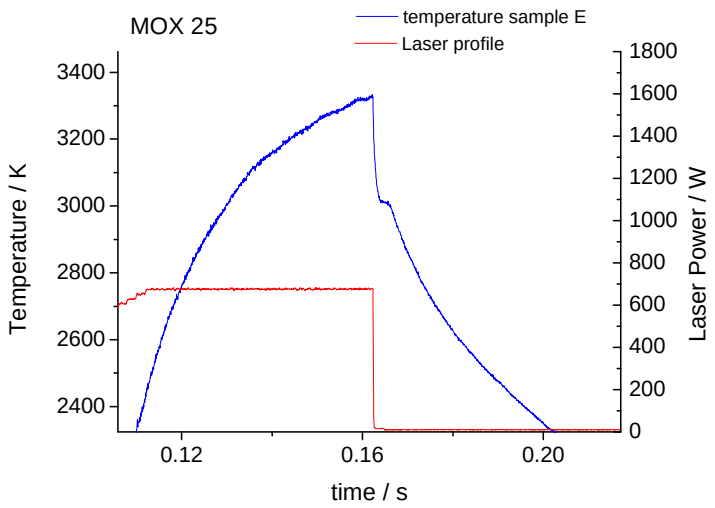


Figure 17: Thermograms recorded with the fast pyrometer at 652 nm on MOX 25 E.

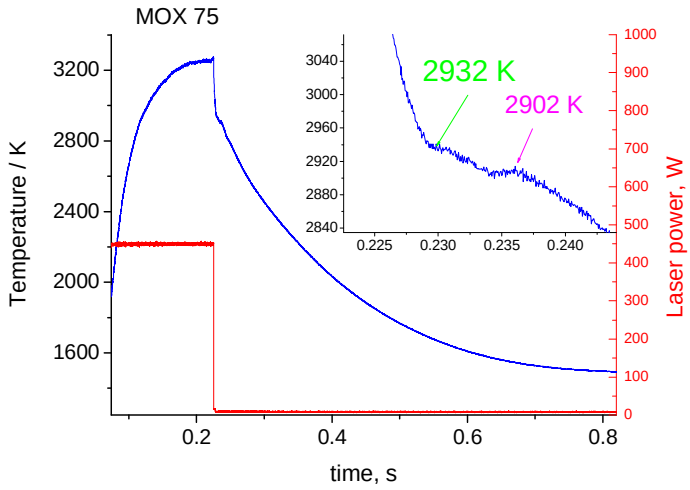


Figure 18: Thermograms recorded with the fast pyrometer at 652 nm on MOX 75 A.

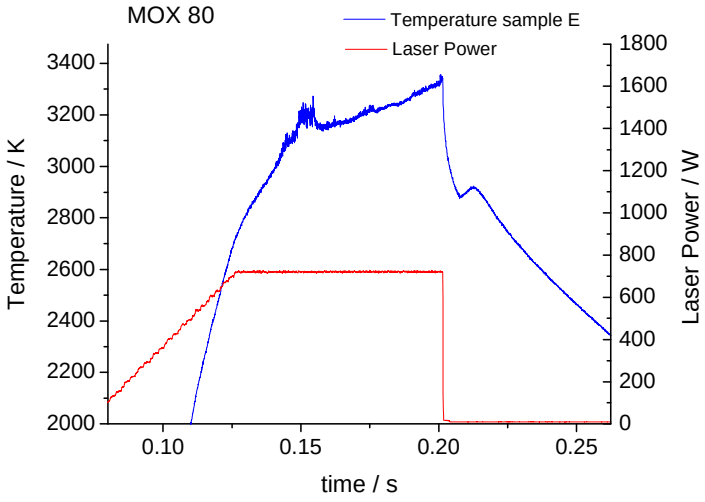


Figure 19: Thermograms recorded with the fast pyrometer at 652 nm on MOX 80 B.

The solidification arrests were often close to a plateau, as would be expected for a congruent phase transition. It would, however, be unlikely that solidification occurs congruently for the different mixed compositions investigated. Therefore it can be concluded that the solidus and liquidus points could be too close together to be observable at the cooling rates produced with the current method. It can be however noticed that, in some cases, as in figure 18, a double arrest or a double inflection (slope change) was observed, as expected for non-congruent melting with well separated solidus/liquidus temperatures. It will be necessary in future to reproduce these experiments with more samples and this second inflexion could be highlighted by performing slower laser heat treatments with lower cooling rates. A large undercooling (several hundreds K) was observed in a few cases in MOX50 and MOX25 samples. The origin of this phenomenon occurring only in a few isolated tests has not found any satisfactory explanation. Independently, a thermal arrest close to the temperature observed in other more regular thermograms was recorded after the undercooling and recalescence in all these cases. All the temperatures, at which thermal arrests or inflections were selected, correspond to the first shot on the different samples. They were determined according to the criteria explained above for pure $PuO_{2.00}$. These values are summarized in Table 3 and plotted in Figure 22. The larger uncertainties for mixed oxide compositions were calculated taking into account the small number of thermograms.

Sample	Number of thermograms	Melting point (K)	Uncertainty (K)
$UO_{2.00}$	4	3130	20
MOX 25	3	3008	35
MOX 50	3	2872	35
MOX 75	1	2950	35
MOX 80	2	2965	35
MOX 90	2	3002	35
$PuO_{2.00}$	11	3017	28

Table 3: Temperature of the thermal arrest at the wavelength λ = 652 nm and with the emissivity ε = 0.83.

One can observe that uncertainty bands are rather large, especially for intermediate compositions. It is possible, that for these compositions, the temperature gradients induced in the sample during the fast heating / cooling cycles result in oxygen migration and non-homogeneous distribution during the measurements. This sort of phenomenon should not affect the small area of the pyrometer focal spot, where local equilibrium conditions are assumed. However, this local equilibrium assumption might be less accurate in these particular cases, which could explain the large data dispersion and, also, the average values lower than those of Kato et al. for the samples MOX25 and MOX50. In fact, deviations towards both hypo- and hyper-stoichiometry have been observed to result in lower melting and solidification temperatures in the single oxides $UO_{2\pm x}$ and PuO_{2-x} (discussed in the previous section). Yet, the current data points are not far from those of earlier authors and still within the large data scatter. In order to deepen this point, MOX samples have been analyzed after the laser heating cycles.

4.3 Post-melting sample characterization

a) X-Ray diffraction

After the laser experiments, the samples were extremely fragile. Thus, the molten part was separated from the bulk and XRD analyses were performed on crushed materials. The molten part was thin, a few hundreds µm, and the corresponding mass was only about 20 mg which complicated the preparation of homogeneous and flat samples. Even if the diffractograms presented well defined peaks and reasonable signal/noise ratio, some of the curves were difficult to fit. Part of this problem was due to partial detachment of the sample from the X-ray diffractometer holder. In fact, the powdered sample was pressed and mixed with glue to obtain a thin layer, however, part of the matter could remain stuck to the mortar affecting the flatness of the sample surface. This effect is particularly visible at the lowest angle of the diffractograms. Therefore, a second method was used to calculate the cell parameters.

The spacing *d* between diffracting planes is defined by Bragg's law as:

$$d = \frac{n \cdot \lambda}{2 \cdot \sin(\theta)} \qquad (4)$$

θ and λ are respectively the incident angle and the wavelength of the X-ray beam, *n* is any integer (1 in this work). For a specific plane of Miller coefficients [h,k,l] in a cubic crystal of lattice parameter *a*, the value of *d* can be obtained through the equation:

$$d_{h,k,l} = \frac{a}{\sqrt{h^2 + k^2 + l^2}} \quad (5)$$

On the diffractograms, the position of the peak at the highest angle was determined with good precision. Since the measurements were performed from $2 \cdot \theta$ = 20 to 120°, this peak corresponds to the plane [6,0,0]. From the previous equations, the cell parameter could be calculated as:

$$a = \frac{\sqrt{h^2 + k^2 + l^2} \cdot \lambda}{2 \cdot \sin(\theta)} = \frac{4.62168}{\sin(\theta)} \quad (6)$$

The cell parameters obtained from the fitting of diffractograms (with Fullprof) and from the technique explained above are summarised in table 4.

Sample	**part**	**Fullprof**	**Calculated**
MOX25 C Three laser shots were performed on this sample and the obtained thermal arrests decreased from about 200 K between the first and the third experiments. The molten part shows two phases and an important shift of the background at low angles.	Bulk (two measurements)	5.453 (2)	5.454 (2) 5.454 (2)
	molten	5.45 (1)	5.423 (5) 5.450 (5)
MOX50 B One laser experiment performed on this sample. One phase observed in both molten and bulk samples.	bulk		5.406 (5)
	molten	5.415 (3)	5.415 (3)
MOX75 B Several laser experiments performed on this sample. One phase observed in both molten and bulk samples.	bulk	5.414 (3)	5.413 (3)
	molten	5.411 (3)	5.409 (3)

Table 4: cell parameters calculated for the MOX 25, 50 and 75 from the bulk and molten area.

The cell parameters of stoichiometric MOX were observed to follow Vegard's law[6]. Thus, the actual results are compared to Vegard's law in figure 20. The MOX 25 and MOX 75 cell parameters follow fairly well Vegard's law. In MOX 25, however, a secondary phase was observed in the molten part with a smaller cell parameter. Three shots were performed on

this sample and the thermal arrest temperature decreased from one laser shot to the next. It is therefore possible that evaporation or segregation phenomena took place at high temperature. The lattice parameter of MOX 50 is lower than predicted, although only one phase was detected for this composition. Different explanations are possible, involving non-homogeneous oxygen distribution or U/Pu ratio.

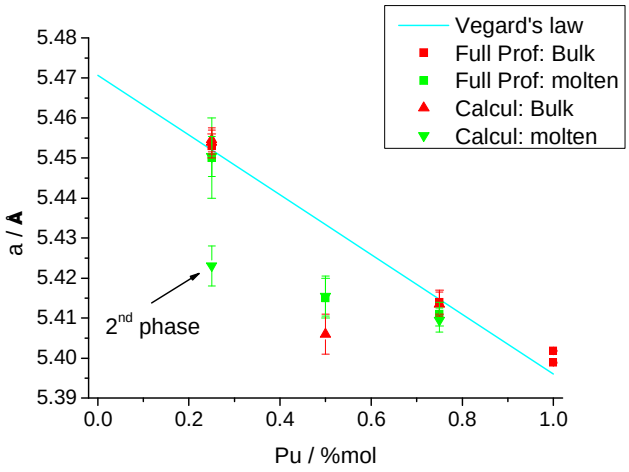
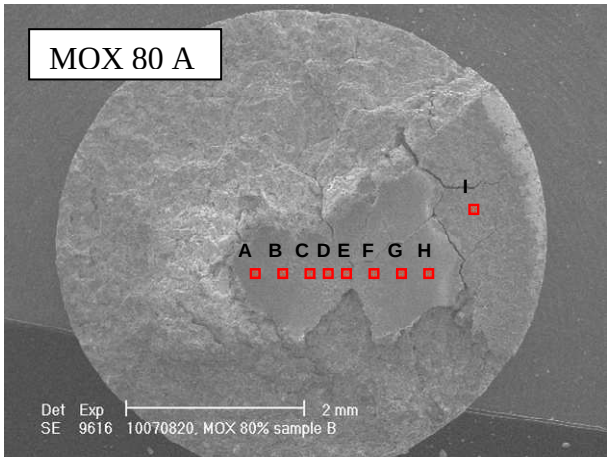


Figure 20: calculated cell parameters compared to the Vegard's law.

b) SEM - EDS

Two main features influence the cell parameters of the MOX, the O/M ratio and the U/Pu ratio. To help a correct interpretation of the XRD results, SEM and Energy Dispersion Spectroscopy (EDS) analyses were performed to control the surface homogeneity and U/Pu ratio of the different samples after laser heating. Although laser melted samples were generally broken after the heating cycles, it was normally possible to analyse parts of the molten and non molten surface. EDS analyses were performed on square spots with 0.01 mm side. As an example, Figure 21 a shows a EDS scan performed on the surface of sample MOX 80 A after laser melting. Eight measurements were performed on the molten area and one on the bulk. The U/(U+Pu) ratio was measured to be constant within the instrumental uncertainties plotted in Figure 21 b. It seems therefore reasonable to assume that the U/Pu ratio does not vary enough to influence the melting temperature measurements in the current laser heating experiments.



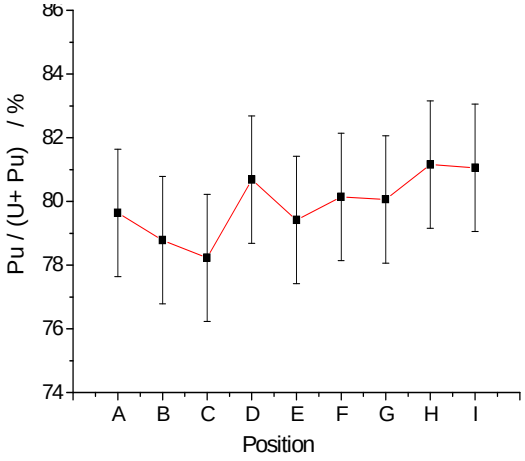


Figure 21 a: nine positions where EDS analyses were performed are represented by the red squares.

Figure 21 b: Pu/(U+Pu) values obtained from the EDS analyses.

4.4 Discussion

Despite the large data dispersion and the described issues related to oxygen distribution in the laser irradiated samples, a sufficiently clear trend can be deduced from Figure 22: the solidus/liquidus curves of the pseudo-binary system UO_2 – PuO_2 seem to have maxima for the pure end members and a minimum for intermediate compositions, most probably between 40 mol % and 60 mol % Pu.

In a more general overview, the current data points, plotted in Figure 22 together with the review graph published by Kato et al., look in fair agreement with those of previous researchers in the U-rich part of the UO_2 – PuO_2 pseudo-binary system. In this range, however, the present solidification temperatures are somewhat underestimated with respect to those of Kato et al., possibly due to non-homogeneous oxygen distribution within the temperature gradients produced in the current samples. In the composition range with mol%PuO_2 > 50, instead, the current solidification points are higher than all those previously observed, up to the newly established congruent melting / freezing point of pure PuO_2 at 3017 K. The disagreement with previous data has been satisfactorily explained as being due to extensive interaction between sample and crucible in traditional heating techniques. This trend in the Pu-rich part of the pseudo-binary diagram implies the existence of a minimum

congruent freezing point at intermediate compositions. The solidification arrest similar to a congruent plateau in the MOX50 suggests that the minimum is probably very close to 50 mol% PuO_2. The large uncertainty, however, calls for further research to confirm this conclusion.

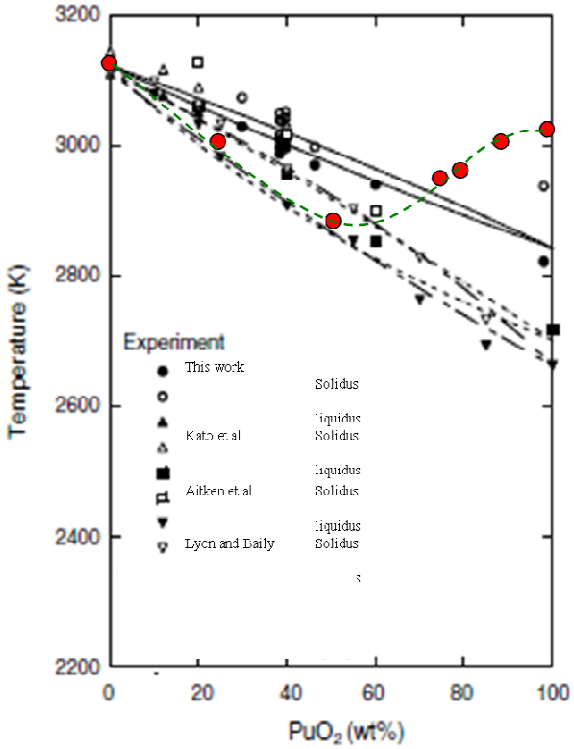


Figure 22: The UO2 – PuO2 pseudo-binary phase diagram with the current data point compared to literature data. The dotted curves suggest an approximate trend for the solidus and liquidus lines assessed in this work.

5 Neptunium Dioxide

5.1 Sample Preparation

Three NpO_{2-x} samples have been prepared, containing ^{237}Np. The starting material was powder. Disk-shaped samples of 4 mm in diameter and about 1 mm in thickness were obtained using a bi-directional press. The samples were then sintered in an atmosphere of $Ar + H_2$ with approximately 1500 ppm of H_2O to obtain dense material. In order to obtain the exact O/Np = 2 stoichiometry, the samples were annealed under a flow of air at 1823 K for 10 hours. No weight change was observed after a second annealing, and this was taken as a satisfactory test that the stoichiometric O / Np = 2 composition had been reached.

5.2 Laser Heating

Only the first of the three NpO_2 samples could be investigated by laser heating in the current research project. Several tests were carried out on a NpO_2 sample held in compressed air (2.5 bar). A solidification arrest was clearly detected, although not always perfectly flat. This irregular and not satisfactorily reproducible shape of the solidification arrest is attributed to morphological changes of the sample surface over successive laser shots. The freezing arrest was observed in a well reproducible temperature range over six successive shots on the same sample (Figure 23). This indicated that no segregation or non-congruent evaporation occurred during the heating cycles across melting, most probably confirming that NpO_2 melts congruently, as already postulated in the earlier research of Chikalla et al.[30] and of Richter and Sari[31]. The spectral emissivity of freezing NpO_2 was also studied in this work by multi-channel VIS – NIR pyrometry, the technique already presented in Chapter 2 and employed for plutonium dioxide and MOX as reported earlier in this chapter. Both the “fit to Planck curves” and the “extrapolation to zero wavelength” approaches were successfully used to exploit the multi-wavelength pyrometry data. Results obtained by the second approach are reported in Figure 24. The radiance temperature spectrum recorded during the freezing arrest with an integration time of 2 ms is well fitted with a greybody (constant) emissivity of 0.81±0.05 and a true temperature of (3040 ± 40) K. This emissivity value is very close to the one obtained and recommended for UO_2 and PuO_2, which is absolutely reasonable

considering the identical Fm3m structure of these oxides. The melting / solidification temperature value reported above has been observed to be reproducible, within the given uncertainty limits, over six different experiments. However, the uncertainty band might be reduced by testing other "fresh" samples, where the surface morphology effect is smaller.

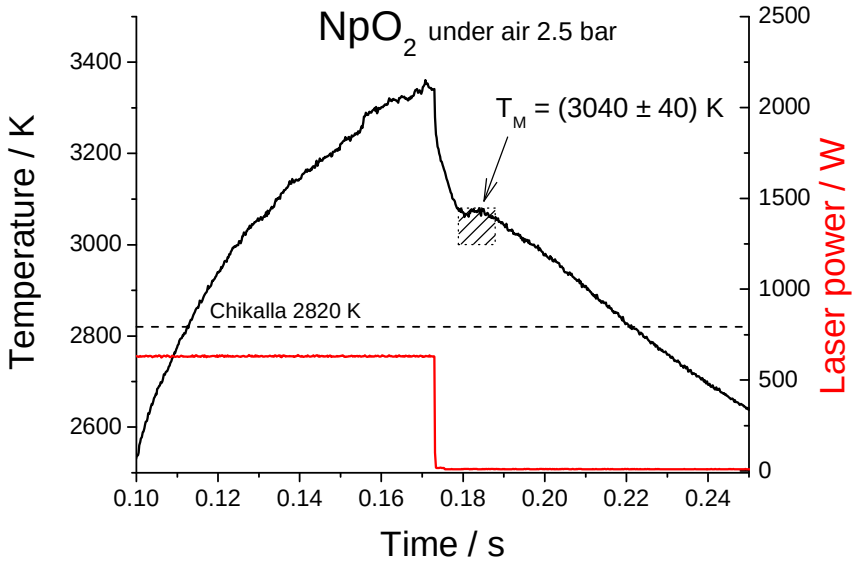


Figure 23: One of the six thermograms successfully recorded on NpO_2. The dotted rectangle indicates the temperature range in which thermal arrests have been observed in all the experiments.

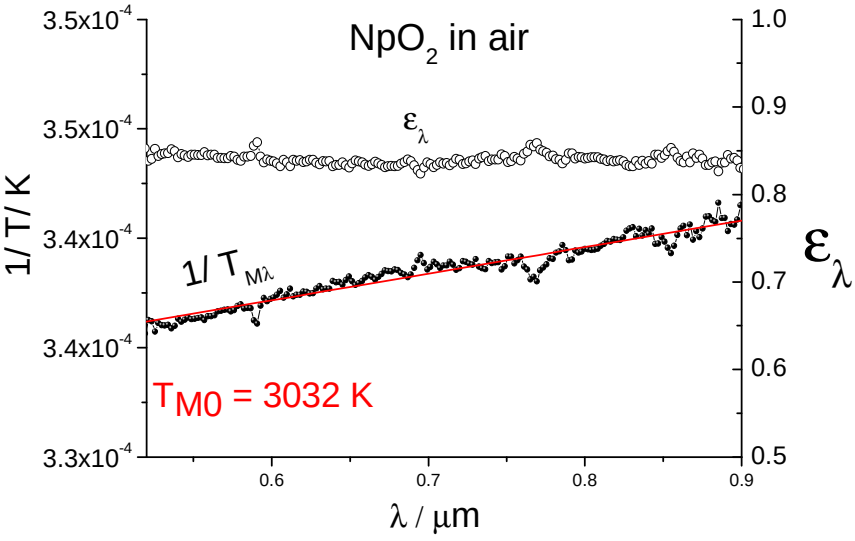


Figure 24: The extrapolation to zero wavelength method for the emissivity analysis during freezing applied to one of the six successful laser heating cycles performed on NpO_2. In this case, the true solidification temperature was observed to be 3032 K, within the reported uncertainty.

5.3 Discussion

The melting / freezing point observed by laser heating on NpO_2 at (3040 ± 40) K, is more than 200 K higher than the value recommended by Chikalla et al. in 1971 and Richter and Sari in 1987. All these authors used traditional heating methods (induction furnaces under blackbody conditions) for their high-temperature investigations. Under such conditions, the NpO_2 sample probably reacted extensively with the containment, because of its high oxygen potential. Thus a situation similar to that already discussed for pure PuO_2 is observed here: fast heating under containerless conditions has shown that the reaction between sample and containment probably lead in more traditional heating techniques to an apparent freezing temperature much lower than the one measured for the pure uncontaminated compound.

6 References – Chapter 3

1. C. Guéneau, A. Chartier, L. Van Brutzel, Chapter 9: the Actinide Oxides, Comprehensive Nuclear Materials, Edited by R. Konings, Elsevier, to be published.
2. Hj Matzke J. Less Common Metals 1986, K Lassmann JNM 1986
3. M. Bober, High Temp. High Pressures, 12 (1980) 297.
4. D. Manara, C. Ronchi, M. Sheindlin, M. Lewis, M. Brykin, J. Nucl. Mater. 342 (2005) 148.
5. M. Kato, K. Morimoto, H. Sugata, K. Konashi, M. Kashimura, T. Abe, J. Nucl. Mater. 373 (2008) 237.
6. W. L. Lyon, W. E. Baily, J. Nucl. Mater. 22 (1967) 332.
7. E. A. Aitken, S. K. Evans, General Electric, GEAP-5672, 1968.
8. B. Riley, Sci. Ceram. 5 (1970) 83.
9. R. J. Lemire, J. Fuger, H. Nitsche, P. E. Potter, M. H. Rand, J. Rydberg, K. Spahiu, J. C. Sullivan, W. J. Ullman, P. Vitorge and H. Wanner, OECD-NEA, Chemical Thermodynamics Series Chemical Thermodynamics of Neptunium and Plutonium, Elsevier, North-Holland 4 (2001) 333.
10. J. J. Carbajo, G. L. Yoder, S. G. Popov, V. K. Ivanov, J. Nucl. Mater. 299 (2001) 181.
11. C. Guéneau, C. Chatillon, B. Sundman, J. Nucl. Mater. 378 (2008) 257.
12. M. Kato, K. Morimoto, H. Sugata, K. Konashi, M. Kashimura, T. Abe, J. Alloys Compd. 452 (2008) 48.
13. M. Kato, K. Morimoto, S. Nakamichi, H. Sugata, K. Konashi, M. Kashimura, T. Abe, The Effect of Oxygen-to-Metal Ratio on Melting Temperature of Uranium and Plutonium Mixed Oxide Fuel for Fast Reactor, Trans. Atom. Ener. Soc. Japan, 7, 4, (2008) 420 (in Japanese).
14. M. Kato, Melting Temperatures of Oxide Fuel for Fast Reactor, Proceedings of ICAPP '09 Tokyo, Japan, May 10-14, 2009, Paper 9451.
15. P. Martin, S. Grandjean, M. Ripert, M. Freyss, P. Blanc, T. Petit, J. Nucl. Mater. 320 (2003) 138.
16. E. L. Gardner, T. L. Markin, R. S. Street, J. Inorg. Nucl. Chem. 27 (1965) 541.
17. H. Shi, M. Chu, P. Zhang, J. Nucl. Mater. 400 (2010) 151.

18. Joint Committee for Guides in Metrology, Evaluation of measurement data – Guide to the expression of uncertainty in measurement, JCGM 100:2008, corrected version 2010.
19. M. Welland, B. J. Lewis, W.T. Thompson 376 (2008) 229-239.
20. T. D. Chikalla, C. E. McNeilly, R. E. Skavdahl, J. Nucl. Mater. 12 (2) (1964) 131.
21. J. C. Boivineau, J. Nucl. Mater. 60 (1976) 31.
22. C. Sari, U. Benedict, H. Blank, Thermodynamics of Nuclear Materials, 1967, IAEA, Vienna (1968), 587–611.
23. E. R. Gardner, T. L. Markin, R. S. Street, J. Inorg. Nucl. Chem. 27 (1965) 541.
24. T. Besmann, J. Nucl. Mater. 144 (1987) 141.
25. D. R. Messier, J. Am. Ceram. Soc. 51 (12) (1968) 710.
26. R. W. Ohse, C. Ciani, Thermodynamics of Nuclear Materials, 1967, IAEA, Vienna (1968), 545–557.
27. L. E. Russel, Plutonium 1960, E. Grison, W. B. H. Lord, R. D. Fowler (Eds.), Cleaver-Hume, London, 1961, 489–492.
28. N. N. Greenwood and A. Earnshaw, "*Chemistry of the Elements*", Pergamon Press, Cambridge (UK) 1994, 327-329.
29. R. E. Latta and R. E. Fryxell, J. Nucl. Mater. 35 (1970) 195
30. T. D. Chikalla, C. E. McNeilly, J. L. Bates and J. J. Rasmussen in : "Int. Colloquim on Study of Crystal Transformations at High Temperatures above 2000 K", Odeillo, FRANCE, 1971 (CNRS 75, Paris, 1972), 351.
31. K. Richter, C. Sari, J. Nucl. Mater. 148 (3) (1987) 266.

Chapter 4: Experimental Study of the Melting Behaviour of Carbide Nuclear Fuels

Uranium-plutonium carbides are one of the candidates for generation IV nuclear power systems, particularly for the gas-cooled fast reactor (GFR) and the very high temperature reactor (VHTR)[1]. Detailed description of these fuels is given in chapter 1. The fuel maximum operational temperature in the GFR and VHTR is between 1300 and 1500 K, but even higher temperatures can be produced under accidental conditions. Experimental data are therefore important to model the high-temperature behaviour of these new fuels.

In this framework, the binary systems uranium-carbon and plutonium-carbon are the starting points to study the ternary uranium-plutonium-carbon and other more complex fuel systems. These materials are pyrophoric and oxidise easily increasing the experimental difficulties at high temperatures. Series of preliminary measurements were performed on uranium-carbon samples to demonstrate the feasibility of the laser technique on this kind of materials. Thereafter, it was possible to perform more complete investigations in the U-C as well as in the Pu-C system. The following sections present these studies.

1 The uranium carbon phase diagram

A general description of the uranium carbon phase diagram is given in Chapter 1. Here more details are discussed concerning the high temperature domain. This is displayed in Figure 1 with the melting temperature values reported in the open literature prior to the current research. The main part of the experimental data are from the 60-70s and the reported values show significant scatter. The melting points of UC and UC_2 are reported to be between 2553 and 2973 K [2,3] and between 2713 and 2803 K [4,5] respectively (Table 1).

Carbide	T_m (K)							
UC	2763±40	2533±50	2973	2663	283	2768±30	2863	-
	2798	-	-	-	2833	2798	-	-
	2833±50	-	-	-	-	2788	-	-
UC_2	2753	-	-	-	2803	2753	-	2713±40
Ref.	6	2	3	7	5	8	9	4

Table 1: Reported value of UC and UC_2 melting temperature, T_m

Variations in the experimental values may arise, for example, from oxygen or nitrogen contamination[5,10] or volatilisation during melting[4]. Storms[6] also mentions that the very low temperature reported by Wilson[11] (not reported in table 1) was probably due to W contamination. Previous measurements of the solidus and liquidus were made using traditional furnace heating methods. Mallett et al.[7] measured solidus and liquidus temperatures of samples between UC and UC_2 prepared using argon arc melting. A sample where a shape similar to a ridge or peak could be distinguished was placed on a graphite ring and heated under vacuum in a furnace. The temperature at which the "ridge" or "peak" rounded was recorded as the solidus, and the temperature at which the sample lost shape and fell through the ring, as the liquidus. Authors have often referred to the work made by Benz et al.[4] to draw the uranium carbon phase diagram because of the particular attention given by these authors to the characterisations before and after heat treatments. They determined the solidus by induction heating of samples up to melting. The samples were prepared by cold pressing and sintering different ratios of pre-prepared uranium carbides under vacuum, to form a cylindrical shape, into which a small hole (blackbody) was made in the top surface. The sample was slowly heated using an induction furnace under a helium atmosphere until liquid was observed in the hole. At this point the temperature for the solidus was recorded, using an optical pyrometer focused on the hole. Since the work of Benz et al., no new experimental data have been added to the U-C phase diagram, until 2009, when the first results of the current laser heating study were published[12]. The data of Chevalier and Fischer refer to a review work[8].

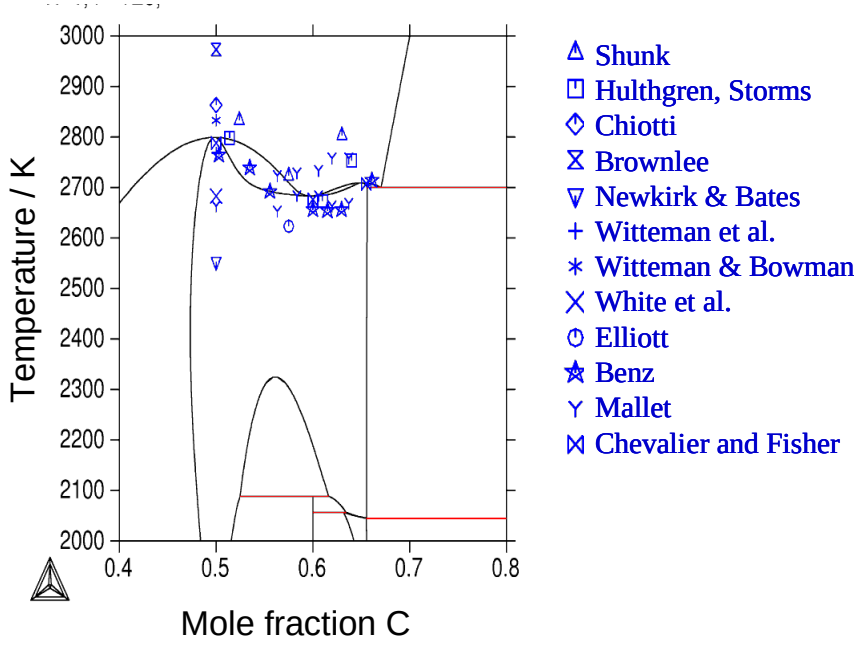


Figure 1: Zoom of calculated U-C phase diagram, between C/U 0.4 to 0.8, showing selected literature data on the solidus-liquidus region.

1.1 Experimental methods

a) Sample preparation

Eleven samples with C/U varying from 0.8 to 2.1 were prepared with an argon arc melting furnace, available at ITU in the Actinide Research Unit. To this purpose a uranium metal ball was cleaned by electrolysis before being combined with graphite splinters in the appropriate ratio. High vacuum (from 10^{-5} to 10^{-6} mbar) and pure argon purging were performed at least two times to remove the oxygen from the furnace. A visual test was performed prior to the preparation of each sample by melting a ball of zirconium. When traces of oxygen were still present in the arc furnace, an easily visible change of colour from grey to blue occurred in the Zr specimen. After positive conclusion from this test, the uranium was melted carefully until the totality of the graphite had diffused inside. The "button" thus obtained was re-melted a few times to ensure a good homogeneity. The drop-shaped sample was then cut with an ISOCUT® diamond saw in a few disks about 1 mm thick and around 10 mm in diameter (figure 2). The biggest disks were used for the laser melting experiments and the others for characterization.

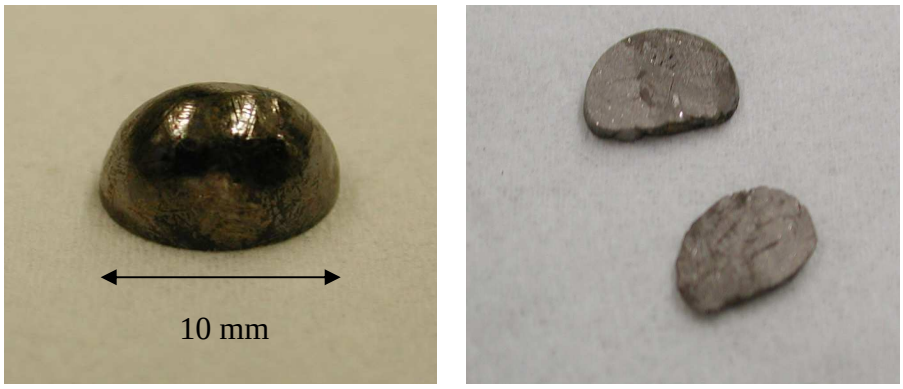


Figure 2: An arc-melted uranium carbide button cut in pieces.

b) Sample composition analysis

Under the current conditions, it is reasonable to consider that these uranium carbide samples did not contain any element other than uranium, carbon and impurities of oxygen. Other minor impurities, like for example nitrogen and sulphur, were detected only in traces. Under this hypothesis, only oxygen and carbon analyses were necessary to determine the C/U ratio, as uranium content can then be obtained by the difference to the total sample weight. These analyses were performed with the fusion extraction – infrared determination (referred to as ELTRA ®), as described in Chapter 2. The results are shown in table 2. The relative uncertainty on the C/U ratio is about 2%. This confirms that it is possible to prepare by arc melting uranium carbon specimens with the desired C/U ratio since these value differ in general by not more than 0.02 (in the worst cases) from the intended one. Moreover, it can be appreciated that the set of precautions taken has efficiently limited the oxidation of the samples, only one measured oxygen mass fraction was higher than 1000 ppm.

C / U	Relative uncertainty (%)	C (mass fraction (%)) / rel. uncertainty (%)	O ppm / rel. uncertainty (%)
0.8	X	X	X
1.02	2	4.87 / 3	1650 / 10
1.27	2	6.035 / 2	40 / 60
1.39	2	6.56 / 2	37 / 60
1.48	2	X	40 / X
1.54	2	7.197 / 2	280 / X
1.65	2	7.69 / 2	21 / 60
1.70	2	7.88 / 2	154 / 60
1.88	3	8.644 / 3	65 / 25
2.02	2	X	50 / X
2.06	2	9.43 / 2	640 / 80

Table2: Analysis of the sample compositions.

These analyses were combined with X-Ray diffraction (XRD). Even when the samples appeared slightly oxidised, the diffractograms never showed the presence of any phase other than those expected. Three distinctive cases were obtained (figure 3):

- Observation of the pure UC phase

It corresponds to a face centred cubic structure isotropic with NaCl. Diffractograms showing only the UC structure are observed for $C/U \leq 1$.

- Observation of a mixture of UC + UC_2

From the ratio C/U = 1.3 to 1.7, all diffractograms show a mixture of UC (with the NaCl structure) + UC_{2-x} (with the tetragonal structure).

- Observation of UC_2 + graphite

From the ratio C/U = 1.8 to 2.1, diffractograms correspond to UC_{2-x} with a tetragonal structure. For $C/U \geq 2$ graphite traces are also visible.

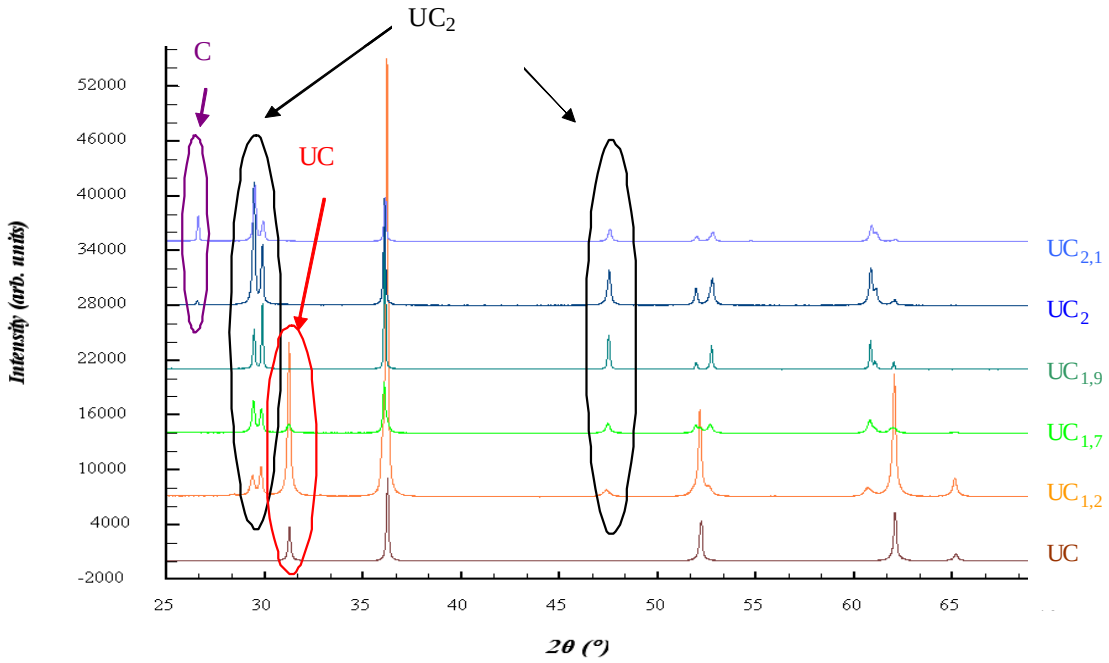


Figure 3: X-Ray diffractograms of 6 different compositions of uranium carbide samples.

According to the equilibrium phase diagram, this mixture of UC + UC_2 should not have been obtained at room temperature, but rather a mixture of UC + U_2C_3 or U_2C_3 + C. This point was extensively discussed by J. Laugier[19] who proposed a metastable phase diagram where the UC_2 phase is present at room temperature (figure 4). Obviously, U_2C_3 cannot be formed because the decomposition kinetics of UC_2 into U_2C_3 + C is extremely slow and this reaction must be initiated by high vacuum and/or mechanical stresses. The measurements of melting point are not impacted by this observation, however the solid-solid phase transition observed at lower temperature must be interpreted in the light of this metastable phase diagram.

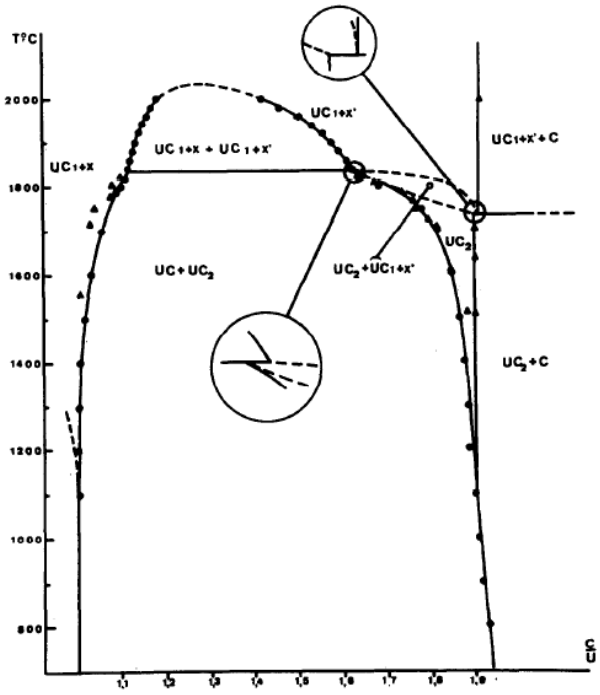


Figure 4: Metastable phase diagram determined by J. Laugier et al.. It shows the existence of cubic UC and tetragonal UC_2 at room temperature, in equilibrium with graphite.

The corresponding XRD cell parameters are calculated for each composition and compared to literature. UC (C/U = 1.02) has a NaCl structure, its lattice parameter being a = 4.959 (1) Å, UC_2 (C/U = 1.88) is observed only in the tetragonal structure, type CaC_2 with the lattice parameter a = 3.525 (1) Å and c = 5.994 (1) Å. In spite of the number of studies performed on this subject, uncertainties remain in these values. Literature values of the lattice parameter vary from a = 4.9544 (3) Å[20] to a = 4.962 Å[21,22] for UC and from a = 3.509 (3) Å, c = 5.980 (5) Å[23] to a = 3.633 Å, c = 6.036 Å[24] for α-UC_2. These characterisations are performed on quenched samples. Both compounds can be hyper- or hypo-stoichiometric and thus the lattice parameters depend on the quantity of carbon vacancies or C2 group frozen during the quenching. Moreover, oxygen and nitrogen are easily soluble in both UC and UC_2. Thus, the UC lattice parameter decreases by addition of oxygen, whereas the effect on the UC_2 parameters is less clear and would require specific studies. Table 3 shows values from literature and those obtained from the different C/U ratios.

Literature					Current research			
UC - space group: F m -3 m(225) Low temperature UC_2 - space group I 4/m m m(139)								
Authors	a_{UC} / Å	Authors	a_{UC2} / Å	c_{UC2} / Å	C/U	a_{UC}/ Å	a_{UC2} / Å	c_{UC2} / Å
23	4.9598(3)	23	3.509(3)	5.980(5)	1.02	4.959(1)		
25	4.961(1)	25	3.524(1)	5.999(1)	1.27	4.957(1)	3.521(1)	5.990(1)
26	4.960	24	3.633	6.036	1.39	4.959(1)	3.525(1)	5.996(1)
20	4.9544(3)	33	3.517(2)	5.987(2)	1.48	4.960(1)	3.525(1)	5.996(1)
27	4.9606(5)	34	3.522(1)	5.988(1)	1.54	4.961(1)	3.522(1)	5.990(1)
13	4.962	35	3.522(8)	5.982(15)	1.65	4.963(1)	3.522(1)	5.993(1)
28	4.958(2)	36	3.524	5.999	1.70	4.959(1)	3.524(1)	5.994(1)
29	4.960	37	3.519	5.971	1.88	4.959(1)	3.525(1)	5.994(1)
30	4.960				2.02		3.520(1)	5.981(1)
21	4.962				2.06		3.521(1)	5.988(1)
22	4.962							
31	4.961(1)							
32	4.955							

Table 3: Cell parameters from literature and current research.

As shown in this work, the β-UC_2 structure, existing at temperatures higher than 2050 K, cannot be quenched because of the extremely fast diffusionless reaction which occurs during the transformation to α-UC_2. This point is discussed more in details later. Bowman et al.[24] performed high temperature neutron diffraction and showed that β-UC_2 has a KCN structure, with lattice parameter a = 5.488 Å at 2173 K, fully miscible with the UC structure.

However, Storm[6] proposed that when the quenching rate is sufficiently rapid, the UC lattice can retain most of the carbon vacancies and part of the C2 group. Consequently, even if the high temperature β-UC_2 modification is not quenched, the low-temperature dependence of the lattice parameter on crystal defects is believed to be similar to the high-temperature one. Figure 5 shows the cell parameters calculated from XRD analyses. The two samples, C/U = 1.2 and 1.8 are not reported in table 2 because no melting temperature could be measured for them. The cell parameters between C/U = 1.3 and 1.7, increase linearly. This tendency seems to correspond to Vegard's law. However, these points fitted with a linear equation give a trend whose extrapolation to C/U = 2 yields to a_{UC2} = 4.967 Å. This does not

correspond to the cell parameter of β-UC_2 determined by Bowman. Hence, it seems that whereas α-UC_2 is easily formed even upon rapid cooling, the UC_{1+x} structure is partially quenched from high temperature through the two phase domain below the peritectoid. The actual composition of this UC_{1+x} quenched phase, not determined in this work, is consequently shifted towards C/U = 1, without reaching the exact UC stoichiometry. Many explanations are possible for this phenomenon, based for example on segregations, concentration of quenched vacancies etc. This subject will be deepened in future research involving also Raman analysis.

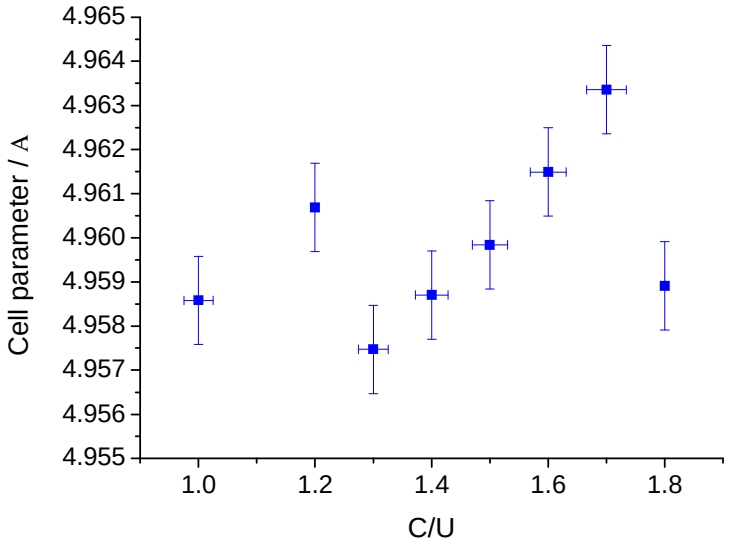


Figure 5: cell parameter of the UC_{1+x} quenched phase.

c) High temperature measurements via laser heating

In general, two to three disks were available per composition. A 3 mm laser spot diameter was sufficient to obtain a molten area big enough to have meaningful results. Uranium carbide samples displayed a good mechanical resistance towards laser irradiation, it was therefore often possible to shoot on different spots of the same sample without destroying it (figures 6 a and b). First tests were performed under primary vacuum but in some cases a black ring was observed around the molten area witch could be due to oxidation during testing. Moreover slight traces of evaporation could also be observed on the colder parts of the sample and on the protective window. To reduce both these effects the whole experiments were performed under a 1.5 to 3 bar Ar pressure. The molten part of the sample remained

shiny and slight traces of evaporation were observable only after a large number of heating cycles.

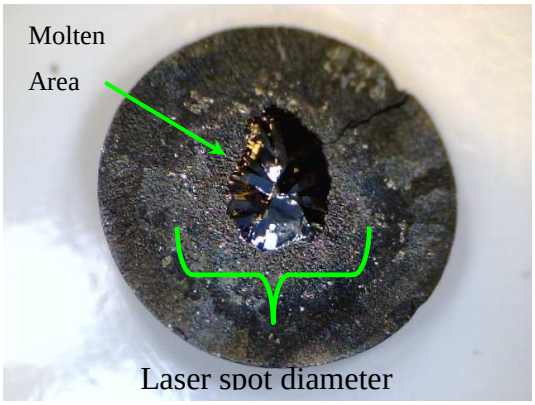


Figure 6 a: C/U = 0.8, because of the small diameter, this sample could be melted in one position only.

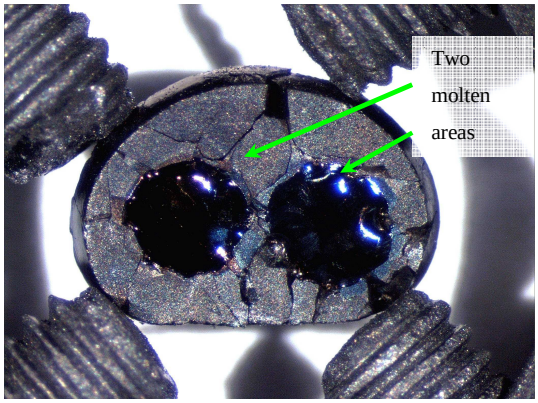


Figure 6 b: C/U = 1.5, here laser heating was performed on two different positions. Some cracks are created because of the thermal stresses.

Cracks often appeared in the laser-heated samples due to thermal stresses, and part of the surface could also fall into pieces during the cooling. These phenomena can lead to peculiar features on the thermograms which are not always easily understandable. The surface state was therefore optically controlled before and after each single experiment. Characterizations with SEM were also performed on the molten area and, when possible, this part of the sample was detached from the bulk for X-ray diffraction analyses. The screws or the high-temperature glue which maintained the sample were also regularly inspected to ensure that no degradation or reactions with the sample occurred during heating.

The quality of the thermogram is strongly dependent on the pyrometers alignment. As explained in Chapter 2, when the pyrometer is not perfectly aligned in the centre of the molten area, the recorded signal can be affected by the presence of thermal gradients, and its interpretation can be difficult. Because of the small laser spot used for this study the molten area diameter was also relatively small (about 3 mm). A preliminary laser shot was used to brand the sample surface in order to ease the alignment of the pyrometers on the right position for subsequent shots.

The heating laser power vs. time profile is the parameter which principally influences the thermogram shape. As described in the previous chapters, a fine tuning of these

parameters permits to reach the sample melting temperature and produce enough liquid to observe a well defined thermal arrest upon freezing. In order to avoid excessive thermal shocks and a sudden projection of molten droplets onto the windows of the pressure vessel, the laser pulse should not reach the maximum power too quickly. For this reason, the initially used square laser pulses were replaced by trapezoidal profiles. Experiments were performed with different laser pulses, and it was observed that a longer pulse at lower power favoured a longer plateau and a faster pulse at higher temperature led to a sharper plateau (more horizontal), probably as a consequence of the reduction of thermal gradients across the laser-irradiated zone in this latter case. Inflections could also be observed during the heating stage of a thermogram but they were not reproducible due to the experimental conditions at this point. Thus all phase transition temperatures have been determined during cooling, whereas the heating stage provides useful information only when the Reflected Light Signal (RLS) analysis can be performed, or for specific emissivity studies.

1.2 High temperature behavior of uranium carbides

a) Multi-channel pyrometry measurements of uranium carbides

Thermograms of uranium carbides have been measured in this research project at many wavelengths, in the ultraviolet (UV), visible (VIS) and near infrared (NIR) spectral ranges, making use of the methods depicted in chapter 2. In particular, several compositions with $1 \leq C/U \leq 2$ have been measured in the VIS and NIR domain, whereas only UC and UC_2 were investigated in the UV. This research has allowed obtaining a wavelength-dependence of the sample spectral emissivity for uranium monocarbide. In addition, the high temperature emissivity behaviour of UC_2 has been critically assessed. For this latter compound, spectral emissivity had been investigated only up to 2240 K[38].

a.1) Uranium Monocarbide

The spectral emissivity of uranium monocarbide was studied by De Coninck et al[38,39] and by Bober[40] et al. by direct spectral reflectivity measurements. Bober et al., in particular, obtained accurate results on the spectral emissivity of solid and liquid UC between room

temperature and 4200 K, results are reported in Figure 7. In the same work, also the melting temperature was reported as (2780 ± 30) K. Bober et al. performed direct measurements of the spectral emissivity, whereas in the current work this parameter has only been obtained from a numerical fit of the radiance measured at different wavelengths. For this reason, it seems reasonable to take the results of Bober et al. as a reference for the present evaluation of UC. On the other hand, the current investigation will permit to complete the previous one by yielding a wavelength dependence of the spectral emissivity for solid and liquid UC. It should be born in mind, however, that Bober et al. performed their measurements on UC samples with a high content of O_2 impurity (3500 ppm), and this important uncertainty source can hardly be evaluated in the present study.

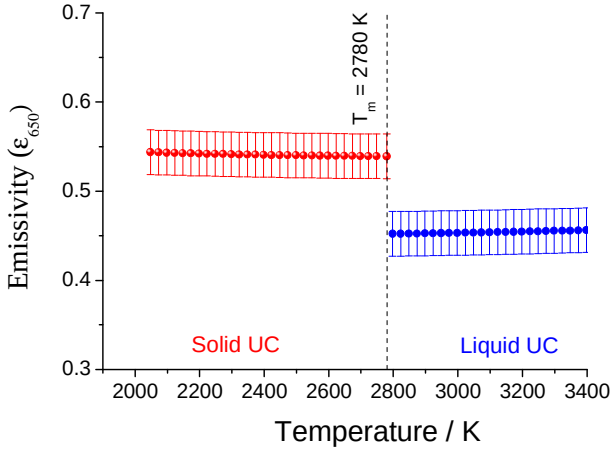


Figure 7: Normal spectral emissivity (ε) explain at 650 nm of UC (+3500 ppm O2) measured by Bober et al.[40].

In order to produce results comparable to Bober's, a full multi-wavelength pyrometry investigation was performed on a 4000 ppm O_2 – containing UC sample. VIS-IR and UV pyrometry investigations were performed using the techniques described in chapter 2.

Experimental thermal radiance (Planck curves) were fitted with Planck-like functions (with the absolute temperature as a free parameter), multiplied by the Taylor expansion of the emissivity assumed to be a continuous function of the wavelength:

$$\varepsilon(\lambda) \cong \sum_{i=0}^{n} a_i \lambda^i \qquad (1)$$

The summation was generally extended to n = 2, but results were already acceptable in the grey body approximation, and numerical instability arises whenever the summation is

extended to too many terms. Moreover, Taylor expansion is a fist-approach method to take into account emissivity as a function of wavelength. The values obtained in all the investigated composition range fall in a large uncertainty band $\varepsilon_{650} = 0.45 \pm 0.07$, for both solid and liquid UC_x. The main reason for the large uncertainty is to be sought in the numerical instability of the regression. A discontinuity between the emissivity of solid and the emissivity of liquid, in agreement with results of Bober et al.[40], was observed in many cases. However, the gap between the solid and the liquid values was often smaller than the measurement uncertainty. The same method was used as an inverse one to obtain the emissivity of solid and liquid UC at a known temperature. This could be realized at the melting point of stoichiometric UC, which was established to be (2780 ± 30) K based on the work of Bober et al. and confirmed in more recent data reviews[8]. This was imposed to be the temperature of the two thermal arrests (melting and freezing) of figure 8.

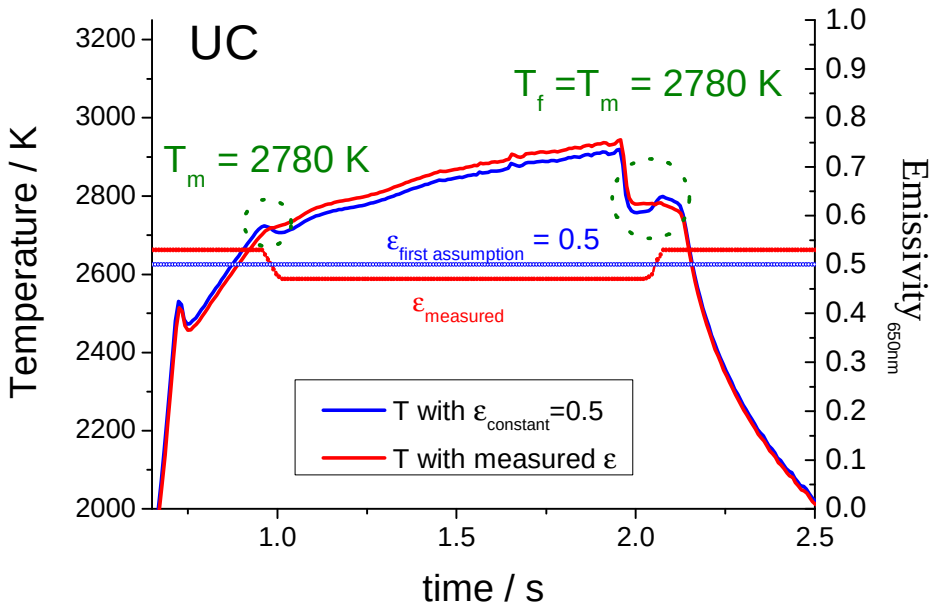


Figure 8: Measurement of the UC emissivity

One can observe that on melting the thermal arrest is followed by an apparent temperature decrease, while on freezing the opposite effect is observed (blue thermogram-corresponding to constant emissivity = 0.5). This phenomenon can be explained on the basis of an emissivity decrease upon formation of liquid[(3)]. Thermal radiance spectra were recorded

[(3)] Since the same effect occurs both on melting and freezing, it cannot be related to supercooling of the liquid. Supercooling of the liquid is normally ruled out by suitably setting the laser heating parameters

at several points during the melting and freezing arrests. Using the approach explained in chapter 2, calling $S_i(\lambda)$ each of these spectra, and P (2780) the Planck function at 2780 K, the sample normal spectral emissivity for each experimental spectrum *i* is given by definition by

$$\varepsilon_i(\lambda) = \frac{S_i(\lambda,2780)}{P(\lambda,2780)} \qquad (2).$$

Emissivity values are thus obtained in the investigated wavelength range (0.550 µm ≤ λ ≤ 0.900 µm) for each of the experimental spectra recorded during the melting and freezing arrests. Twelve spectra were recorded on melting and twelve on freezing. The spectra taken on the maximum recalescence in both cases were considered as corresponding to the solid, whereas those taken at the minimum temperature during the phase transition were attributed to the liquid. Spectra in between were considered as a mixture of the two. Results of emissivity as a function of wavelength for solid and liquid UC are shown in figure 9.

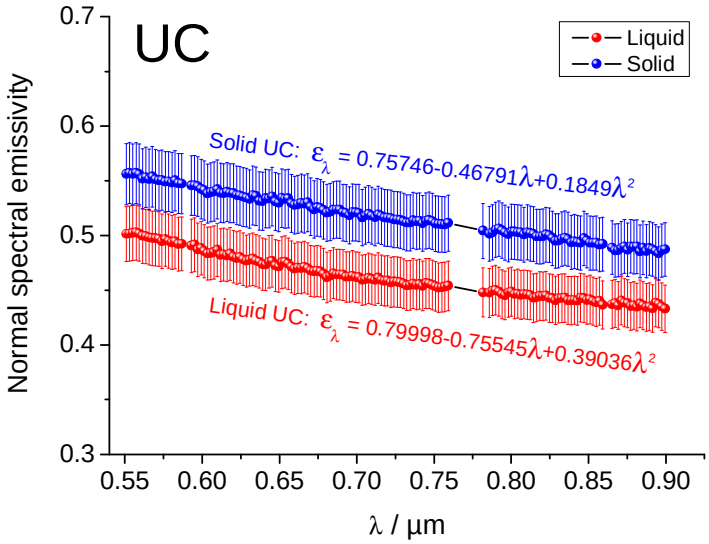


Figure 9: Emissivity as function of λ in liquid and solid phases

The resulting emissivity trends are:

Solid UC: $\varepsilon_\lambda = 0.75746-0.46791\cdot\lambda+0.1849\cdot\lambda^2$ (3)

Liquid UC: $\varepsilon_\lambda = 0.79998-0.75545\cdot\lambda+0.39036\cdot\lambda^2$ (4)

Uncertainty bands in Figure 9 are given by the composition (according to the uncorrelated error propagation law) of the uncertainty on the melting temperature of UC (± 30 K) and the dispersion on the current experimental emissivity data. Within these uncertainty bands, the

reported emissivity trends have been checked, by fitting radiance spectra at different temperatures, to be valid also for solid UC at $T < T_M$ and for liquid UC at $T > T_M$. One can notice that:

1. The gap between the emissivities of solid and liquid UC is confirmed in the investigated spectral range. This gap slightly tends to increase with increasing λ.

2. The spectral emissivity of both solid and liquid UC decreases with increasing wavelength, as expected for a metallic material in the VIS-UV range.

3. The spectral emissivity values at 0.65 µm are 0.53 for solid UC and 0.47 for liquid UC.

The latter values are used in order to correct the signal of the fast pyrometer used to record thermograms in the current study. It should be noted, however, that the effect of the gap between solid and liquid emissivity was regularly observed only for samples with a high content of oxygen impurities (> 2000 ppm). The question remains therefore open, on whether the oxygen content has an impact on the lower emissivity of liquid. A more accurate analysis of the solid surface roughness effect on radiance might also lead to a better comprehension of the observed behaviour. The melting temperature observed for samples with lower oxygen contents are still consistent, at 0.65 µm, with $\varepsilon_{650} = 0.53$ and $T_M = (2780 \pm 30)$ K. One can observe that in the red curves of figure 8, the emissivity variation between solid and liquid (using the 0.650 µm values indicated above) compensate almost perfectly the inflections corresponding to the melting and freezing arrests, and it flattens them as a result. However, given the still large uncertainties on the measured emissivity, this effect has not been included in the calculation of the error bands on the phase diagram experimental points.

In order to complete and corroborate the presented results, the melting temperature of UC could be measured also by making use of UV pyrometry, using the technique under development presented in Chapter 2. The resulting thermogram measured at 0.215 µm is reported in Figure 10.

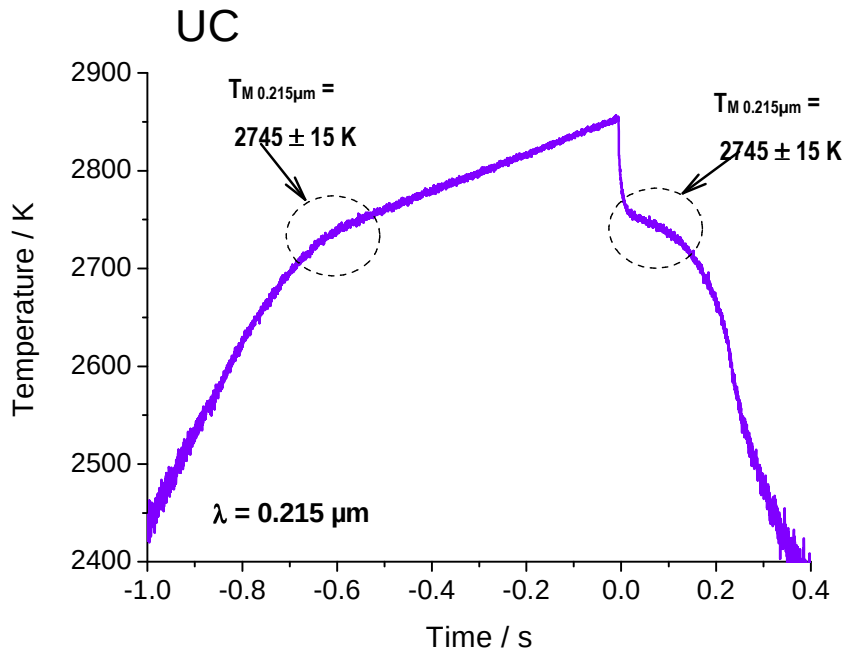


Figure 10: Thermogram in radiance temperature recorded on a UC sample (3500 ppm O_2) at 0.215 µm.

It should be noted that the radiance gap is not visible in this case upon melting and freezing. This can be ascribed to two possible causes. First, the focal spot of the UV-pyrometer is much larger than the focal spot of the VIS – IR ones. Therefore, the observed signal is an average on a wider region, where thermal gradients and possible temperature jumps are smoothed. Second, if the trends for the emissivity of solid and liquid UC reported in figure 9 are extrapolated to 0.215 µm, one can observe that the emissivity gap tends to vanish in the ultra-violet range. In particular, at 0.215 µm the emissivity for solid UC would be $\varepsilon_{SOLID\ 215}$= 0.68, and the emissivity for liquid UC $\varepsilon_{LIQUID\ 215}$= 0.66. Under this assumption, the radiance gap corresponding to the emissivity variation would be of approximately 1.5 K, i.e. much smaller than the measurement intrinsic uncertainty. For these reasons, it is not a surprise that the radiance gap clearly observed in the visible range could not be noticed in the ultraviolet.

Since the reported radiance melting/freezing temperature at 0.215 µm is a lower bound for the real temperature (which will be higher, the lower is the emissivity), the measured value of (2745 ± 15) K can be considered as being in agreement with the value of the true melting temperature, (2780 ± 15) K, established with the measurements in the visible range as explained below.

The value at 0.215 µm of the spectral emissivity corresponding to a true temperature of 2780 K can be easily obtained from equation (8) in chapter 2, solved for ε_λ. By substituting the current UV values for λ and T_λ one obtains $\varepsilon_{215} = 0.736$. This value is slightly higher than the one extrapolated from the VIS/NIR analysis, still well within the experimental uncertainty. In fact, one should not forget that due to the low sensitivity to emissivity changes (cf. Chapter 2), UV pyrometry is much better suited for the measurement of temperature than it is for the estimation of emissivity once the true temperature is known. Nonetheless the usefulness of this further temperature measurement at shorter wavelength can be seen from the diagram in figure 11. Here the inverse solidification radiance temperatures measured on the UC sample are plotted as a function of the pyrometer wavelength and fitted both with linear regression (dotted line) and with the function in equation (3) above, obtained by imposing the value 2780 K to the true melting temperature.

It can be seen that, while in the VIS/IR range the two approaches give equally good fits, in the UV a discrepancy between the linear fit and the experimental data is evident. The apparently little numerical discrepancy (2766 K at 0.215 µm for the linear extrapolation *vs*. 2745 K experimentally measured) is not negligible when the little sensitivity of the radiance intensity in the UV is taken into account. Moreover, the extrapolated solidification temperature at zero-wavelength (T_0) give a clearly too high value (2873 K). This shows that the method called "linear extrapolation to zero wavelength" can be very approximate when the investigated material has an emissivity dependence on wavelength which consistently deviates from the gray body behaviour. This limitation of the "linear extrapolation to zero wavelength" approach can be well evidenced by enlarging the operational wavelength range of the pyrometers, as it is done here by employing UV pyrometry.

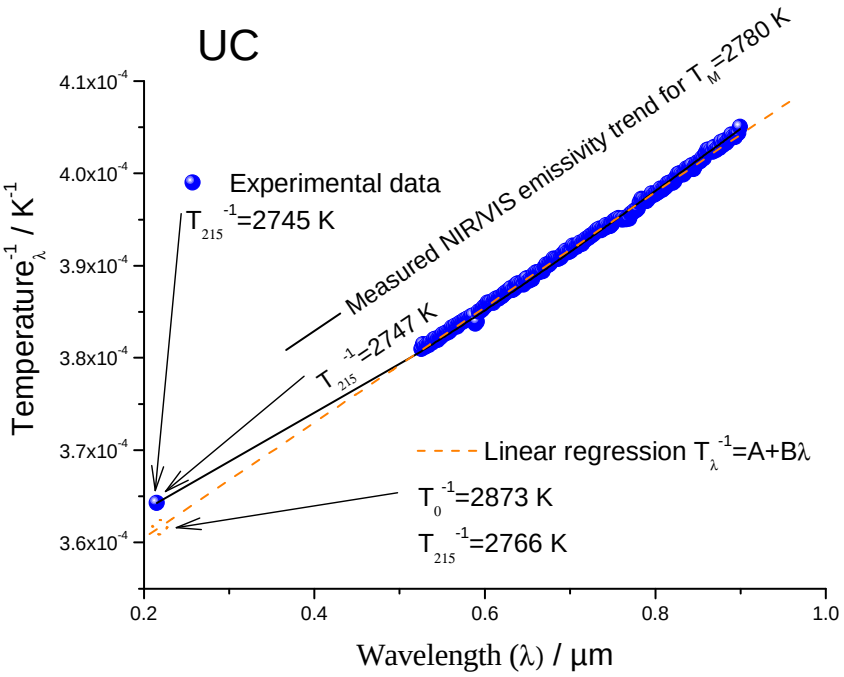


Figure 11: The inverse solidification radiance temperatures measured on a UC sample as a function of the pyrometer wavelength.

In conclusion, the current results on the melting temperature and the spectral emissivity behaviour of UC can be summarized in the following points:

1. The melting point value reported by Bober et al.[40], T_m = (2780 ± 30) K can be confirmed, with the emissivity values recommended by Bober et al. at 0.65 µm.

2. The spectral emissivity ε_λ of solid and liquid UC is dependent on wavelength, according to Equations (3) and (4) valid for melting solid and solidifying liquid respectively. The validity of these trends has been shown to extend, within the reported experimental uncertainty, from the UV region (λ = 0.215 µm) to the near – infrared (λ = 0.9 µm). No significant emissivity changes have been observed, within the limits of the current experimental approach, for liquid at higher temperature and solid at lower temperature.

3. A gap of approximately 0.07 between the emissivity of solid UC and that of liquid UC in the visible range is confirmed. This gap tends to vanish at short wavelengths (in the

UV domain) and increase at increasing wavelengths. However, the emissivity of liquid UC is probably dependent on the oxygen impurity content.

a.2) Uranium Dicarbide

The emissivity analysis for UC_{2-x} is more difficult and challenging than for UC. Essentially, no real reference points exist for this composition above 2240 K, the maximum temperature reached by De Coninck et al. in their experimental investigation based on electron-beam heating and reflectivity analysis[38]. Like in the case of Bober et al. for UC, also De Coninck k et al. performed more direct measurements of spectral emissivity, based on Kirchhof's law. Their results can therefore be taken as a reference for the current investigation. However, as it can be seen in Figure 12, the data of the De Coninck et al. are not well reproducible in different samples, especially above the $\alpha \rightarrow \beta$-UC_2 transition. Whereas an emissivity of approximately 0.525 ± 0.025 can reasonably be assumed for α-UC_2, slightly increasing with temperature, not much can be said for β-UC_2, if not that ε_{650} is probably still close to 0.5 in the vicinity of the $\alpha \rightarrow \beta$ transition. On the other hand, De Coninck et al. also measured the spectral emissivity at 2.3 μm, showing that its value is lower than it is in the visible range. This behaviour is typical of a metallic material, which α-UC_{2-x} has been shown to be both by electrical resistivity measurements[41] and by ab-initio calculations[42]. Although this property has never been directly proven for β-UC_{2-x}, also this phase can reasonably be assumed to behave as a conductor, by analogy with cubic UC (which is essentially the same phase), or with fcc γ-ThC_2[43].

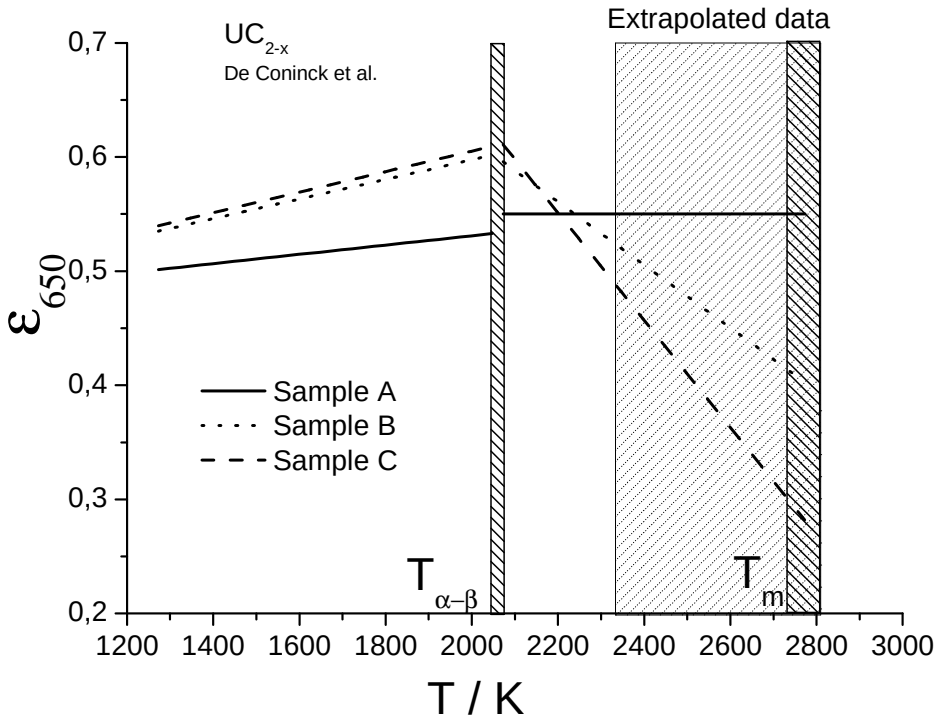


Figure 12: Normal spectral emissivity measurements in α and β-UC_2 by De Coninck et al.[38]. The in α →β-UC_2 transition temperature is reported with an uncertainty band of 30 K around 2055 K. The melting temperature is reported with the uncertainty band obtained in the current research.

Based on this assumption, a metallic behaviour of the spectral normal emissivity can be hypothesized for UC_2, and in particular ε_λ can be assumed to be slightly decreasing with λ. Since this behaviour corresponds to the one established for solid UC, it is natural to assume, as a first approximation, that β-UC_2, which is isostructural to fcc UC, has also a similar spectral emissivity. In order to test this assumption, the thermogram in Figure 13 recorded at 0.65 µm can be taken as a reference. This was recorded on a UC_2 sample containing around 640 ppm of oxygen (see Table 1 above). One can notice the main features of the thermogram: an inflection corresponding to melting, a clear thermal arrest upon freezing and a long thermal arrest corresponding to the β→α transition. The melting inflection was not reproducible upon heating at this wavelength, probably due to parasite reflection of the heating laser beam, and has therefore not been considered in the present analysis. Many-wavelength spectra have been recorded corresponding to each of the blue circles in figure 13. Spectra on the freezing arrest are fitted using Wien's law corrected by equation (3) for the spectral dependence of emissivity. The fit is more conveniently performed on a diagram plotting the inverse radiance

temperatures T_λ *vs* wavelength λ (Figure 14). The resulting curve fits well the experimental data with a real temperature T_M = 2737 K. This temperature is slightly higher than that reported by Benz (2713 K) and the value recommended in recent literature reviews for UC_2 (2700 K)[8], but still within the experimental uncertainty.

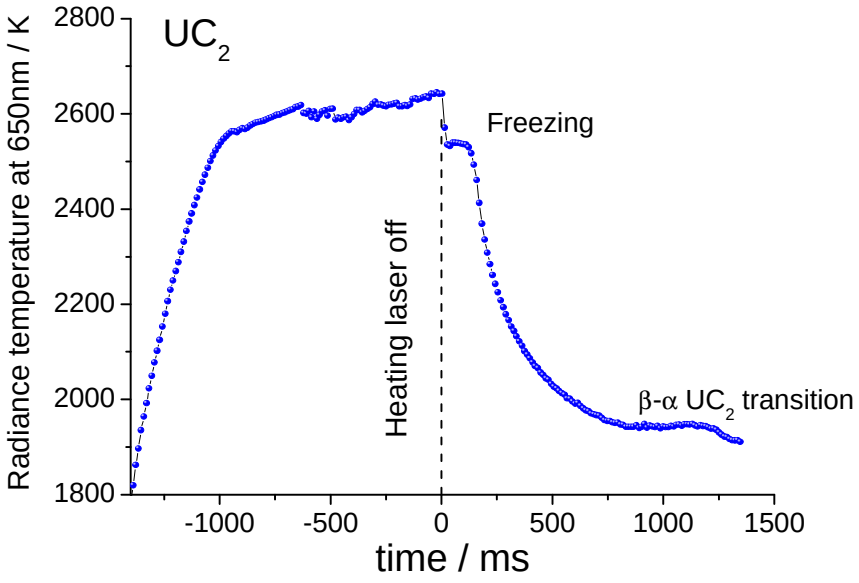


Figure 13: Thermogram recorded at 0.65 µm during a laser heating / cooling cycle on a UC_2 sample.

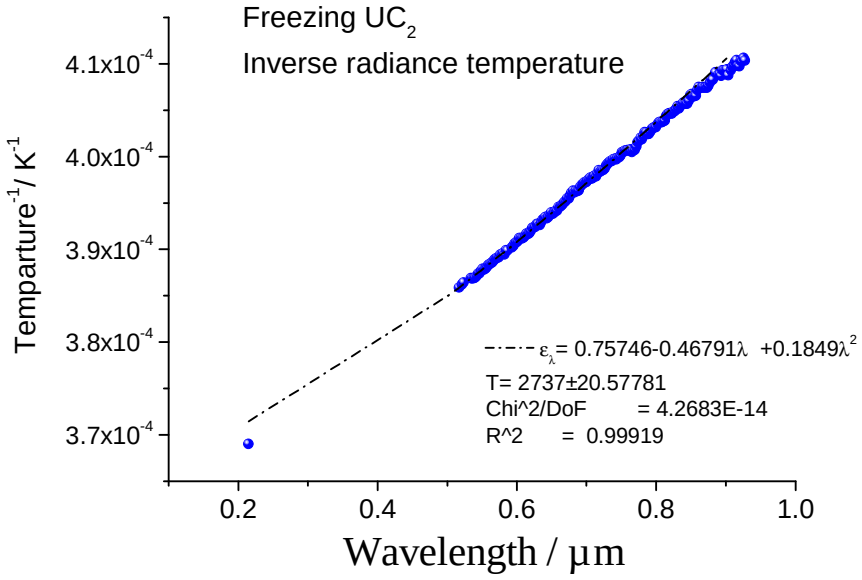


Figure 14: The inverse solidification radiance temperatures measured on a UC_2 sample as a function of the pyrometer wavelength. Data are fitted using the emissivity of solid UC. The agreement is good in the VIS-NIR range, but the emissivity appears to be higher in the UV at 0.215 µm.

The assumption that spectral emissivity behaves as it does in solid UC appears therefore reasonable. In order to check the discrepancy with previous data, however, the freezing point of UC_2 has been measured also by UV pyrometry at 0.215 µm. The resulting thermogram is displayed in Figure 15. The radiance melting temperature of UC_2 is (2710 ± 15) K. Unfortunately, only one UV pyrometry measurement was successful on UC_2, so no real statistics is available for this composition. The reported error indicates only the uncertainty in locating the exact melting / freezing temperature in the thermogram of figure 15. The value, 2710 K, is a lower bound for the real melting point of UC_2, being this a radiance temperature. This point has been added in the diagram of Figure 14, and it can be noticed that it is below the inverse radiance temperature trend extrapolated from the visible range. In fact, if the solidification temperature value obtained in the VIS/IR range using the emissivity of stoichiometric UC is retained (2737 K), the corresponding emissivity at 0.215 µm can be calculated through Equation (5) above, yielding $\varepsilon_{215} = 0.78$. This value is higher than the one predicted by equations (3) and (4) for solid and liquid UC, which should both range, at 0.215 µm, around 0.65. Assuming that this discrepancy is not due to the experimental uncertainty only, one should therefore admit that the spectral emissivity of freezing UC_2 considerably increases in the UV range. This assumption is obviously to be deepened and proven in further research. In conclusion, the value 2737 K can be retained, although with a larger uncertainty than reported for UC.

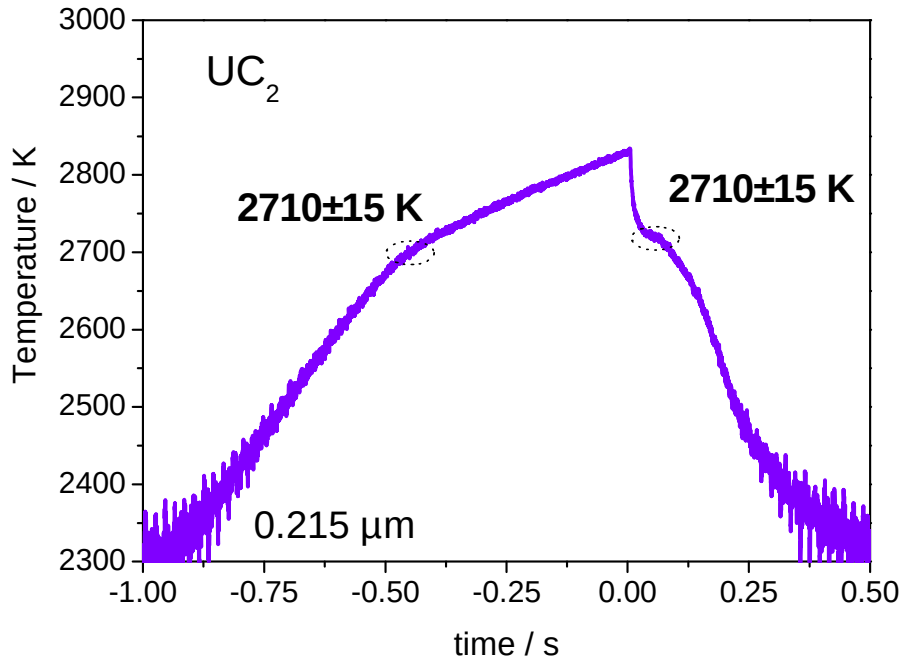


Figure 15: Radiance temperature thermogram recorded on a UC_2 sample (640 ppm O_2) at 0.215 µm.

Another point that can be highlighted is the absence of any evident emissivity change upon melting in UC_2. Unlike the case of UC + 3500 ppm O_2, the slight liquid supercooling upon freezing visible in Figure 13 is not paralleled by any similar temperature gap upon melting, and cannot be attributed to an emissivity change. On the other hand, radiance spectra of supercooled liquid UC_2 are fairly well fitted by using the emissivity of *solid* UC (Equation (3)), and *not* with the expression obtained for *liquid* UC (Equation (4)). One can therefore conclude that in the case of UC_2 with oxygen impurity concentration < 1500 ppm there seem to be no gap between the optical spectral emissivities of solid and liquid. Since such a gap was hardly observed also in low-oxygen contaminated UC samples (see Figure 17 in the following section), it seems reasonable to attribute this gap more to the high oxygen content than to the C/U ratio. This is not necessarily in disagreement with the results of Bober et al. who reported 3500 ppm of oxygen impurities in their UC sample. This hypothesis is confirmed by other similar experiments carried out on other samples with different C/U and oxygen impurity content < 1000 ppm. It should however be noted, that a slight inflection is always visible upon melting, which could be attributed to a minor emissivity discontinuity between solid and liquid, but it can not be observed by the current uncertainty in radiance spectra fitting.

A last interesting point of this study concerns the emissivity of solid fcc β-UC_2 in the proximity of and during the $\beta \rightarrow \alpha$ transition. An additional difficulty in the optical analysis of this transition is that the solid sample surface cannot be rigorously considered as optically smooth (unlike the freezing liquid), and the radiation spectra fitting can therefore be affected by uncontrolled morphological changes and irregular roughness. Nonetheless, figure 16 shows that even spectra of inverse radiance temperature recorded in the UV-VIS-NIR domain during the $\beta \rightarrow \alpha$ UC_2 transition can be reasonably well fitted using formula (3) above, and resulting in a transition temperature of 2059 K, in excellent agreement with literature values. This phase transition could not be detected with UV pyrometry, because its temperature is below the detection limit of our detector. An uncertainty of ±20 K seems reasonably conservative for this value, to take into account the hypothesis on emissivity.

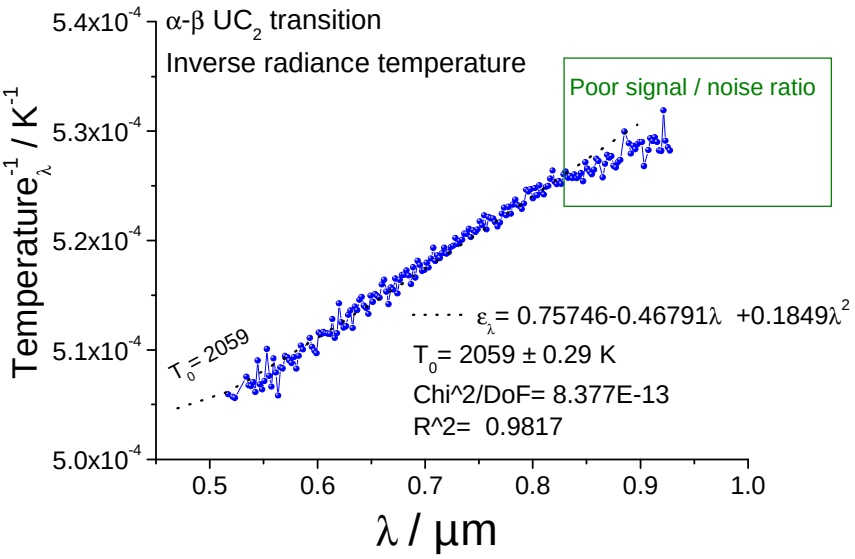


Figure 16: The inverse β→α transition radiance temperatures measured on a UC_2 sample as a function of the pyrometer wavelength. Data are fitted using the emissivity of solid UC.

a.3) Experimental highlights

In conclusion, the results of the current study can be summarized in the following points.

1. The melting temperature of stoichiometric UC is (2780 ± 30) K, and can be taken as a high temperature reference for the U-C system. The error bands take into account a possible oxygen impurity effect.

2. The emissivity of solid UC decreases with increasing wavelength in the UV-VIS NIR domain, as expected for a metallic material.

3. The emissivity of liquid UC appears to be lower than the emissivity of the solid. The gap measured in the VIS-IR range amounts to approximately -15% for a solid emissivity of about 0.53. This gap, measured in a UC sample with 3500 ppm of oxygen impurities, seems to decrease and tends to vanish with decreasing oxygen content and, probably, with increasing C/U ratio.

4. The trend measured for the optical spectral emissivity of solid UC can be reasonably extended to fcc β-UC_2 and to the entire high temperature UC – UC_2 fcc solid solution.

The error induced by this assumption appears to be much smaller than the uncertainty affecting the available literature data.

5. With this assumption on the spectral optical emissivity, the melting point of UC_2 is recommended at (2737 ± 40) K, where the larger uncertainty is related to the lack of experimental data.

6. Within the same assumptions, the $\beta \rightarrow \alpha$ UC_2 transition temperature is recommended to occur at (2056 ± 20) K, where the large relative uncertainty is mostly related to the current assumption on emissivity.

7. The optical spectral emissivity of UC_2 has been observed to considerably increase in the UV spectral range compared with the emissivity of UC, which seems to follow the same trend established in the VIS – NIR domain.

These conclusions will be taken as the starting point for the investigation of several compositions in the U-C system, dealt with in the following section.

b) Investigation of the high temperature phase diagram U-C

All the thermograms reported for the study of the U-C phase diagram, recorded with the 652 nm pyrometer are presented as true temperature vs. time, whereby the true temperature is obtained from the radiance temperature through Wien's formula, equation (8) in chapter 2. Here the value of emissivity at 652 nm is considered to be constant and equal to 0.53, based on the conclusions of the previous section.

Through the different experiments, and for all compositions, pronounced thermal arrests have been observed corresponding to the liquid-solid and solid-solid phase transitions. Plateaus slightly decreasing in temperature, perfectly horizontal or slightly affected by undercooling have been recorded in the different cases. The same method explained in Chapter 3 for the interpretation of thermal arrests in oxide samples has been applied here to the study of carbides, in order to have a consistent exploitation of the thermograms. The comparison of all plateaus from each composition and the RLS has permitted to establish the thermal arrest temperatures case by case, as presented in the following paragraphs.

Figure 17 shows thermograms obtained during the melting of nearly stoichiometric UC (C/U = 1.02 ± 0.02) with 1650 ppm of O_2, using two different laser heating profiles, one high and fast (pulse 1, with maximum power of 1250 W over 20 ms), the other lower but longer (pulse 2, with maximum power of 750 W over 30 ms). In both cases the samples are heated well above the reported melting temperature (2780 K). With pulse 1, the maximum temperature reached is 3500 K and 3150 K using pulse 2. On cooling very clear thermal arrests are observed at 2756 K and 2757 K for pulses 1 and 2 respectively. The noise observed around the highest temperature is believed to be due to viscous movements on the sample surface. By reducing the maximum temperature, this noise is removed, as shown by the thermogram corresponding to pulse 2. The curves obtained do not show further inflections during cooling, indicating that UC freezes congruently and undergoes no phase changes below the melting temperature. No emissivity change upon melting can be deduced from the thermograms recorded on these samples, unlike the case of higher-oxygen containing specimens as the one of figure 8.

A sample with C/U = 0.8 was also investigated, in order to perform at least one check on a hypo-stoichiometric sample. The liquidus temperature of (2712 ± 30) K obtained in this case with the same emissivity accepted for stoichiometric UC is in good agreement with the values reported in the literature. Also a second inflection was detected at much lower temperature (around 1400 K), near the pyrometer detection limits. This certainly corresponded to the solidification point of metallic uranium, in agreement with the phase diagram reported in figure 5 of Chapter 1. The $UC_{0.8}$ was used as a reference in EPMA micrographs, as explained below.

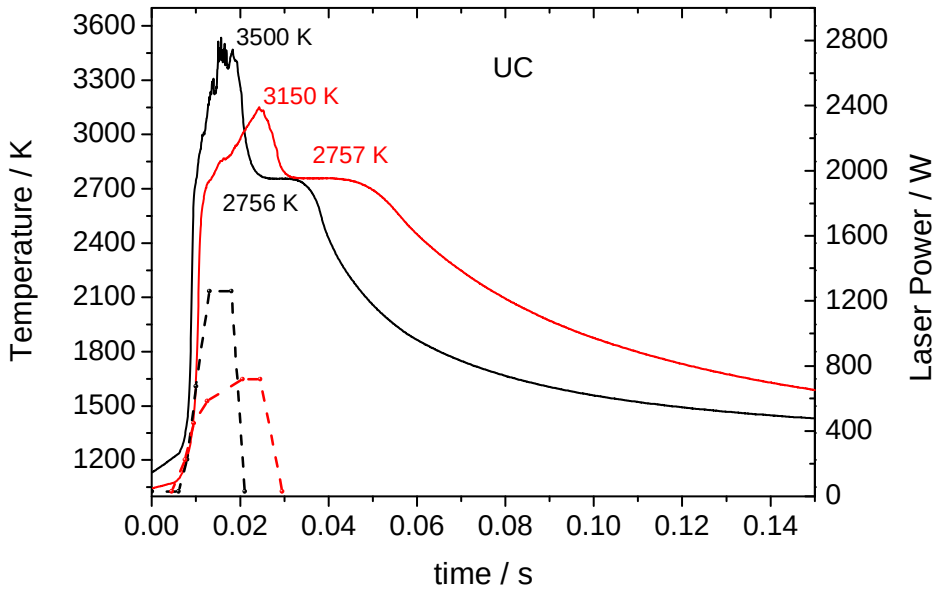


Figure 17: Thermograms obtained on UC with two different laser profiles.

In samples with ratio C/U = 1.3 to 2.1 the phase transitions observed in the thermograms were more complex than the previous ones. The RLS method helped then to distinguish them. Alignment of the Ar^+ laser was realized by maximizing the reflected signal after screening all the parasite reflections. Figure 18 shows the curves obtained during melting/freezing of a specimen with C/U = 1.5. If a distinct liquidus and solidus exist for this and the neighbouring compositions, they are close and not distinguishable in the current experiments. A high-power laser heating profile was applied (1 kW, 40 ms). The maximum temperature reached (3300 K) is well over the expected melting temperature for this sample composition. On cooling a clear thermal arrest is observed at 2656 K and corresponds well to the end of the vibrations in the RLS. Within the experimental uncertainty, this is the lowest solidification point observed in the investigated U-C composition range.

A further inflection is also observed at lower temperature, underlined by the RLS at approximately 2019 K. This second thermal arrest is likely to correspond to a solid-solid transition. It is not observed every time for the compositions varying between C/U = 1.3 and 1.5 and therefore it was not taken into account in the final results. In the worst case, it could correspond to the onset of segregation phenomena during the complex freezing process, leading to the formation of zones richer in C.

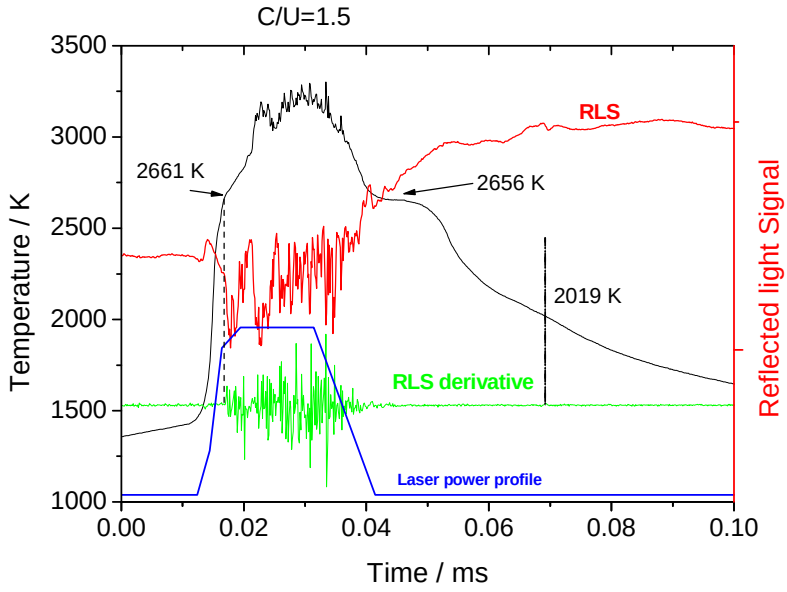
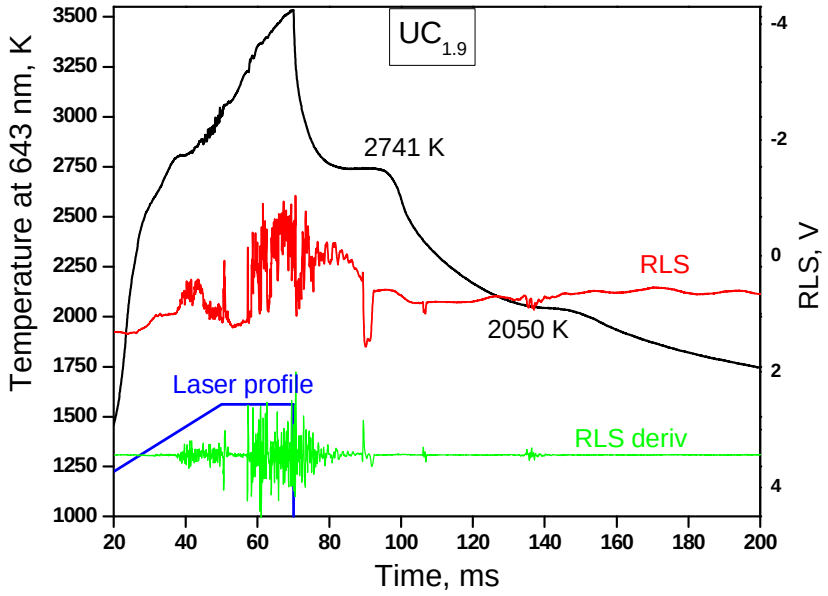


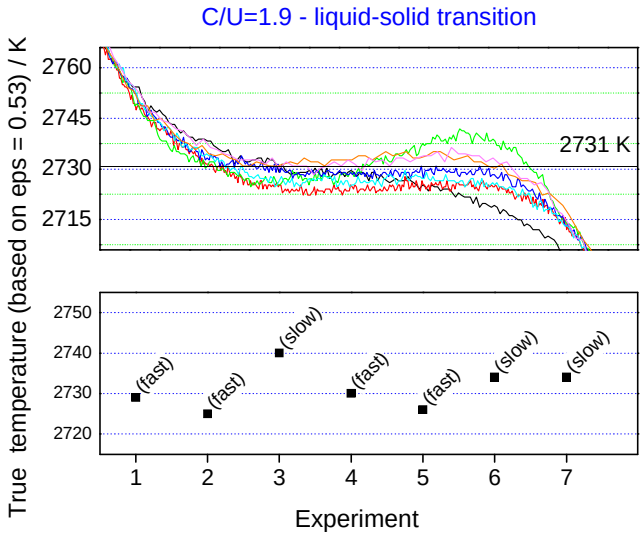
Figure 18: Thermogram obtained on a uranium carbon sample with C/U = 1.5.

As an example of heating cycles on samples with C/U > 1.5, Figures 19 and 20 show the results obtained with a series of seven measurements realised on a C/U = 1.9 sample. The laser pulses duration was modified from hundreds ms to one sec, identified by the labels "fast" and "slow" in figure 20. For the samples with C/U > 1.5, the second thermal arrest is much more pronounced and perfectly identified by the RLS. The really good reproducibility of the two thermal arrests highlights the good chemical and mechanical stability of these samples at high temperatures. Degradation of the sample surface, oxidation or non congruent evaporation would have impacted on the phase transition temperature over successive shots. For C/U ≥ 1.9 the solidification temperature seems to remain constant at different compositions, within the experimental uncertainty. This suggests that the common value of the solidification temperature can correspond to the eutectic temperature for the system UC_2-C. Phase diagram optimization (CALPHAD) of the U-C system shows however that these temperatures could alternatively correspond to the liquidus transition (see figure 23 below). Unfortunately, samples with C/U > 2.1 could not be successfully fabricated with the current method, so a more sound corroboration of this result is left to further research in this field.



.

Figure 19: Thermogram obtained on a uranium carbon sample with C/U = 1.9 and 650 ppm of O_2.



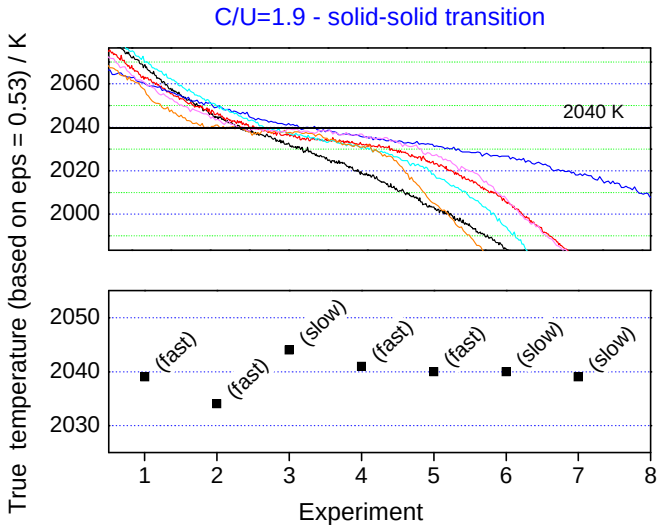


Figure 20: Plateaus of liquid-solid and solid-solid phase transitions obtained during 7 different measurements performed on one uranium carbon sample with C/U = 1.9 and 650 ppm of O_2.

A series of post-heating cycle characterizations was performed to determine without any doubt the origin of the second thermal arrest

The molten part of a sample with C/U=1.9, could be separated from the rest of the specimen and analysed by X-Ray diffraction (XRD). The two diffractograms in figure 21, the first taken on a fresh specimen (red curve) and the second on a molten and refrozen one (blue curve), looked very similar. This rules out the hypothesis that the second observed thermal arrest may correspond to an oxidation in which case additional oxide peaks would have appeared in the XRD.

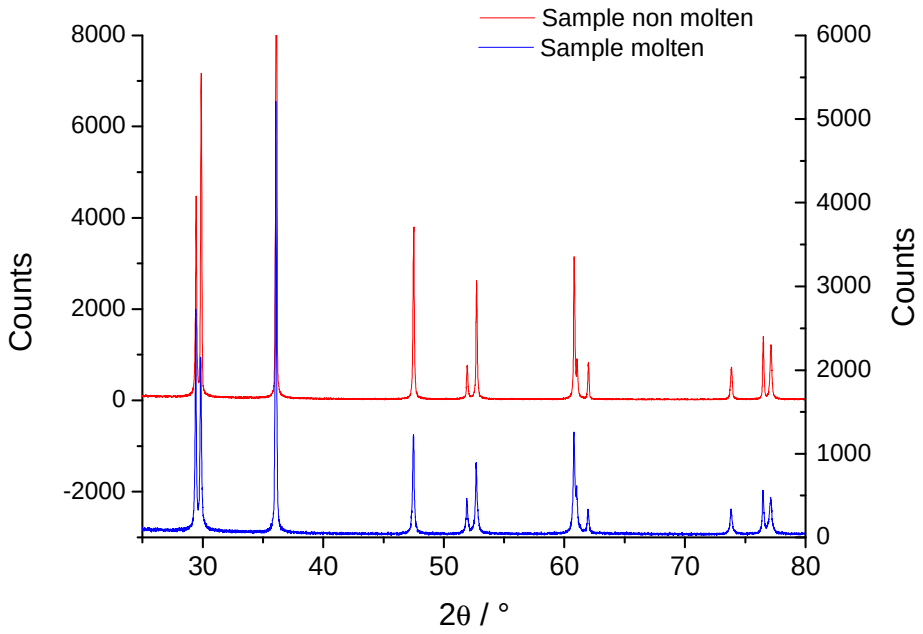


Figure 21: X-ray diffractogram from fresh and melted samples with C/U = 1.9.

As explained before, samples with C/U>1 displayed a mixture of UC and UC_2 phases both after arc-melting preparation and laser heating cycles. It is important to mention again that it was never possible to quench the high temperature structure of UC_{2-x} (β-UC_{2-x}), not even if the sample reached room temperature with very fast cooling rates. This was confirmed by XRD and electron microprobe (EPMA) analyses. As mentioned, XRD clearly showed that the quenched UC_{2-x} phase was tetragonal (α-UC_2), i.e. the low-temperature phase and not the cubic high-temperature phase. EPMA pictures are presented in figures 22 a and b, corresponding to samples with C/U = 0.8 and 1.7 respectively. Figure 22.a shows well formed stoichiometric UC grains with U-metal richer grain boundaries (brighter zones). In this picture, the grain bulk can be taken as a visual reference of stoichiometric UC. Figure 22.b shows that for C/U = 1.7, instead, the UC phase is covered with UC_2 needles in a Widmanstätten structure. These needles were most probably formed by an epitaxial growth of α-UC_2 on UC[41].

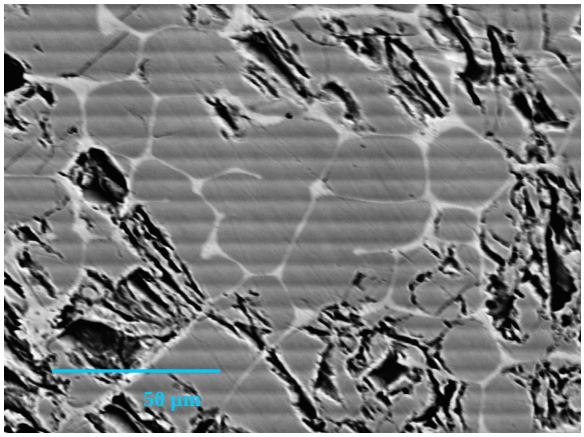


Figure 22.a: Electron microprobe picture of C/U = 0.8.

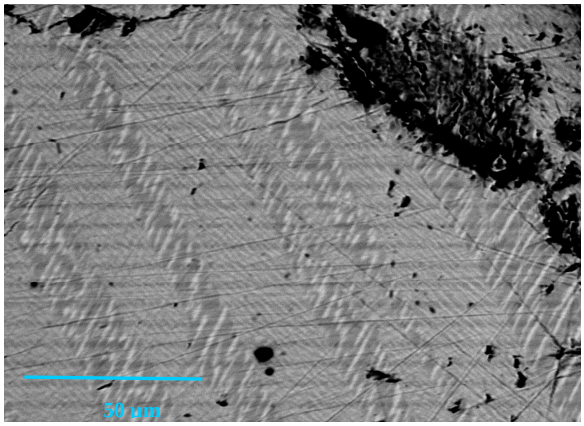


Figure 22.b: Electron microprobe picture of C/U = 1.7.

These different analyses seem therefore to confirm that the observed solid-solid phase transition should be attributed to the β-UC_2 to α-UC_2 transition. This cubic-to-tetragonal transition occurs without any atomic diffusion[41], however with an important lattice distortion, and can therefore be considered as martensitic, according to the definition given in references 44 and 45. The current investigation confirms the nature of this transition: despite its diffusionless nature, it actually occurs with an important release of latent heat (which can be attributed to strain energy) and at the same time with extremely rapid kinetics. This latter point is also typical of martensitic transitions, which are known to proceed very rapidly, at speeds approaching the velocity of sound in the material[46]. The velocity of sound c_s of β-UC_2 can only be estimated from mechanic properties available for cubic UC and tetragonal UC_2, namely from the bulk modulus B and the density ρ according to the formula[47]:

$$c_s = \sqrt{\frac{B}{\rho}} \qquad (5)$$

The densities and bulk moduli reported in the literature for UC and α-UC_2 are, respectively: ρ_{UC}(extrapolated at 2100 K)≈13g·cm^{-3}; B_{UC} = 158 GPa; $\rho_{\alpha/\beta\text{-}UC2}$(extrapolated at 2100 K)≈10.7 g·cm^{-3} and $B_{\alpha\text{-}UC2}$ = 216 GPa[48]. The speed of sound for these compounds can thus be calculated to be:

$$c_{sUC\ 2100} \approx 3.486 \cdot 10^3\ \mathrm{m \cdot s^{-1}} \qquad (6)$$

$c_{s\alpha\text{-}UC2\ 2100} \approx 4.49 \cdot 10^3\ m \cdot s^{-1}$ (7)

It is thus reasonable to assume that the velocity of sound in cubic β-UC_2 undergoing the β-α martensitic transition is of the order of $4 \cdot 10^3\ m \cdot s^{-1}$. Considering that the heated/cooled specimen can be approximated with a disc of 5 mm in diameter and several tens of microns in depth, according to the reported estimation the transition is expected to occur in only a few microseconds. For this reason even cooling rates of several hundreds thousands of $K \cdot s^{-1}$ are not sufficient to quench the β -UC_2 phase. Yet, a clear thermal arrest of several milliseconds is well observable in the current experiments, which seems to indicate that the phase transition proceeds in the material with an effective speed which is about 10^3 times lower than the speed of sound in the material. This observation can be useful for a deeper analysis of the β→α-UC_2 transition, to be developed with further research methods. For example, the presence of impurities (especially oxygen), large thermal gradients and a varying morphology in two-phased samples can slow the transition rate. However, it should be proven by further research whether these effects are sufficient to justify the observed duration of the β→α-UC_2 thermal arrest.

c) Accuracy analysis

Like in the case of oxides, the total uncertainty affecting the current experimental data points can be evaluated according to the law of independent error propagation:

$$E_{TOT} = \pm\sqrt{\sum_i E_i^2} \quad (8)$$

Three main uncertainty sources have been identified in the current phase transition point determination: the assumed spectral emissivity of the sample at the operating wavelength of the pyrometer, the temperature calibration and the random data point dispersion. Substituting the numerical values obtained for these uncertainties point by point and composition by composition yielded the error bars reported in table 3 and in figure 23 below. The composition uncertainty bands are based on the uncertainties reported for the ELTRA® measurements.

1.3 Summary of results on the uranium - carbon system

Approximately 200 laser heating experiments have been carried out for the determination of the uranium carbide behaviour at high temperature (1400 K ≤ T ≤ 3500 K), and finally 81 thermograms were selected based on the quality of the sample and thermograms.

C/U	Number of thermograms	Liquid – solid transition / K	Uncertainties / K	Solid-solid Transition / K	Uncertainties / K
0.80	2	2712	30		
1.02	10	2760	31		
1.27	9	2679	29		
1.39	8	2657	28		
1.48	14	2656	29		
1.54	7	2675	29	2072	19
1.65	5	2694	31	2069	18
1.70	11	2705	30	2053	19
1.88	7	2728	30	2039	18
2.02	3	2727	32		
2.06	6	2734	32	2071	19

Table 3: Value of the liquid-solid and solid-solid phase transitions based on a spectral emissivity of 0.53 at the operating wavelength of the pyrometer.

The experiments performed in the current project have permitted to assess the melting/freezing temperatures of uranium carbides with $0.8 \leq U/C \leq 2.1$, and also the temperatures of the $\beta \rightarrow \alpha$ solid-solid phase transition when applicable. Figure 23 shows a summary of these different results superimposed to the phase diagram U-C evaluated using the CALPHAD method based on available literature data under metastable conditions, i.e. ignoring the formation of U_2C_3 (as already proposed by Laugier and Blum[19]). This phase was actually never observed in the current samples, neither after arc melting and furnace annealing, nor after fast laser melting and quenching. It is therefore reasonable to assume that the current experimental observations correspond to the metastable phase diagram, as could be expected from the high cooling rates produced in the experiments.

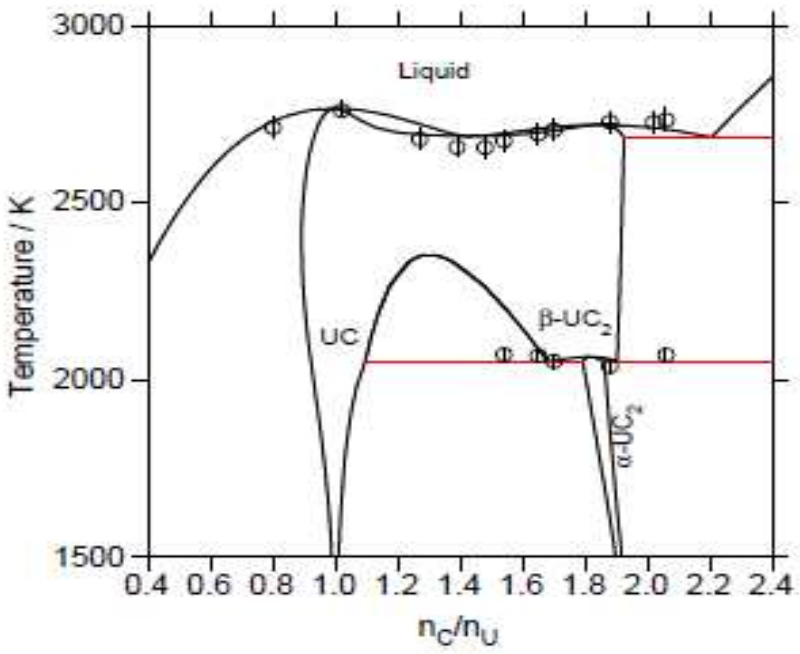


Figure 23: The metastable uranium - carbon phase diagram compared to the current data points.

All results are in fair agreement with the calculated phase diagram, considering the wide scatter of data presented in the literature. The solidus and liquidus temperatures could never be clearly distinguished, implying that the free energy curves of the two phases must be very close in the range investigated. This series of points is currently being used for an improved re-assessment of the high temperature uranium - carbon phase diagram.

2 The plutonium carbon phase diagram

Much less information is available for the plutonium - carbon system than for the uranium carbon system. For the sample synthesis, arc melting is a suitable technique. The elements react quickly together and form a dense carbide button which, compared to the powder obtained with metallurgic techniques, is relatively immune to atmospheric corrosion[6]. It has however been experienced that Pu_2C_3 samples as well as those with higher C/Pu ratio are fragile and easily break during cooling. Experimental data are principally available for low temperature and C/Pu<1. Thus, Storms[6] represented the high temperatures phase boundaries in dash lines only. The phase diagram calculated by Fischer[49] does not seem to fit

correctly the experimental data of Reavis[50, 51] for the liquidus temperatures. This author was the only one to perform, four decades ago, high temperature measurements on plutonium carbide samples with a differential thermal analysis apparatus[51]. In that research, the sample was contained in graphite crucibles covered by a graphite lid in which a 1mm diameter hole was drilled. It was then heated by induction and light emerging from the hole was focused on a photosensitive diode while light from a tungsten heat shield was focused on another photodiode. In parallel the sample temperature was measured with an optical pyrometer. Differential thermal analysis was thus obtained by comparison of the signals yielded by the two photodiodes. It should be noted that this method could be affected by large uncertainty in the measurement of absolute temperature whenever blackbody conditions were not met in the hole where the photodiode was focused, and particularly upon formation of liquid inside the hole.

The goal of the present work in this context was to check the applicability of fast laser heating to plutonium carbides and provide new data points for the assessment of the plutonium - carbon phase diagram. This is also an important starting point for the study of the ternary uranium - plutonium - carbon system.

2.1 Experimental methods

a) Sample preparation

Two samples, $PuC_{0.84}$ and Pu_2C_3, were prepared by arc melting using high vacuum (10^{-5}-10^{-6} mbar) and Ar-gas bottle 6N. The hypostoichiometric monocarbide was easily synthesised and re-melted a few times under the Ar arc to ensure good homogeneity, whereas the sesquicarbide was really fragile and during the third melting it broke into two parts. The resulting "buttons" were cut into disks in the same way as for the uranium carbide samples described above. Buttons were stored in vacuum before being cut and shortly after subject to the laser heating cycles. This procedure, aimed at minimizing the sample oxidation, was less effective for Pu-carbides than it was for U-carbides. The carbon content was measured with the fusion extraction – infrared determination (ELTRA ®) method described in chapter 2, but unfortunately it was not possible to measure the oxygen content with the current equipment. In the case of the PuC sample, the measured composition corresponded to the initial mass of carbon and plutonium weighed, yielding an atomic ratio C/Pu = 0.84. For Pu_2C_3, it was not

possible to measure immediately the sample and despite the dry atmosphere of the glovebox it oxidised rapidly, thus small pieces crumbled into powder. The carbon measurements were thus unsuccessful. All these experimental difficulties, in addition to the limited availability of metallic plutonium for the sample preparation, give an idea of how awkward it is to produce experimental data for the system Pu-C.

b) Sample analysis

Some pieces of the $PuC_{0.84}$ sample were ground and embedded for XRD analyses. The diffractogram obtained confirmed the monocarbide NaCl-like structure of this compound. However, non-negligible oxidation occurred within a few days. Figure 24 is a comparison of the results obtained on PuC eight and forty two days after preparation. Despite the storage under high vacuum the powder was oxidised. The peak intensity decreased and a second phase corresponding to PuO_2 appeared indicating the oxidation state of the sample. No X-ray diffraction data on Pu_2C_3 could be obtained in this study. This compound is very reactive to water vapour. Under a standard nitrogen atmosphere of 1000 ppm (O_2 + H_2O) it displayed excessive surface corrosion within a few minutes. Optimal condition to perform XRD analyses on such powder could therefore not be assured for this work.

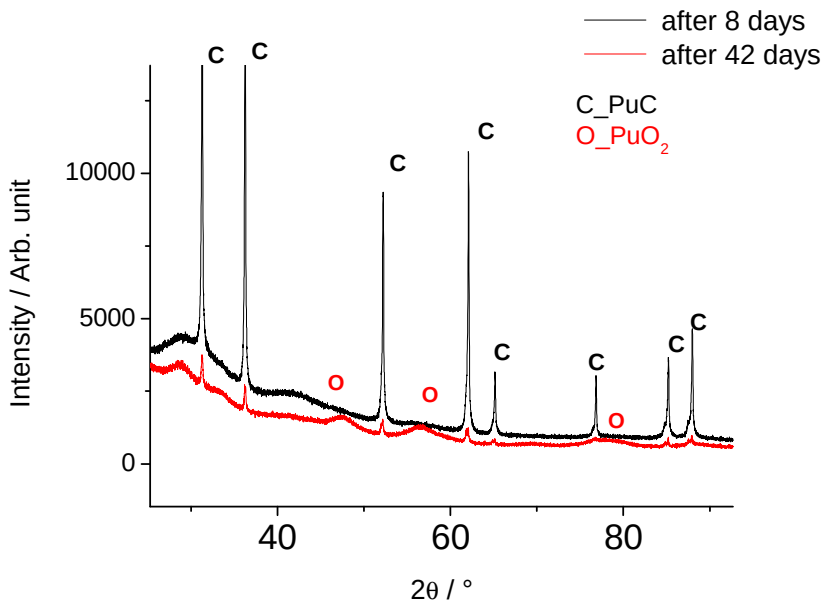


Figure 24: Comparison between the XRD pattern of the current PuC0.84 sample eight (black line) and forty-two (red line) days after preparation.

2.2 High temperature measurements via laser heating

a) PuC

Two disks, named A and B, were used to perform melting measurements of $PuC_{0.84}$. The laser heating cycles were performed under Ar at 1.5 bar with a laser spot of about 5 mm in diameter.

An emissivity analysis similar to the one performed in the case of stoichiometric UC was performed here for $PuC_{0.84}$. In this case, however the lower temperature and the poorer sample stability resulted in a larger uncertainty. A "slow" heating cycle was performed with a heating laser pulse lasting 1.25 s, in order to obtain exploitable signals with the VIS-NIR multichannel pyrometer previously described. To this purpose, an integrating time of 12 ms was used. The resulting thermogram, recorded by the photodiode at 649.4 nm with a tentative emissivity of 0.5, is reported in figure 25.

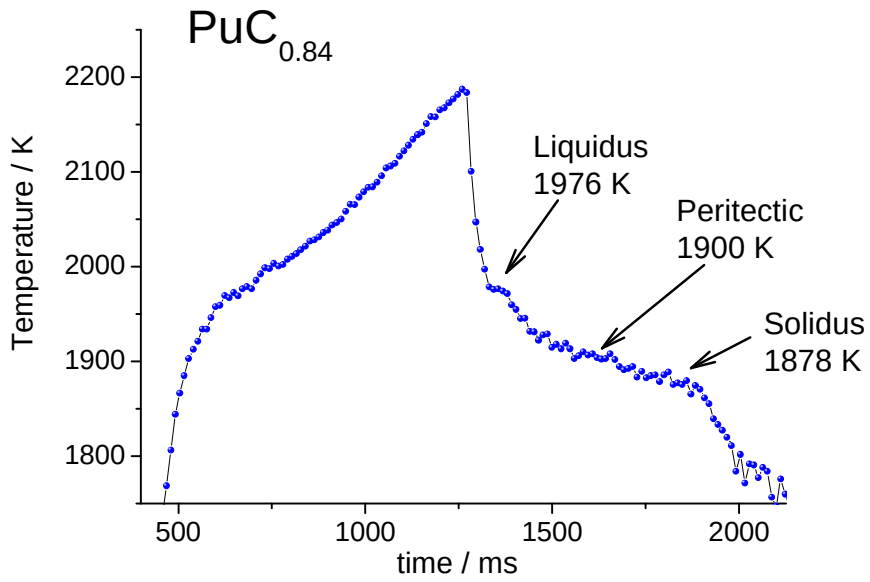


Figure 25: "Slow" thermogram recorded on a PuC0,84 sample by the 650 nm photodiode of the multi-channel VIS-NIR pyrometer with a tentative ε_{650}=0.5.

Probably, this experiment was affected by oxidation of the sample because of the

longer dwelling time at high temperature. In addition, the multi-channel pyrometer signal is characterized by a poor signal / noise ratio at low temperature, whereby increasing the integrating time yields a larger signal, but also amplifies the background noise. These factors should be taken into account as important error sources difficult to quantify. Nonetheless, clear thermal arrests are visible in the thermogram of figure 25. The first, on cooling, certainly corresponds to the liquidus point, and the last inflection to the solidus. This latter is expected to be slightly lower than the peritectic temperature, because the exact peritectic composition is slightly more enriched in C, as in the phase diagram reported in Figure 6 of Chapter 1. This transition does not correspond, for this composition, to a complete disappearance of the liquid phase. The associated latent heat released on cooling is therefore relatively small, and for this reason the peritectic is difficult to detect by the current thermal analysis. Nonetheless, an arrest can be observed in this slow experiment, as indicated in figure 25 between the liquidus and the solidus, and it must therefore correspond to the peritectic transition. Since the corresponding temperature has been determined by a few authors in the literature, this can be taken as a reference for an evaluation of the emissivity of PuC_{1-x}.

The peritectic line of PuC_{1-x} can be assumed to occur at (1900 ± 20) K, according to the review of Fisher[49] and the last data of Reavis[51]. By imposing this temperature to the experimental radiance spectra corresponding to the assumed peritectic thermal arrest in figure 25, the emissivity trend shown in figure 26 is obtained for $PuC_{0.84}$. Here, the dotted lines defining the uncertainty band correspond to the ±20 K uncertainty band on the assumed peritectic temperature. The resulting emissivity *vs* wavelength trend is:

$$\varepsilon_\lambda(PuC_{0.84}) = 0.85218 - 0.81369 \cdot \lambda + 0.4169 \cdot \lambda^2 \qquad (9)$$

It can be noted, that the actual spectral emissivity at 650 nm is very close to 0.5 (ε_{650}=0.505). This value can therefore be retained for further pyrometric measurements in the same wavelength range.

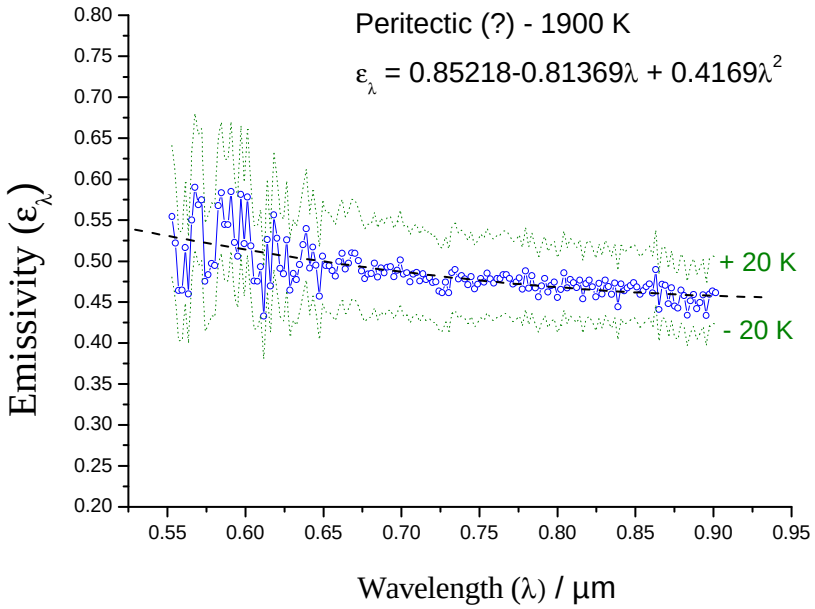


Figure 26: The measured wavelength dependence of the optical spectral emissivity of $PuC_{0.84}$ around the peritectic transition, assumed to occur at (1900 ± 20) K.

A first check of the obtained emissivity vs wavelength dependence was carried out by using expression (9) to fit the inverse radiance temperatures recorded at several wavelengths during the liquidus and solidus arrests in figure 25, compared with the peritectic inverse temperature curve. Results are plotted in figure 27. It seems confirmed that equation (9) can be reasonably used to estimate the emissivity of solid and liquid PuC in the vicinity of the co-existence temperature range. The emissivity obtained with this analysis was therefore used to obtain the real temperature curves in the faster heating cycles on $PuC_{0.84}$ described in the next paragraphs. Faster experiments were obviously aimed at minimising the sample degradation at high temperature, and particularly its oxidation.

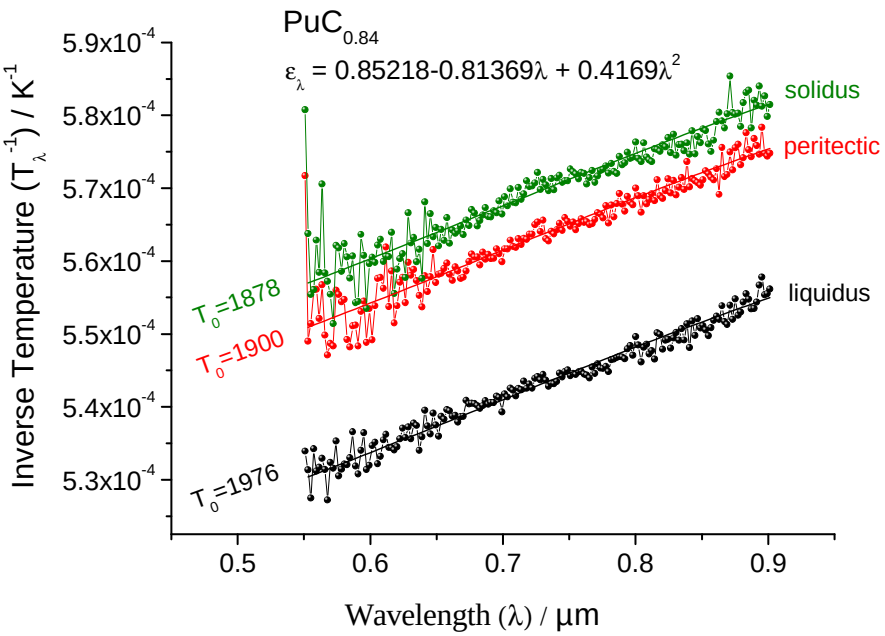


Figure 27: The inverse liquidus, peritectic and solidus radiance temperatures measured on a $PuC_{0.84}$ sample as a function of the pyrometer wavelength.

These fast experiments were performed on both disks A and B. In the first disk two inflexions were observed with the fast pyrometer at 652 nm: one around 1980 K and the second at around 1880 K (figure 28).

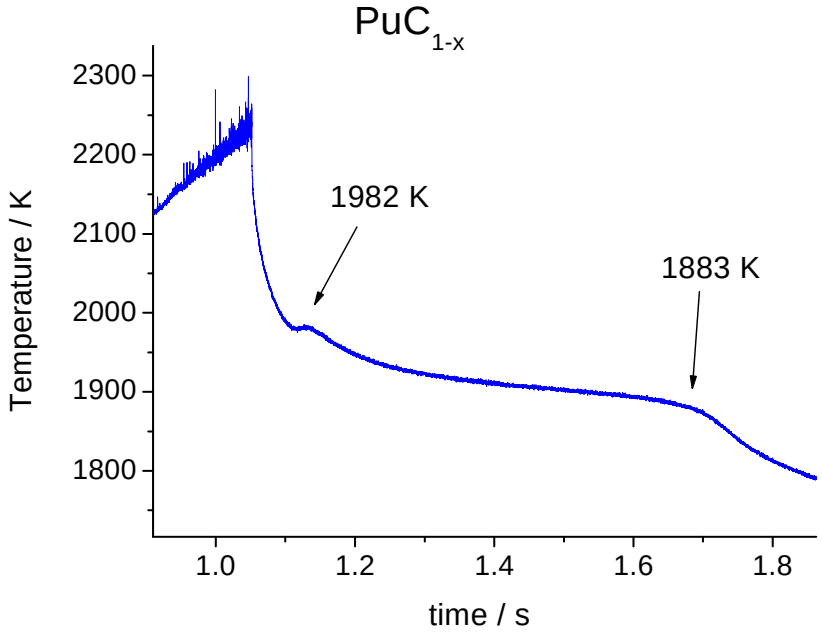


Figure 28 : Thermogram recorded on a $PuC_{0,84}$ sample, at λ = 650 nm and with ε_{650} = 0.5.

From the phase diagram, they correspond respectively to the liquidus and peritectic temperatures of PuC. To confirm the origin of the second one, a lower power laser pulse was applied to sample B (figure 29). The maximum temperature reached was slightly higher than the liquidus and no molten mater was observed on the sample. A thermal arrest was still observed at 1894 K. Thus the lower thermal arrest was perfectly reproducible from the first laser shot without forming any molten matter. This result disproves that segregation phenomena could be at the origin of the second thermal arrest and thus reinforce the assumptions made on the arrests observed in the "slow" thermogram of figure 25. Moreover, the transition temperatures proposed here correspond fairly well to those obtained by Reavis[51] via differential temperature analysis and support that PuC_{1-x} presents a good resistance to the laser irradiation.

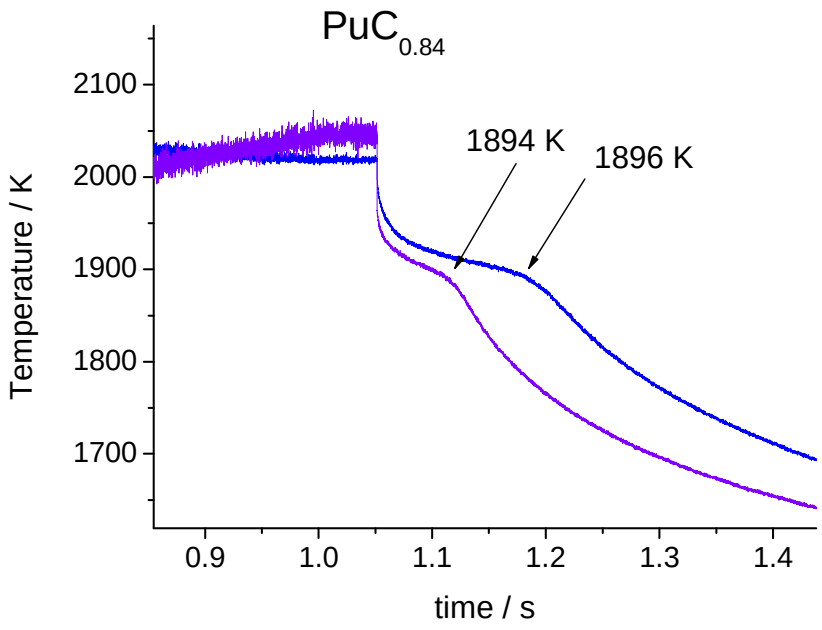


Figure 29: Thermogram recorded on a $PuC_{0,84}$ sample B, at λ= 650 nm and with ε_{650} = 0.5.

After a first series of experiments had been performed, the samples stayed inside the autoclave under Ar and the day after new laser heating cycles were performed. In total, 22 thermograms presented pronounced thermal arrests, figure 30 presents the temperatures obtained in all the heating cycles on both samples A and B. The results are very reproducible and they are not affected by the shape of the laser profile where the maximum temperature was varied in a range of several hundreds K. However, the liquidus temperatures obtained the second day were systematically higher. The oxidation of the

plutonium carbides may increase the melting temperature through the formation of PuO_2 phase ($T_m(PuO_2)$=3017 K, see Chapter 3).

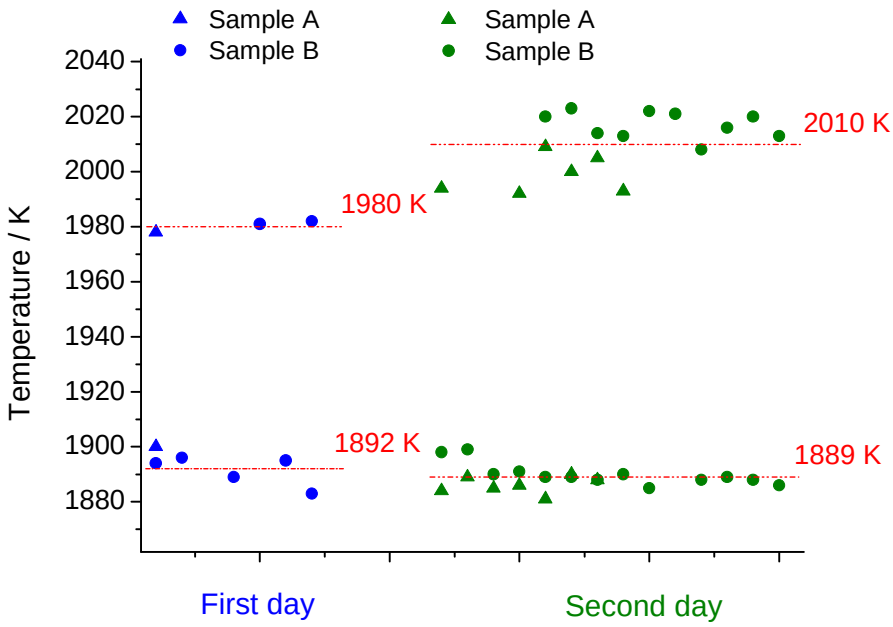


Figure 30: Liquidus and peritectic temperatures obtained in repeated shots on $PuC_{0.84}$ disks. Blue data points: first day. Red data points: second day.

XRD analyses were performed on the molten area obtained during the laser experiment and on the sample powder prepared from the sample synthesis. Both diffractograms resulted to be very similar, the peak intensities being smaller for the one performed after laser heating because of the very small quantity of matter. The lap of time before analyses (20 days) was long enough for the samples to be oxidised. Results in figure 31 show peaks corresponding to PuO_2 which could be easily formed because of the important active surface in both the case of the as-synthesised powder or the detached molten area. No second carbide phase was observed to be formed during the melting measurement, but because of the oxidation, it remained hardly possible to measure the cell parameter.

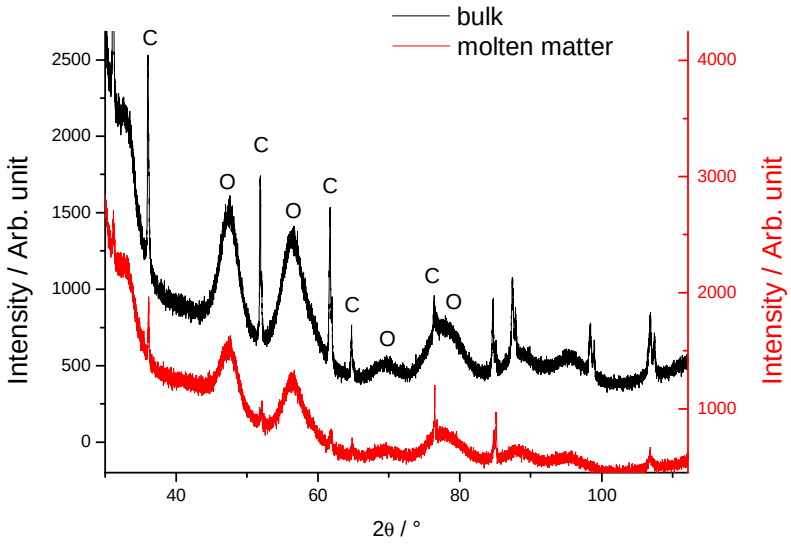


Figure 31: XRD performed on $PuC_{0.84}$

b) Pu_2C_3

Similar parameters were used for the melting measurement of Pu sesquicarbide. The Pu_2C_3 sample was much more fragile than $PuC_{0.84}$, and it quickly broke and fell apart under laser irradiation. After different trials, the remaining pieces were too small to be mounted between screws. A very small piece was therefore stuck in the ceramic glue already used for some UC samples (see Chapter 2). The atmosphere was then purged with an Ar-2% H_2 gas mixture and optics were mounted to have a 3 mm laser spot on the sample fragment only, in order to avoid fast heating and dissociation of the ceramic glue. Only one good thermogram could be obtained under these conditions (Figure 32). The vibrations observable at high temperatures, already recorded in other cases, could be due to vaporization or rapid movement of the liquid mass. The thermogram shows pronounced thermal arrests with temperatures comparable to those reported in the literature.

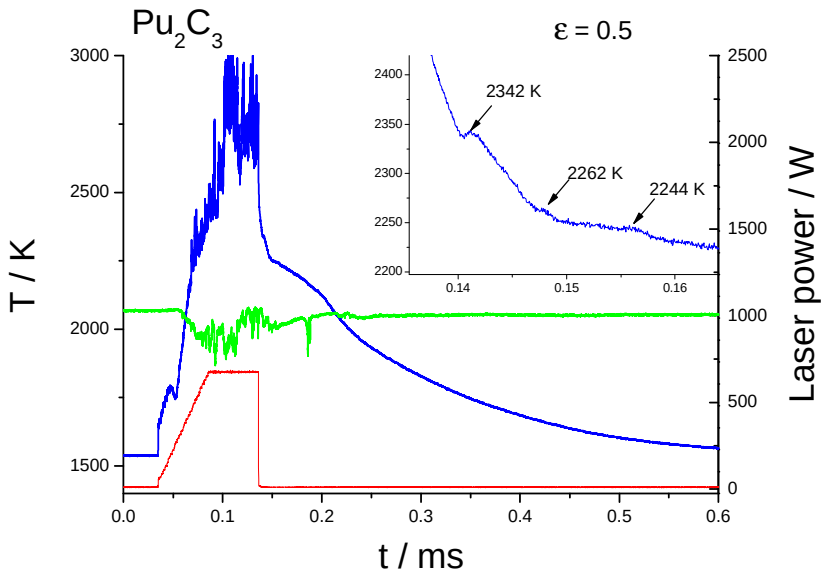


Figure 32: Thermogram recorded on a $PuC_{0,84}$ sample B, at λ=650nnm and with ε_{650}=0.5.

The same thermogram was recorded also with the multi-channel VIS- NIR pyrometer (Figure 33). This allowed a tentative study of the emissivity of solidifying Pu_2C_3, corresponding to the second arrest observed in the thermogram. To this purpose, since no reference temperature could be assumed for Pu_2C_3, the inverse Pu_2C_3 liquidus radiance temperature was fitted using equation (11) for the emissivity dependence on wavelength. This yielded a zero-wavelength (true) temperature $T_{0liquidus}(Pu_2C_3)$ = 2325 K (Figure 34). It can be seen in figure 34 that the fitting is not excellent, but also that the spectral signal / noise ratio is very poor in this case. This is a consequence, among other possible causes, of the high cooling rate produced in this experiment (for which the multi-channel pyrometer is not suited), the sample contamination with the ceramic glue etc. The high cooling rate and short experiment duration can also explain the differences between the fast pyrometer and the multichannel pyrometer thermograms in figure 33. Still it appears that the assessed emissivity trend can be employed in a first approximation even for Pu sesquicarbide.

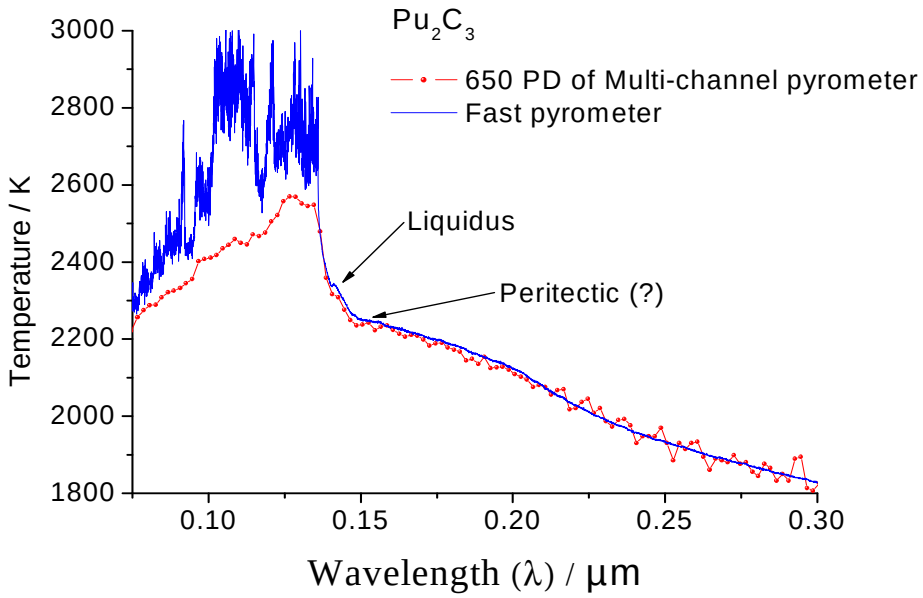


Figure 33: Thermogram recorded on a Pu_2C_3 sample at 650 nm by fast pyrometry (solid line) and by the 649 nm photodiode of the multi-channel pyrometer (line + red circles).

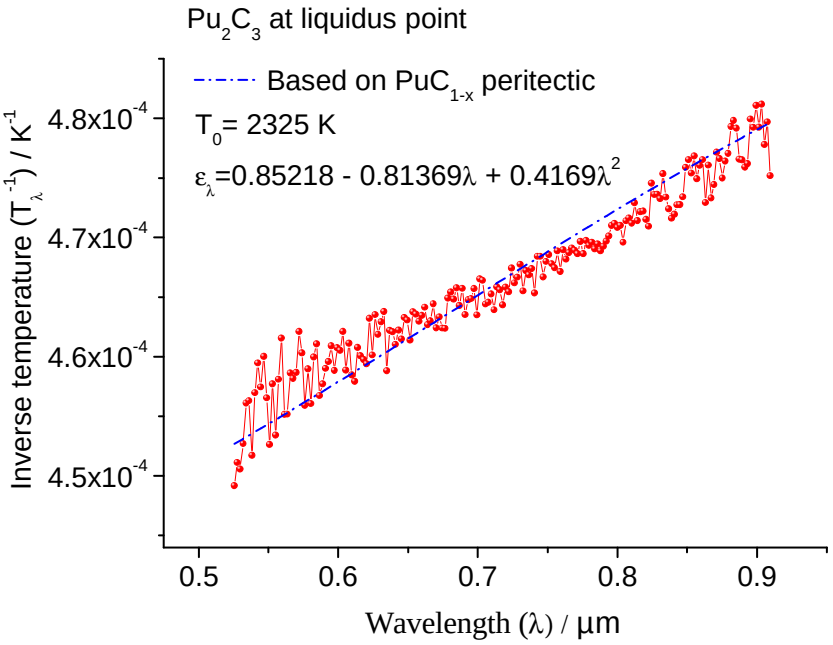


Figure 34: The inverse liquidus, radiance temperatures measured on the Pu_2C_3 sample as a function of the pyrometer wavelength. Extrapolation to zero-wavelength using equation (9) for the emissivity dependence on λ.

In conclusion, the liquidus point of Pu_2C_3 has been observed in this work at (2330 ± 40) K, whereas the peritectic arrest is still too uncertain to be assigned an established temperature.

Although this successful experiment showed the feasibility of a laser heating study of Pu_2C_3, it is obvious that large uncertainties still remain. For example, the sample had to be left in the glovebox during a full weekend, in order for the glue to completely dry. During this lapse of time, the specimen was probably partially oxidised which could influence the transitions temperatures, as already observed for $PuC_{0.84}$. Moreover, the glue slightly melted and interacted with the sample (as confirmed by SEM-EDS, which revealed contamination of the Pu_2C_3 with some wt % of Al) inducing an unquantifiable influence on the experimental results. They are nonetheless in a reasonable agreement with those assessed from the literature, as discussed in the following section.

2.3 Discussion

High temperature measurements on the plutonium carbides were realised by fast laser heating. They led to a few new experimental data in the plutonium-carbon phase diagram (figure 35). They confirmed the peritectic temperature of PuC already proposed by Reavis in a temperature range between 1890 and 1940 K. Variation of T_m due to oxidation is certainly a major factor of uncertainty. Reavis himself, on the other hand, reported performing heating cycles lasting about 1 minute and "sacrificed the accuracy of temperature measurements" to minimise interactions with crucible. The results obtained in this work on Pu sesquicarbide are more preliminary since only one thermogram was exploitable under the current experimental conditions, which should still be optimised. They were nonetheless close to existing literature data. Moreover, the tests performed here have been useful for the optimisation of the experimental parameters in view of further investigation.

In particular, the current laser heating technique can be applied to the analysis of the Pu-C binary system in order to minimise the sample degradation (reaction, oxidation) at high temperature. Investigating more compositions in the range $0.67 \leq C/Pu \leq 2+x$ will yield important information concerning in particular:

1. The liquidus temperatures;

2. The extension of the peritectic lines;
3. A more detailed study of the PuC_2 – C eutectic;
4. A study of the $\beta \rightarrow \alpha$ PuC_2 phase transition (so far detected only by Harper et al. by high temperature XRD).

Some of these features occur at a relatively low temperature (< 2500 K), which can in principle be measured also by other methods than optical pyrometry (e.g.:thermocouples). In these cases, a more detailed study of the sample emissivity will also be possible.

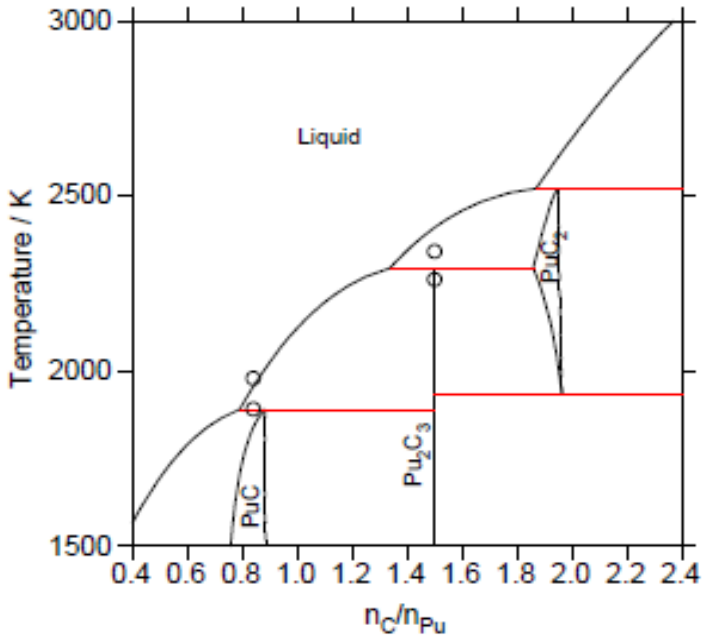


Figure 35: The plutonium - carbon phase diagram compared to the current data points.

3 References – Chapter 4

1. A technology roadmap for generation IV nuclear energy systems, DOE report GIF-002-00, December 2002.
2. R. P. Elliot, Constitution of Binary Alloys, McGraw-Hill, New York, 1965 (suppl. 1).
3. L. D. Brownlee, J. Br. Nucl. Energy Conf. 4 (1959) 35.
4. R. Benz, C. G. Hoffman, G. N. Rupert, High Temp. Sci. 1 (1969) 342.
5. F. A. Shunk, Constitution of Binary Alloys, McGraw-Hill, New York, 1969 (suppl. 2).
6. E. K. Storms, The refractory Carbides, vol. 2, Academic, New York, 1967.
7. W. Mallet, A. F. Gerds, H. R. Nelson, J. Electrochem. Soc. 98 (1952) 505.
8. P. Y. Chevallier, E. Fischer, J. Nucl. Mater. 288 (2001) 100.
9. P. Chiotti, J. Am. Ceram. Soc. 35 (1952) 123.
10. J. Henney, D. T. Livey, N. A. Hill, UKAEA Report 4176, 1963.
11. W. B. Wilson, J. Am. Ceram. Soc. 43 (1960) 77.
12. C. A. Utton, F. De Bruycker, K. Boboridis, R. Jardin, H. Noel, C. Guéneau, D. Manara, J. Nucl. Mater. 385 (2009) 2 443.
13. L. D. Brownlee, J. Inst. Metals 87 (1959) 58.
14. R. Hultgren, P. D. Desai, D. T. Hawtkins, M. Gleiser, K. K. Kelley, American Society of Metals, Metals Park OH, 1973
15. W. G. Witteman, M. G. Browman, quoted by E. K. Storms, US At. Energy Comm. LA-2942, 1964, 254pps; US At. Energy Commun. TID-7676 (Fourth Uranium Carbide Meeting, East Hartford, Conn.) 1963, 121.
16. H. W. Newkirk Jr., J. L. Bates, US At. Energy Comm. Report HW-59468, 1959, 5pp.
17. W. G. Witteman, J. M. Leitnaker, M. G. Bowman, US At. Energy Comm. Report TID 7603 (1961) 48.
18. G. D. White, P. D. Shalek, J. T. Dusek, US At. Energy Comm. Report ANL 6868 (1963) 152.
19. J. Laugier, P. L. Blum, J. Nucl. Mater. 39 (1971) 245.
20. J. M. Williams, R. A. J. Sambell, J. Less-Common Metals 1 (1959) 217.
21. E. Rudy, F. Benesovsky, Wissenschaften 94 (1963) 204.
22. L. E. Toth, H. N. Nowotny, F. Benesovsky, E. Rudy, Monatshefte fuer Chemie 92 (1961) 794.

23. A. E. Austin, Acta Crystal. 12 (1959) 159.
24. A. L. Bowman, G. P. Arnold, W. G. Witteman, T. C. Wallace, N. G. Nereson, Acta Cryst. 21 (1966) 670.
25. R. E. Rundle, N. C. Baenziger, A. S. Wilson, R. A. McDonald, J. Am. Chem. Soc. 70 (1948) 99.
26. R. C. Lied, G. D. White, J. Am. Ceram. Soc. 45 (1962) 149.
27. J. S. Olsen, L. Gerward, U. Benedict, J. P. Itie, K. Richter, J. Less-Common Metals 121 (1986) 445.
28. N. H. Krikorian, W. G. Witteman, M. G. Bowman, J. Electrochem. Soc. 110 (1963) 6.
29. H. Nickel, O. Inanc, K. Lucke, J. Nuc. Mater. 28 (1968) 79.
30. S. Ihara, K. Tanaka, M. Suzuki, Y. Akimoto, J. Nuc. Mater. 39 (1971) 203.
31. N. Vigier, C. Den Auwer, C. Fillaux, A. Maslennikov, H. Noel, J. Roques, D. K. Shuh, E. Simoni, T. Tyliszczak, P. Moisy, Chem. Mat. 20 (2008) 3199.
32. O. S. Ivanov, Z. M. Alekseeva, Struct. Alloys Certain Systems Cont. Uranium Thorium (1963).
33. M. Atoji, R. C. Medrud, J. Chem. Phys. 31 (1959) 332.
34. D. W. Jones, I. J. McColm, R. Steadman, J. Yerkess, J. Solid State Chem. 68 (1987) 219.
35. T. C. Wallace, N. H. Krikorian, P. L. Stone, J. Electrochem. Soc. 111 (1964) 12.
36. H. Nickel, H. Saeger, J. Nucl. Mater. 28 (1968) (1) 93.
37. E. Rudy, F. Benesovsky, Monatshefte fuer Chemie und verwandte Teile anderer Wissenschaften 93 (1962) (2) 522.
38. R. De Coninck, R. De Batist and A. Gijs, High Temp.-High Pressure 8 (1976) 167.
39. R. De Coninck, W. Van Lierde and A. Gijs, J. Nucl. Mater. 57 (1975) 69.
40. M. Bober, H. U. Karow and K. Mueller, High Temp.-High Pressure 12 (1980) 161.
41. Matzke, Hj. "Science of advanced LMFBR fuels", North Holland, 1986.
42. H. Shi, P. Zhang, S. Shen Li, B. Wangd, Bo Sun, J. Nucl. Mater. 396 (2010) 218.
43. R. Shein, A. L. Ivanovskii, J. Nucl. Mater. 393 (2009) 192.
44. K. H. G. Ashbee, F. C. Frank, C. K. H. DuBose, J. Nucl. Mater. 47 (1973) 323.
45. M. Cohen, G. B. Olson and P. C. Clapp, "*On the Classification of Displacive Transformations (What is Martensite?)*", Proc. Int. Conf. On Martensitic Transformations, ICOMAT 1979, Cambridge, Massachussets, USA, 24-29 June 1979, 1-11.
46. D. R. Askenland, "*The Science and Engineering of Materials*", Third Edition, Chapman and Hall, London1990, p.338.

47. F. Everest, (2001). *The Master Handbook of Acoustics*. New York: McGraw-Hill. pp. 262–263.
48. Gmelin handbook of inorganic chemistry, U, 8th edition, supplement volume C12: uranium carbides, 1987
49. E. Fischer, Computer Coupling of Phase Diagrams and Thermochemistry 32 (2008) 371.
50. J. G. Reavis, L. Reese, Quaterly Status Report on the Advanced Plutonium Fuels Program, April 1 to June 30, Los Alamos Scientific Laboratory of the University of California, LA-4484-MS, Project 463, (1969).
51. J. G. Reavis, L. Reese, Quaterly Status Report on the Advanced Plutonium Fuels Program, April 1 to June 30, Los Alamos Scientific Laboratory of the University of California, LA-4494-MS, Project 463, (1970).
52. E. A. Harper, H. J. Hedger and J. T. Dalton, Nature 219 (1968) 151

Chapter 5: Conclusions

The main focus of the present PhD project has been the measurement of high temperature phase transitions occurring in actinide compounds employable as nuclear fuels of the Fourth Generation. This study has mostly dealt with temperatures above 1800 K and often up to more than 3000 K. Much effort has been put in the identification and solution of the numerous difficulties connected with such extreme conditions. The main of such difficulties have been the fast kinetics of oxidation/reduction and volatilization phenomena, the interaction between sample and containment and the temperature measurements themselves. Concerning this last point, optical pyrometers are the only thermometers available at such high temperatures. These instruments allow accurate temperature measurements only if blackbody conditions can be produced or the spectral optical emissivity of the investigated samples is known at the operational wavelengths. However, in many cases neither of such conditions is met in the materials investigated in the present work, hence requiring an additional parallel investigation of optical properties. Because of all these factors, the identification and quantification of experimental uncertainty sources has constituted another challenging task of this work.

In this context, a recently developed approach, based on laser heating, has been applied to the study of various radioactive materials, producing a number of original experimental data points.

In conclusion, the present work has lead to significant progress both in the instrumental development and in the comprehension of the high temperature behaviour of actinide materials, as summarized in the following paragraphs.

1 Progress in the experimental method

The main advantage offered by the experimental method used in this work is the possibility to perform extremely fast high-temperature measurements under containerless conditions and controlled atmosphere. The heating cycles presented in this work last from tens to hundreds milliseconds, compared to the minutes or hours of traditional methods.

Because of the extreme sample reactivity at very high temperature, the short duration of tests constituted a valid way of limiting undesired degradation of the investigated materials. For the same reason, another advantage of the current method is to heat only a restricted area of the sample surface, ensuring that no effective contact between the investigated area and the sample containment occurred. This method has been shown, for the first time, to be particularly suited for pyrophoric carbides that are easily oxidised. Measurements were also successfully performed on actinide dioxides, which have a significant vapour pressure at the temperature of melting.

Particular effort has been put in the improvement of calibration and tests of pyrometers. For example, the very high temperature linearity and accuracy of the pyrometers was checked by measuring the melting point of standard materials such as Mo, the ZrC-C eutectic and W. In these tests, other possible undesired side effects have been taken into account. In particular, the impact on the experimental results of occasional temperature gradients across the investigated spot has been evaluated. Theoretical and experimental investigations have been therefore undertaken at ITU in collaboration with Polytech'Orléans to quantify this effect. The main error source in the current measurements remains the uncertainties in the determination of the sample spectral emissivity. This optical property had to be determined in the investigated materials, because blackbody conditions could not be produced while maintaining the containerless character of the current experimental method. For this purpose, emissivity was studied by multi-wavelength pyrometry, whereby the spectral domain ranged from the ultraviolet (215 nm) to the near infrared (915 nm). Although this approach required the choice of secondary emissivity or temperature references, implying an additional uncertainty source, it allowed the measurement of consistent and original data in this difficult research domain.

Another difficulty of the current approach has been the particularly small quantity of molten matter, about tens of milligrams, quite challenging to characterize after melting. Nonetheless, satisfactory results have been obtained by XRD and SEM – EDS, supporting the consistency of the current high temperature phase transition measurements. Besides these traditional methods, more sensitive apparatus are currently being developed for active materials characterisation. Thus, for example, transmittance electron microscope and Raman spectrometry could be added in future work in the same research field.

2 Material properties

Experimental data have been produced in this work for the high temperature behaviour of two different types of compounds: oxides and carbides.

Oxides are electrical and thermal insulators, implying limited conductive thermal losses and high emissivity, which are two advantages for the current high temperature studies. On the other hand, these materials are characterized by high oxygen potential and volatility at the measurement temperatures. The current laser method under containerless conditions permitted to limit the vaporisation issue and prevent oxidation / reduction reactions between sample and crucible.

A series of experiments was first performed on pure actinide oxides. Well reproducible thermograms were recorded and high temperature data thus obtained were validated by post melting characterisations. The well established melting point of $UO_{2.00}$, (3130 ± 20) K, was reproduced. On the other hand, the congruent fusion/solidification temperature measured in this research on stoichiometric PuO_2 is significantly higher compared to literature data. This melting point was established at (3017 ± 28) K, 170 K above the value reported in the most recently published assessment. This difference must be attributed to extensive reaction between sample and containment when using more traditional furnace heating techniques. Moreover, the melting behaviour of plutonium dioxide as a function of the O/Pu ratio, which is still controversial, was also addressed. Preliminary experiments were performed in this work under reducing conditions and it was observed that the melting temperature of PuO_{2-x} decreases with oxygen. However doubts still remain on this last point due to the difficulties in controlling the O/Pu ratio in experiments on non-stoichiometric and non-congruently melting samples. Finally, preliminary experiments were performed on the melting point of NpO_2. Despite the still large uncertainties, due in this case to the limited availability of specimens, also the NpO_2 melting temperature was determined to be (3040 ± 40) K, much higher than previous authors.

The new melting point determined for PuO_2 imposed a reinvestigation of the complete UO_2-PuO_2 phase diagram at high temperature. More than vaporisation control and emissivity determination, the main difficulty of this study on U, Pu mixed oxides (MOX) was the control

of oxygen, uranium and plutonium distribution in the presence of temperature gradients. This issue essentially originates from the fact that PuO_2 has a much higher oxygen potential than UO_2. Segregation and formation of secondary phases were limited as much as possible by annealing samples under a suited gas flux prior to the laser heating cycles, and by optimizing the experimental parameters during the melting point measurements. Despite the large uncertainties, it is possible to determine the general tendency of the melting point across the MOX compositions. The fusion/solidification points measured in this work are in fair agreement with older data for samples with low PuO_2 content (< 50 %). It was observed, however, that for higher plutonium contents the solidus and liquidus lines are likely to slightly differ from those of an ideal solution, as previously proposed in the literature. Instead, a minimum melting temperature probably exists around the MOX with 50 % PuO_2. This points needs to be confirmed by further measurements. In addition an experimental apparatus aimed at the determination of high temperature phase transitions of radioactive materials held under an elevated buffer gas pressure is currently being developed at ITU. This facility will possibly allow studying the melting behaviour of U, Pu MOX with a better control on the oxygen behaviour.

The uranium-carbon and the plutonium-carbon systems were also investigated. The metallic character of these compounds implies large conductive thermal losses and low emissivity, often dependent on the wavelength. These features, in addition to their high reactivity towards oxygen, constituted the main difficulties in the study of these materials, which were less affected by vaporisation and reaction with the containment. Emissivity values were measured in this work on UC and UC_2, obtaining data close to the very few existing in the literature. Moreover, the obtained emissivity values have been originally assessed as a function of wavelength and oxygen impurities. They were moreover shown to be usable also for other non-stoichiometric samples with C/U ratio between 0.8 and 2.1. The melting temperatures and some solid-solid phase transitions of these uranium carbides were thus determined with an uncertainty of approximately 20 K. The current values are in fair agreement with recently optimized phase diagrams, showing that the current experimental approach reproduces data obtained with more traditional methods in samples not too volatile or reactive towards the containment.

Very few experimental information exist for the Pu-C system at high temperature. The high oxidation rate of these materials makes their characterisation very difficult. However, the

first attempts performed in this work brought reasonable values and demonstrated the suitability of the current method for melting measurements of plutonium carbides.

3 Impact of the current result

The results obtained in this work on the melting point of different actinide oxides and carbides are summarized in figure 1, where they are also compared with previously existing data. Results on carbides corroborate, within the experimental uncertainty, the literature values, and reinforce them because they have been obtained with a totally different experimental approach. In some cases, moreover, the current data have a better precision than the previous ones. On the other hand, the important differences between current and older melting point data on plutonium and neptunium dioxides cast doubts on the validity of high temperature studies on actinide oxides, and, in general, highly reactive materials by “traditional” furnace heating methods. In this respect, the current research can be seen as the stimulance for a reinvestigation of the melting behaviour of many refractory materials. In particular, the melting point trend for the actinide dioxide need revisiting in future research, yielding important information also at a more fundamental level of actinide science. For example, the new results show a much less steep variation with atomic number in the dioxides of the transuranic elements. The existing data suggest an almost linear decrease with atomic number, whereas the new data suggest a "saturation", to be confirmed by further research on the trans-plutonium element compounds.

From a more technological viewpoint, the new results on the U-Pu-O systems at high temperature could have a concrete impact on the nuclear fuel design. All the experimental information produced in this work will be integrated in nuclear fuel data bases and used for the thermodynamic optimization of phase diagrams.

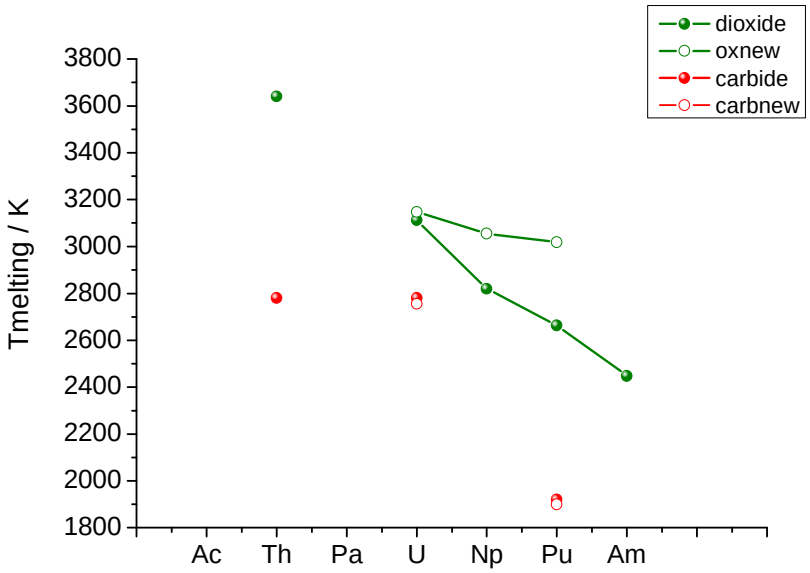


Figure 1: Melting point of actinide oxides and mono carbides.

Franck DE BRUYCKER

Transitions de phases à hautes températures de combustibles nucléaires de quatrième génération

Il est important de bien connaitre le comportement des combustibles nucléaires dans des conditions extrêmes afin d'assurer la sureté des réacteurs et de prévoir les conséquences d'un éventuel accident. L'objectif principal de cette thèse est l'étude des transitions de phase à très haute température de matériaux envisagés pour les combustibles nucléaires de quatrième génération. Dans ce but, une méthode a été développée à l'institut européen des transuraniens (ITU) pour étudier ces matériaux à des températures excédant 2500K. La technique utilisée consiste à chauffer l'échantillon à l'aide d'un laser de haute puissance et à mesurer sa température par pyrométrie. Le signal d'un second laser réfléchi par la surface de l'échantillon est aussi étudié afin de mieux caractériser les transitions de phase. Les avantages de cette technique résident dans la rapidité des expériences (de quelques dizaines de ms à quelques secondes), et dans le contrôle de l'atmosphère, ce qui permet de limiter les effets d'évaporation ou d'oxydation/réduction de l'échantillon. Il convient de signaler que seule la partie centrale de l'échantillon est fondue, la phase liquide sondée est ainsi confinée au sein de l'échantillon lui-même, ce qui évite toute interaction avec le système de fixation. Nos résultats sur les carbures d'uranium sont en accord avec ceux de la littérature, et ont permis d'affiner le calcul des diagrammes de phase pour ces matériaux stables à haute température. La technique que nous avons mise au point a été utilisée, pour la première fois, pour étudier des matériaux de haute activité. Des résultats originaux ont été obtenus sur les systèmes PuO_2, NpO_2, UO_2-PuO_2 et Pu-C.

Mots clés : haute température, transition de phase, chauffage laser, pyrométrie, plutonium, uranium

High Temperature Phase Transitions in Nuclear Fuels of the Fourth Generation

Understanding the behaviour of nuclear materials in extreme conditions is of prime importance for the analysis of the operation limits of nuclear fuels, and prediction of possible nuclear reactor accidents, relevant to the general objectives of nuclear safety research. The main purpose of this thesis is the study of high temperature phase transitions in nuclear materials, with special attention to the candidate fuel materials for the reactors of the 4th Generation. In this framework, material properties need to be investigated at temperatures higher than 2500K, where equilibrium conditions are difficult to obtain. Laser heating combined with fast pyrometer is the method used at the European Institute for Transuranium Elements (JRC – ITU). It is associated to a novel process used to determine phase transitions, based on the detection, via a suited low-power (mW) probe laser, of changes in surface reflectivity that may accompany solid/liquid phase transitions. Fast thermal cycles, from a few ms up to the second, under almost container-free conditions and control atmosphere narrow the problem of vaporisation and sample interactions usually meet with traditional method. This new experimental approach has led to very interesting results. It confirmed earlier research for material systems known to be stable at high temperature (such as U-C) and allowed a refinement of the corresponding phase diagrams. But it was also feasible to apply this method to materials highly reactive, thus original results are presented on PuO2, NpO2, UO2-PuO2 and Pu-C systems.

Keywords : High temperature, phase transition, laser heating, pyrometry, plutonium, uranium

JRC EUROPEAN COMMISSION

Institut Transuranium Karlsruhe
Von-Helmotz-Platz 1
76344 Eggenstein-Leopoldshafen
Germany

I.T.U